

# Reviews of Geophysics®



## REVIEW ARTICLE

10.1029/2023RG000808

## Dynamics, Monitoring, and Forecasting of Tephra in the Atmosphere

### Key Points:

- Explosive eruptions can generate plumes that reach heights up to tens of kilometers, dispersing solid clasts (tephra) over long distances
- The most significant improvements in tephra monitoring from satellites in the past decade have come from advanced geostationary imagers
- Probabilistic and ensemble numerical modeling are emerging as the standard strategies for the operational forecasting of tephra clouds

### Correspondence to:

F. Pardini,  
federica.pardini@ingv.it

### Citation:

Pardini, F., Barsotti, S., Bonadonna, C., de' Michieli Vitturi, M., Folch, A., Mastin, L., et al. (2024). Dynamics, monitoring, and forecasting of tephra in the atmosphere. *Reviews of Geophysics*, 62, e2023RG000808. <https://doi.org/10.1029/2023RG000808>

Received 2 FEB 2024

Accepted 2 OCT 2024

F. Pardini<sup>1</sup> , S. Barsotti<sup>2</sup>, C. Bonadonna<sup>3</sup> , M. de' Michieli Vitturi<sup>1</sup> , A. Folch<sup>4</sup>, L. Mastin<sup>5</sup> , S. Osoreo<sup>6</sup> , and A. T. Prata<sup>7</sup>

<sup>1</sup>Istituto Nazionale di Geofisica e Vulcanologia (INGV), Sezione di Pisa, Pisa, Italy, <sup>2</sup>Icelandic Meteorological Office, Reykjavík, Iceland, <sup>3</sup>Department of Earth Sciences, University of Geneva, Geneva, Switzerland, <sup>4</sup>Geociencias Barcelona (GEO3BCN-CSIC), Barcelona, Spain, <sup>5</sup>U.S. Geological Survey, Cascades Volcano Observatory, Vancouver, WA, USA, <sup>6</sup>Servicio Meteorológico Nacional, Buenos Aires, Argentina, <sup>7</sup>CSIRO Environment, Clayton, VIC, Australia

**Abstract** Explosive volcanic eruptions inject hot mixtures of solid particles (tephra) and gasses into the atmosphere. Entraining ambient air, these mixtures can form plumes rising tens of kilometers until they spread laterally, forming umbrella clouds. While the largest clasts tend to settle in proximity to the volcano, the smallest fragments, commonly referred to as ash ( $\leq 2$  mm in diameter), can be transported over long distances, forming volcanic clouds. Tephra plumes and clouds pose significant hazards to human society, affecting infrastructure, and human health through deposition on the ground or airborne suspension at low altitudes. Additionally, volcanic clouds are a threat to aviation, during both high-risk actions such as take-off and landing and at standard cruising altitudes. The ability to monitor and forecast tephra plumes and clouds is fundamental to mitigate the hazard associated with explosive eruptions. To that end, various monitoring techniques, ranging from ground-based instruments to sensors on-board satellites, and forecasting strategies, based on running numerical models to track the position of volcanic clouds, are efficiently employed. However, some limitations still exist, mainly due to the high unpredictability and variability of explosive eruptions, as well as the multiphase and complex nature of volcanic plumes. In the next decades, advances in monitoring and computational capabilities are expected to address these limitations and significantly improve the mitigation of the risk associated with tephra plumes and clouds.

**Plain Language Summary** During explosive volcanic eruptions, fragmented material known as tephra is forcefully injected into the atmosphere through volcanic plumes. While the largest clasts tend to settle in proximity to the volcano, the smallest fragments, commonly referred to as ash, can be transported over long distances, forming volcanic clouds. On the ground, tephra poses a significant hazard to human activities, both near the volcano and at distances up to hundreds of kilometers. In contrast, volcanic clouds present a serious threat to aviation. For these reasons, we are motivated to understand the dynamics of tephra plumes and clouds and how we can mitigate their hazards. Today, we have the capability to monitor tephra plumes and clouds using a plethora of techniques, ranging from ground-based methods to satellite instruments. Moreover, forecasting of tephra dispersion through computer simulations has become a valuable tool used to mitigate the risk of explosive eruptions. In this paper, we provide a comprehensive review of the current understanding of tephra plumes and clouds, covering their generation, the factors that influence their characteristics, and the latest strategies for monitoring and forecasting.

## 1. Introduction

During explosive volcanic eruptions, hot mixtures of solid fragments (tephra) and gasses are injected into the atmosphere and carried upward by buoyant columns (volcanic plumes) that eventually spread laterally, forming umbrella clouds. The largest tephra clasts (blocks, bombs, and lapilli;  $> 2$  mm) settle close to the volcano, either from the plume margins or following ballistic trajectories from the vent, while the smallest particles (ash;  $\leq 2$  mm) typically reach higher atmospheric altitudes and are dispersed over wider areas. Volcanic plumes are actively supplied by material from an erupting volcanic vent. When the eruption ceases, the plume can disperse and evolve into a volcanic cloud, which consists of the remaining airborne tephra and gasses (Figure 1). Volcanic clouds can spread thousands of kilometers downwind and eventually circle the Earth in a matter of days (Khaykin et al., 2022; Robock & Matson, 1983; Rose & Durant, 2011) (Figure 2).

© 2024 The Author(s). This article has been contributed to by U.S. Government employees and their work is in the public domain in the USA.

This is an open access article under the terms of the [Creative Commons Attribution License](https://creativecommons.org/licenses/by/4.0/), which permits use, distribution and reproduction in any medium, provided the original work is properly cited.

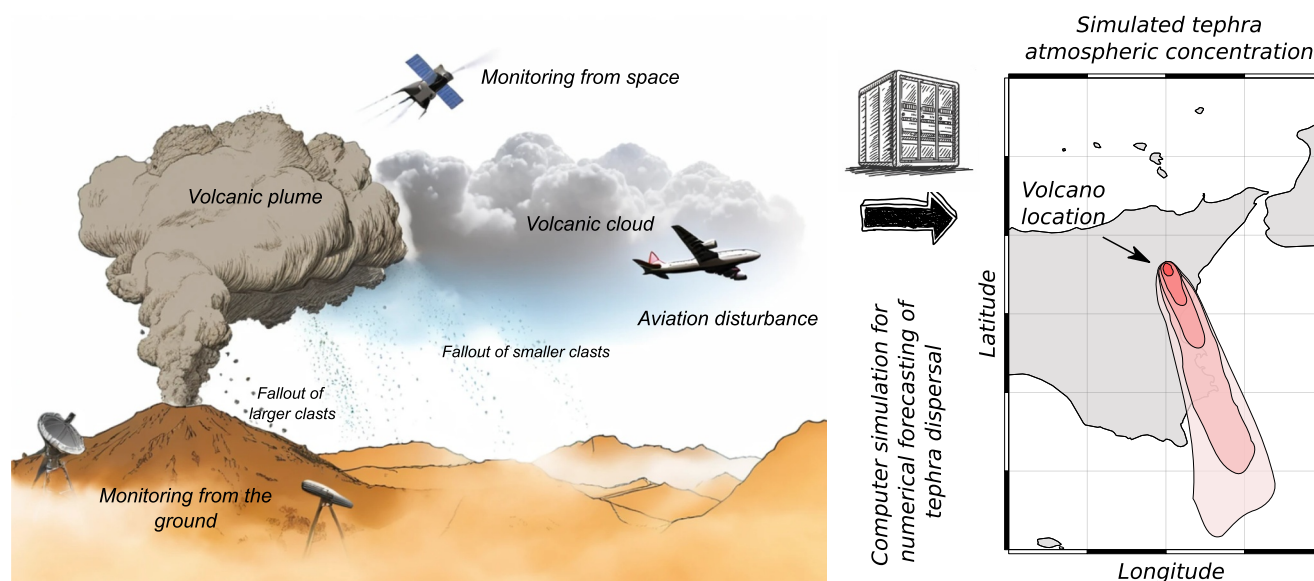


**Figure 1.** Cartoon summarizing the main topics addressed in the paper: physics of volcanic plumes and clouds, monitoring from the ground and space, and numerical forecasting of tephra clouds, with an emphasis on hazard assessment related to tephra suspended in the atmosphere.

Volcanic plumes can be generated by explosive events of any magnitude, from small short-lasting events to large caldera-forming eruptions. The smallest episodes, with a Volcanic Explosivity Index (VEI) of 0, erupt no more than  $10^4 \text{ m}^3$  of tephra, with eruption column heights below 100 m. In contrast, the largest eruptions, rated VEI 8, can eject more than  $10^{12} \text{ m}^3$  of tephra, reaching column heights well above 25 km (Newhall & Self, 1982; Sigurdsson et al., 2015). For example, Stromboli volcano (Italy) produces daily mild explosions (VEI 0) that primarily affect the nearby volcanic terrace (Rosi et al., 2013). In contrast, the Toba caldera-forming eruption (Indonesia, 75,000 years ago; VEI 8) spread tephra over a significant portion of the northern Indian Ocean and has been hypothesized to have accelerated the transition to an ice age climate mostly due to the interactions of sulfate aerosols with radiation from the Sun and Earth (Black et al., 2021; Rampino & Self, 1992). Between these extremes, 50–70 eruptions with volumes  $\geq 0.1 \text{ km}^3$  occur annually (submarine and subaerial) showing a variety of eruption styles and dynamics (Siebert et al., 2015). The complexity of volcanic processes means that a single volcano can experience different types of eruption styles. Recording volcanic activity worldwide helps to better investigate eruption processes and mitigate hazards. In this sense, the *Global Volcanism Program*, led by the Smithsonian Institution, maintains an extensive database of Holocene/Pleistocene volcanoes and eruptions from the past 12,000 years (<https://volcano.si.edu>). The catalog contains detailed records of past eruptions and includes weekly updates on volcanic activity around the world. These reports provide information on ongoing eruptions, seismic activity, and other relevant observations. This database represents an essential resource for researchers and hazard assessment professionals.

In the case of explosive eruptions, volcanic products pose several hazards, not only from tephra but also from other types of emissions, such as gasses (e.g., Carlsen et al., 2021). Public health, buildings, and infrastructure can be significantly impacted by the presence of tephra suspended into the air (in this case mainly ash) or accumulated on the ground (Bonadonna et al., 2021; Deligne et al., 2022; T. M. Wilson et al., 2015). Studies to determine the effects of exposure to volcanic particles on human health have been conducted over the years (see Stewart et al. (2022) and references therein), with acute and chronic respiratory diseases reported in populations exposed to volcanic ash (Baxter et al., 1983; Forbes et al., 2003; G. Gudmundsson, 2011; Hillman et al., 2012). Particle size, shape and mineral composition determine the potential hazard of volcanic particles if inhaled. Particles less than  $4 \mu\text{m}$  diameter are called *respirable* and can penetrate the alveolar region of the lungs, producing toxic reactions (Horwell et al., 2003). On the ground, tephra fallout can severely impact critical infrastructure, causing economic losses in various sectors (Ayris & Delmelle, 2012; M. Bebbington et al., 2008; Giles et al., 1999; Wardman et al., 2012; T. M. Wilson et al., 2012). Critical infrastructure includes energy and water/wastewater supply networks, transportation (aviation, land, and marine), food and agriculture, manufacturing, and communications. Quantifying the thickness (or static load) of tephra necessary to cause structural damage or complete disruption of a service is quite

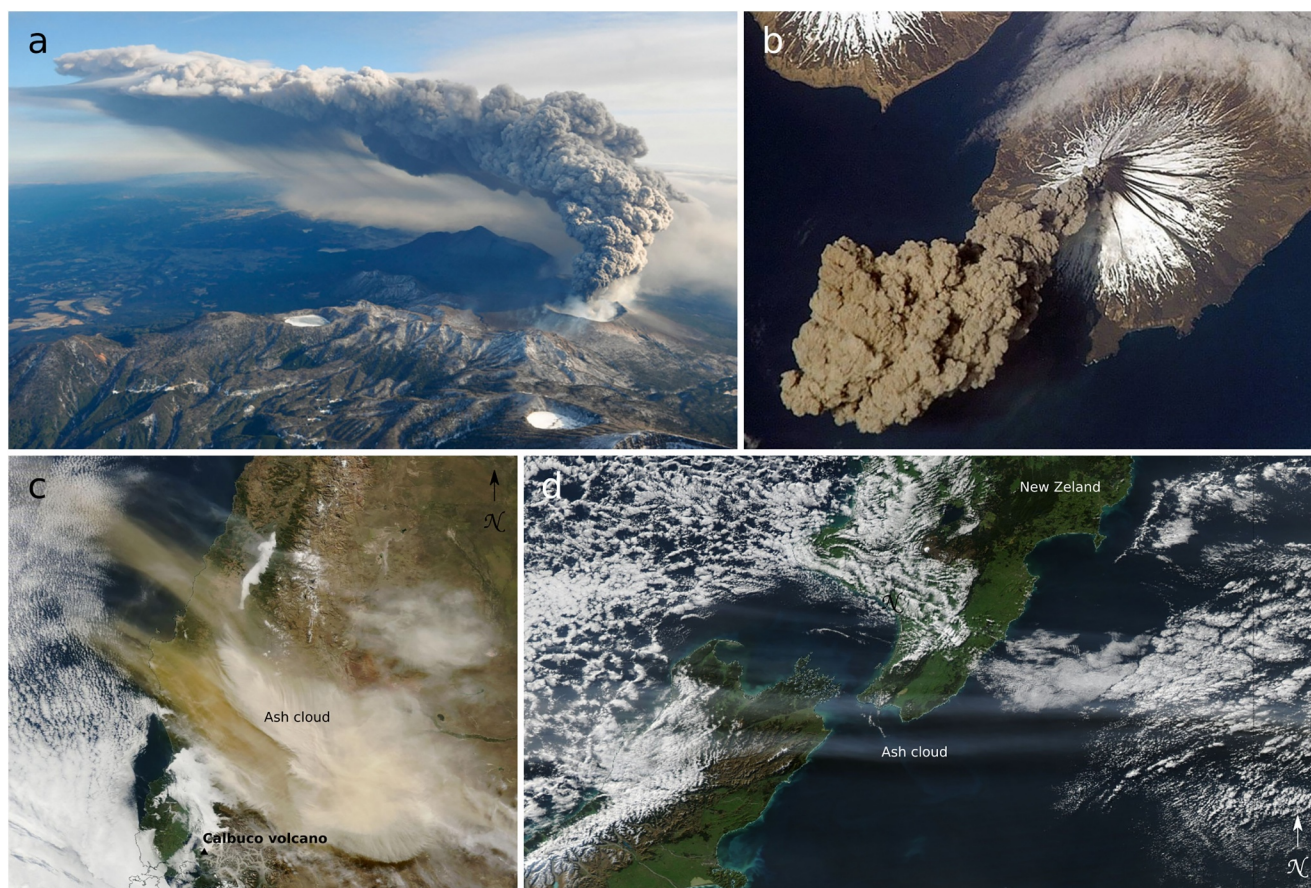


**Figure 2.** (a) Volcanic plume from the 2011 eruption of Shinmoedake volcano (Japan). Photo credit: US Geological Survey. (b) Volcanic plume generated by the eruption of Mount Cleveland volcano (United States) on 23 May 2006. The photograph was taken from the International Space Station at an orbital altitude of approximately 400 km. The image is freely available in the Gallery of the Global Volcanism Program, led by the Smithsonian Institution. (c) True-color image taken by the MODIS sensor onboard the Terra NASA satellite, showing the volcanic cloud produced by the eruption of Calbuco volcano (Chile) in April 2015. Image source: NASA. (d) The ash cloud from the 2011 Puyehue-Cordón Caulle eruption (Chile) traveled more than halfway around the world, reaching New Zealand. The true-color image was taken by the MODIS sensor onboard the Aqua NASA satellite. Image source: NASA.

challenging, as it strongly depends on characteristics of the infrastructure involved. A few to tens of millimeters of tephra are normally sufficient to damage residential buildings and infrastructure (G. Wilson et al., 2014; T. M. Wilson et al., 2012). A static load of  $100 \text{ kg/m}^2$  (corresponding to a thickness of 10 cm assuming a density of  $1,000 \text{ kg/m}^3$ ) is commonly taken as the limit above which roofs collapse and structural damages to networks and disruption of services may occur (S. F. Jenkins et al., 2015). Depending on the roof pitch, tephra can slide off, reducing the load on the roof compared to the load deposited on the ground (Osman et al., 2023). In any case, corrective actions ranging from cleaning to expensive repairs or replacements are required to restore the initial condition (Hayes, Wilson, et al., 2019; G. Wilson et al., 2014). While tephra fallout can have positive effects on soil and ocean fertility in the long term (Barone et al., 2022; Fiantis et al., 2019), agricultural activities and crops can be seriously damaged if blanketed by tephra (Craig et al., 2016; Cronin et al., 1998). Rural communities, whose economic activities are primarily based on agriculture and livestock, can be affected by tephra fallout not only immediately after an eruption, but also months to years afterward due to wind remobilization of volcanic deposits in ash storms. These storms produce effects similar to the initial eruption but perpetuate for years, significantly slowing down the economic recovery of the affected populations (Dominguez, Bonadonna, et al., 2020; T. M. Wilson et al., 2011). The international *Volcanic Ashfall Impacts Working Group*, sponsored by the US Geological Survey (USGS), provides resources and guidance for the public, agencies, and scientists on mitigation actions to be taken in case of tephra fallout ([https://volcanoes.usgs.gov/volcanic\\_ash/](https://volcanoes.usgs.gov/volcanic_ash/)).

Prior to deposition, volcanic ash dispersed and suspended in the atmosphere poses a significant risk to aviation safety (Alexander, 2013; Engwell et al., 2021; F. Prata and Rose, 2015). Ash particles ingested by aircraft turbines

can soften at the operating temperatures found inside the engine (1,200–2,000°C). Once hot and sticky, these particles may adhere to internal engine components, degrading the performance and eventually causing catastrophic failures (Giehl et al., 2017; Song et al., 2016).

A multidisciplinary investigation of tephra life cycle using field observations, laboratory experiments, and numerical modeling is critical to understanding the various processes that produce tephra clasts and determine their fate, including generation inside the volcanic conduit, injection into the atmosphere through volcanic plumes, long-scale transport, and sedimentation on the ground. A better understanding of these mechanisms has implications for our ability to mitigate the risk posed by tephra plumes and clouds on human infrastructure and natural ecosystems. Significant progress in our comprehension of tephra life cycle has occurred since the 1960s, coinciding with the rise of quantitative volcanology in contrast to the previous qualitative and descriptive approach. This advancement has been facilitated by collaborative efforts across various disciplines, particularly in physics, mathematics, statistics, and computational science. First efforts to describe the thermodynamics and fluid dynamics of volcanic plumes came from observations at Heimaey and Stromboli volcanoes in the 1970s (e.g., Blackburn et al., 1976; Sparks & Wilson, 1976; L. Wilson, 1976; L. Wilson et al., 1978). These pioneer studies opened up the numerical modeling of explosive eruptions and related features (Armienti et al., 1988; Carey & Sigurdsson, 1986; Valentine & Wohletz, 1989; Woods, 1988). In the decades since, we have greatly advanced in our capacity to develop numerical models to simulate complex natural phenomena, such as the rising of volcanic columns and the transport and deposition mechanisms of tephra particles (Costa, Suzuki, et al., 2016; Folch, 2012; Y. J. Suzuki et al., 2016). Such tools are today fundamental in the assessment of the hazard due to explosive eruptions and are used worldwide to provide forecasts of the movement of volcanic clouds. Moreover, in recent decades, there has been a radical improvement in our ability to observe plumes and clouds using satellite and ground-based technologies. The advent of satellite observations in the 1980s marked a turning point, as unprecedented data of explosive plumes and clouds began to be collected (e.g., Holasek et al., 1996; Krueger, 1982; Matson, 1984; A. J. Prata, 1989a, 1989b). These observations, especially of large eruptions, have played a crucial role in advancing our understanding of the dynamics of tephra, ranging from plume rising and the spread of the umbrella cloud to the transport and deposition of volcanic particles.

Explosive eruptions of different styles that occurred at Mount St. Helens (USA 1980, VEI 5), El Chichón (Mexico 1982, VEI 5), Pinatubo (Philippines 1991, VEI 6), Soufriere Hills (Montserrat 1995, VEI 3), Eyjafjallajökull (Iceland 2010, VEI 3), among others, have had a profound impact on modern volcanology, shaping the way volcanic crises are addressed in terms of risk management. Recently, the 2022 eruption of Hunga volcano (Tonga, VEI 5–6) entered the list of profoundly impactful eruptions (Dalal et al., 2023; Poli & Shapiro, 2022). Advances in observational technologies have documented the highest plume (57 km; Proud et al., 2022), the most lightning activity of any known meteorological event (>2,600 flashes/min; Van Eaton et al., 2023), and produced full 2D maps of plume height over 10-min intervals that were accurate to less than 1 km, thanks to stereo image analysis from two geostationary satellites (Podglajen et al., 2022; Van Eaton et al., 2023). With each eruption, especially large events, our constantly improving technologies allow us to observe and to understand processes of plume development in greater detail, and to expand our understanding of additional processes such as: tsunamigenesis triggered by volcanic eruptions (Lynett et al., 2022), generation of atmospheric waves (Wright et al., 2022), impact on the climate system (S. Jenkins et al., 2023), and lofting of volcanic clouds due to aerosol-radiation interaction (Muser et al., 2020).

The variety of volcano locations, eruption styles, and general conditions (meteorological and environmental) make it impossible to define a single strategy for dealing with volcanic eruptions in terms of monitoring and forecasting. An efficient monitoring network enables early warnings and enhances the characterization of eruption source parameters (ESPs), such as column height, mass eruption rate (MER), and eruption duration. This, in turn, implies that numerical forecasting of tephra dispersal can be set more precisely. Volcanoes that erupt frequently are generally well monitored and are the subject of dedicated analyses of hazard assessment. Mount Etna in Italy is an example, exhibiting frequent eruptions ranging from weak Strombolian events to lava fountains producing columns up to 10 km high (Andronico, Cannata, et al., 2021). In contrast, some volcanoes erupt unexpectedly after periods of quiescence. In such cases, serious challenges may arise for risk managers due to the lack of hazard assessment and risk mitigation plans. For example, the sub-Plinian eruption of Calbuco (Chile, 2015) occurred suddenly after 54 years of quiescence and with only less than 3 hr of precursor seismic activity, generating two sub-Plinian phases with column heights over 15 km in less than 12 hr (Romero et al., 2016). This eruption prompted a state of emergency in Chile, causing significant damage to

infrastructure, buildings and economic activities due to the consistent accumulation of tephra (Hayes, Calderón, et al., 2019), and disrupting local air travel. There are cases where distinctive eruption and meteorological conditions challenged the response to weak intensity events even at well monitored volcanoes, as seen for the eruption of the Eyjafjallajökull volcano (Iceland, 2010). The volcanic ash risk management guidance for Europe prior to 2010 stipulated that an airspace should be closed when ash is observed or forecast to be in that area, regardless of contamination levels. In 2010, the 39-days Eyjafjallajökull eruption released at least 70 Tg of very fine ash into the atmosphere (M. T. Gudmundsson et al., 2012). The combination of the volcano location, the height of the eruptive column (between 3 and 10 km) and the prevailing westerly and north-westerly winds caused an unprecedented impact on global air traffic, with the closure of central Europe airspace from April 15 to 21 (M. T. Gudmundsson et al., 2010). To limit the economic losses, a new policy allowing flight operations in low concentrated ash contaminated regions emerged and these guidelines are still valid today in the European and north Atlantic region (ICAO, 2024).

In this review, we comprehensively examine the current understanding of tephra plumes and clouds, encompassing their generation and the latest monitoring and forecasting strategies. We elucidate the eruptive mechanisms that lead to tephra formation and investigate the dynamics of plume rise and cloud dispersal (Section 2). In particular, Section 2.1 provides a description of the fragmentation mechanisms that lead to tephra generation, while Section 2.2 describes the physics of volcanic plumes. The transport of tephra into the atmosphere until its final deposition on the ground is illustrated in Section 2.3, where we present gravitational settling, wet deposition, aggregation, settling-driven gravitational instabilities (SDGIs), and resuspension. Subsequently, we provide an overview of the state-of-the-art techniques for monitoring tephra, employing ground-, airborne-, and space-based instruments (Section 3). For each method, we highlight the strengths and limitations and illustrate its applicability to monitor tephra plumes and clouds produced by volcanic eruptions of different styles. Moving on to Section 4, we discuss the numerical modeling of tephra plumes and clouds, focusing on the numerical models currently in use (Sections 4.1 and 4.2), as well as the most recent procedures for tephra forecasting, which are applied both for operational purposes (i.e., during an ongoing eruption) and long-term hazard assessment (Sections 4.3, 4.4, and 4.5). We note that this review focuses on tephra in the atmosphere; therefore, topics such as the description of tephra deposits and the hazard assessment of tephra on the ground are not covered. Finally, in Section 5, we present general conclusions and discuss future trends for each of the main topics addressed in the paper (ground- and satellite-based monitoring and numerical modeling). When discussing monitoring and forecasting strategies, we emphasize their practical application in real-time scenarios. In this context, “real-time” refers to the capability of collecting observational data and generating numerical forecasts within a timeframe consistent with the progress of the investigated eruption. This enables timely decision-making to mitigate the impacts associated with tephra plumes and clouds. Finally, in the text, we use the term “tephra” when referring to the complete spectrum of particle sizes, while the term “ash” is specifically employed for discussions and applications involving only the finest tephra particles ( $\leq 2$  mm).

## 2. Generation and Dynamics

The injection of tephra into the atmosphere is the manifestation of different styles of explosive volcanism, each producing plumes with specific features and associated hazards. Traditionally, scientists classify explosive eruptions as Hawaiian, Strombolian, Vulcanian, Plinian (and sub-Plinian), and phreatomagmatic (Sigurdsson et al., 2015).

Hawaiian and Strombolian eruptions are characterized by magmas with low viscosity (lower viscosity for Hawaiian than Strombolian) and represent the least violent events. They are transient explosions (lasting seconds) that produce plumes reaching heights from hundreds of meters to a few kilometers (very rarely reaching the tropopause). Due to the low eruption columns and the coarseness of the ejecta, their dispersal potential is limited, causing the majority of clasts to be deposited within a few hundred meters of the vent. Vulcanian eruptions are typically short-lived events (lasting seconds to minutes) and usually do not last long enough to produce sustained columns. However, if explosions occur in rapid succession, sustained columns can form, with resulting plumes reaching heights of several kilometers (up to 20 km). In this case, relevant dispersal of finer material can occur, similar to more energetic events (Plinian or sub-Plinian). Plinian and sub-Plinian eruptions produce sustained volcanic columns that rise several kilometers high (tens of kilometers), injecting tephra into the atmosphere (often reaching the stratosphere) and spreading it over wide areas. They represent the more energetic events and those with higher hazards in terms of tephra dispersal. Phreatomagmatic eruptions result from the interaction between

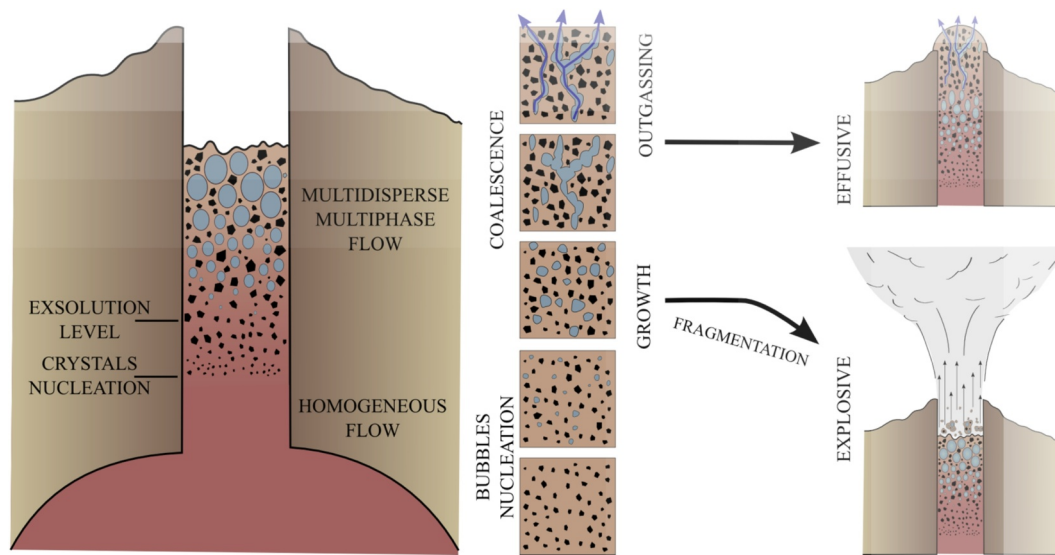


**Figure 3.** Schematic representation of the processes occurring in a volcanic conduit that can lead to the fragmentation of magma, and thus to an explosive eruption generating a volcanic column. When magma rises, bubbles nucleate, and their growth is constrained by the elevated viscosity of silicate melts, leading to an accumulation of pressure. When gas loss through permeable pathways is limited, gas overpressure can break the thin films surrounding the bubbles and fragment the magma. This process transforms the initial continuous liquid phase with dispersed gas bubbles and crystals into a high-velocity gas phase with dispersed magma fragments. The presence of crystals on one hand facilitates the nucleation of gas bubbles, thereby intensifying the explosiveness of an eruption. On the other hand, a high crystal content increases the viscosity of magma affecting the ability of gas bubbles to rise and expand.

magma and external water, leading to complex and often highly explosive events. Plumes generated by phreatomagmatic eruptions are highly heterogeneous, ranging from weak plumes poor in tephra to sustained columns typical of Plinian styles.

### 2.1. From Magma Fragmentation to Tephra Plumes

The genesis of volcanic plumes lies deep within volcanic conduits, in a process known as magma fragmentation (Cashman & Scheu, 2015; Gonnermann, 2015; T. J. Jones et al., 2022). Magma fragmentation is the disintegration of magma into pyroclastic material. This process mostly occurs when the pressure of the dissolved gasses in the magma (mainly water vapor, carbon dioxide, and sulfur gasses) exceeds its tensile strength, causing it to shatter into fragments. These fragments, called tephra, are then expelled into the atmosphere, eventually giving rise to buoyant plumes that may further evolve into volcanic clouds (Mackie et al., 2016). Thus, while our observations are atmospheric, the cause is rooted in the depths of volcanic conduits, where a continuous liquid phase with dispersed gas bubbles and crystals rises and transforms into a high-velocity gas phase with dispersed magma fragments (Figure 3).

The composition of magma can affect the fragmentation and the resulting eruptive plume in several ways. First, the fragmentation process strongly depends on the amount of gas and crystals, which assume a pivotal role in the dynamics of magma fragmentation. As magma rises its pressure decreases and the gasses dissolved in the melt phase exsolve, giving rise to the formation of gas bubbles through homogeneous nucleation from the silicate melt, that is, without preferential nucleation sites as crystal (Gonnermann & Manga, 2007; de' Michieli Vitturi & Aravena, 2021). The growth of these bubbles is constrained by the elevated viscosity of silicate melts, leading to an accumulation of gas pressure within the bubbles. This gas overpressure, if not released via permeable pathways, has the potential to break the thin films surrounding the bubbles, thereby fragmenting the ascending magma. Crystals within the magma matrix also exert a significant influence over the process of magma fragmentation. On the one hand, the presence of crystals facilitates the nucleation of gas bubbles (heterogeneous nucleation; Gardner et al., 2023), thereby intensifying the explosiveness of an eruption. On the other hand, a high crystal content increases the overall viscosity of the magma and can affect the ability of gas bubbles to rise and expand, potentially leading to higher gas overpressure and more explosive fragmentation (Moitra et al., 2018). Hence, both gas and crystals are inherent factors that govern the intricacies of magma fragmentation (Mourtada-

Bonnefoi & Mader, 2004), ultimately determining the style and intensity of explosive eruptions and the injection of tephra in the atmosphere and thus, ultimately, the hazard footprint.

The genesis of the erupting magma also affects its fragmentation. At divergent boundaries, magma is brought to the surface from the deeper mantle by convection cells and it has low silica (because there is little interaction with crustal materials), resulting in low viscosity. In addition, magmas from divergent boundaries generally have a low volatile content. Conversely, at subduction zones, where the oceanic crust subducts beneath the thicker continental crust, interaction with high-silica crustal rock is more significant resulting in magmas with larger volatile and silica content, and thus with a higher viscosity. As stated above, these differences in viscosity and volatile level have significant implications for the fragmentation and the eruptive styles. It has also been found that magma composition affects the typical MER of explosive eruptions, because of a strong relationship between magma rheology and conduit stability. To maintain stability, dacitic and rhyolitic explosive eruptions need conduits with diameters significantly larger than those for phonolitic and trachytic eruptions. This difference results in the higher eruption rates typically seen in dacitic and rhyolitic explosive events, leading to higher volcanic columns (Aravena et al., 2018).

Interaction with external water can cause magmas that would normally erupt lava flows to explode into tephra particles or convert normally explosive eruptions into more energetic events. A notable example is the 1886 Mount Tarawera eruption, in New Zealand (Houghton et al., 2004). The violent character of this eruption came from the interaction of the rising basaltic magma with both cold groundwater and superheated geothermal fluids, resulting in the youngest known basaltic Plinian eruption, with ash dispersed hundreds of kilometers away from the vent. This behavior is quite unusual for basaltic magmas because basaltic explosive eruptions are commonly Strombolian or Hawaiian in style, ranging from mild explosions to more energetic lava-fountains, with the tephra released in the atmosphere impacting mostly proximal areas. Despite that, a few other basaltic Plinian eruptions occurred in the past (e.g., the 60 ka Fontana Lapilli (FL) and 2.1 ka Masaya Triple Layer eruptions of Las Sierras-Masaya volcano (Nicaragua), the 122 BCE Mount Etna eruption (Italy), or the 2017–2018 CE eruption of Ambae (Vanuatu)). However, not all these Plinian eruptions are associated with interaction with external water. In fact, it has been shown that basaltic magma, when rapid and substantial microlite crystallization occurs and high-volume fraction of crystals are reached, can undergo brittle fragmentation despite the relatively low viscosity of the melt (Bamber et al., 2020).

For intermediate viscosity magma, like andesite and dacite, the degassing through permeable paths creates sometimes a dense plug at the top of the conduit, which can seal it and lead to the buildup of a high overpressure at the base of the plug (Diller et al., 2006). This overpressure can eventually disrupt the plug, exposing the inner magma to a pressure drop and initiating a fragmentation wave moving downward inside the conduit, which ultimately produces a Vulcanian eruption. Even for Vulcanian eruptions, fragmentation plays a leading role in controlling density, velocity, and mass discharge rate of the gas-particle mixture, all factors which can significantly affect the eruptive column. Alatorre-Ibargüengoitia et al. (2011) obtained through laboratory experiments a relationship between the fragmentation speed and the ejection velocity of the gas-particle mixture.

Magma fragmentation does not only control the style and intensity of explosive eruptions, but also the morphology and size of the resulting tephra (Jordan et al., 2014; Kaminski & Jaupart, 1998; Walker, 1981). Basaltic magmas with a low content of crystals are characterized by a fluidal fragmentation, which produces elongated fibers (Pele's hair) as well as vesicular ash fragments that preserve the original melt interstices between bubbles. Even highly viscous and crystal-poor silicic magma, which generally fragments in a brittle way, produce ash particles that retain the shape of interstitial melt between the expanding bubbles; because of this, ash shapes range from flat plates to cusped shards to pumiceous micro-fragments and dense crystals. In contrast, when the interaction of external water with mafic magma leads to magma fragmentation, the resulting ash particles vary from vesicular to dense, with the latter being generally smooth and equant (Mackie et al., 2016). As regards the particle size resulting from the primary fragmentation, it has been shown that cumulative grain size distribution is well described by a power-law relationship, where the power-law exponent, also known as the fractal dimension of the distribution, is correlated with the potential energy at fragmentation (Fowler & Scheu, 2016; Turcotte, 1997). Secondary fragmentation, which can occur both within the conduit and in the jet region of the plume (T. J. Jones & Russell, 2017), can modify both the shape and size of the particles, by rounding them and decreasing the average size, and by increasing the fractal dimension of the grain size distribution.

## 2.2. Plume Dynamics

During explosive eruptions, magma and gas exit volcanic vents as negatively buoyant gas-particle jets, driven upward by momentum. Their negative buoyancy causes them to decelerate and eventually stall, collapsing back onto the flanks of the volcano. However, if they entrain enough air and heat it, they become positively buoyant and rise high into the atmosphere. Continued mixing with air causes them to cool, lose buoyancy, and then collapse gravitationally to a lower level, where they advect downwind or spread laterally as an umbrella cloud. Buoyant plumes are of particular interest because they are responsible for the widespread dispersal of volcanic ash.

Four parts can be defined for a typical plume (Figure 4a): (a) a momentum-driven gas-thrust basal region; (b) a buoyant, convective thrust region; (c) an overshooting top where the plume has lost buoyancy but continues to rise and, finally, (d) a collapsing and spreading region.

### 2.2.1. The Gas-Thrust Region

Most volcanic eruption plumes leave the ground surface as vertical jets (Figure 4a—inset). Pressures in the shallow subsurface that drive these jets can be several megapascals or more, and the pressure gradient between surface and near surface is almost always too great for pressures in the flowing mixture to drop by viscous pressure losses in the fluid. Thus, at some near-surface choke point, their velocity accelerates to the sound speed of the mixture, which ranges from several tens to hundreds of meters per second (Bennett, 1971; Kieffer, 1989; Kieffer & Sturtevant, 1984; McGetchin & Ullrich, 1973). Above the choke point, the mixture accelerates to supersonic velocity before going through a series of shock waves and pressure fluctuations, and eventually equilibrates to atmospheric pressure. The velocity after equilibration depends on the vent geometry and on other parameters but likely ranges from several tens to a few hundred meters per second (Koyaguchi et al., 2010; Woods & Bower, 1995). Assuming the gas that drives volcanic jets from the vent consists only of volatiles that have exsolved from the magma, all erupting mixtures will be negatively buoyant (Sparks & Wilson, 1976). Negative buoyancy and air drag cause them to decelerate with elevation. Without air entrainment, the jet would rise only a few hundred to a few thousand meters until its initial kinetic energy is converted to elevation potential energy. It would then collapse back to the ground surface and propagate outward as a pyroclastic density current (PDC). Along its perimeter, however, the jet shears against the adjacent air, producing eddies that curl outward and then back into the jet, carrying ambient air with them (Figure 4a—inset). The eddies develop within a boundary layer that widens with elevation and, as the boundary layer widens, eddies grow wider and engulf more air until, at several vent diameters above the ground surface, the boundary layer has worked its way into the jet core (Figure 4a). At greater height, the jet develops a roughly Gaussian velocity profile (when averaged in time) (Wynanski & Fiedler, 1969, Figure 1; Pope, 2000, Figure 5.15), though this may be modified by crosswinds (Aubry et al., 2017) or partial collapse (Esposti Ongaro and Cerminara, 2016).

The amount of air entrained into the jet is the key factor that controls whether an erupting column transforms into a buoyant plume or collapses. Much research has been dedicated to understanding which factors control the entrainment rate (Aubry et al., 2017; Degruyter & Bonadonna, 2013; Devenish et al., 2010; Dürig et al., 2023; Falcone & Cataldo, 2003; Hoult & Weil, 1972; Huq & Stewart, 1996; Kaminski et al., 2005; Liepmann, 1991; List, 1982; Patrick, 2007; Ricou & Spalding, 1961; Solovitz et al., 2011; Y. J. Suzuki & Koyaguchi, 2010, 2015; Turner, 1986). In general, higher speed jets produce faster eddies, which entrain air at a greater rate (Jessop & Jellinek, 2014; Morton et al., 1956). In the near-vent region, experiments and models suggest that the entrainment rate also depends on vent geometry (Y. J. Suzuki et al., 2020), distance from the vent (Solovitz & Mastin, 2009), vent overpressure (Ogden et al., 2008; Solovitz et al., 2011), and jet buoyancy (Kaminski et al., 2005). For jets in crossflow, the entrainment rate is also thought to increase linearly with crossflow velocity (Hewett et al., 1971; Hoult et al., 1969). Air entrainment along the jet perimeter has significant implications for entrainment in jets of different sizes. The jet perimeter increases linearly with the jet radius  $r$  whereas the MER increases with  $r^2$ . Thus, as a fraction of erupted volume flux, small plumes entrain more air along their margins than big plumes. As vent diameter grows (by erosion for example), it becomes increasingly difficult to entrain enough air to develop buoyancy. In the largest eruptions, column collapse becomes a dominant process, producing extensive, laterally emplaced pyroclastic deposits known as ignimbrites (Woods, 1988).

A collapsed column that moves away from the vent as a PDC may continue to mix with air along its upper margin (Figure 4b). Mixtures of hot air and fine, elutriated ash may rise buoyantly to form coignimbrite plumes, phoenix

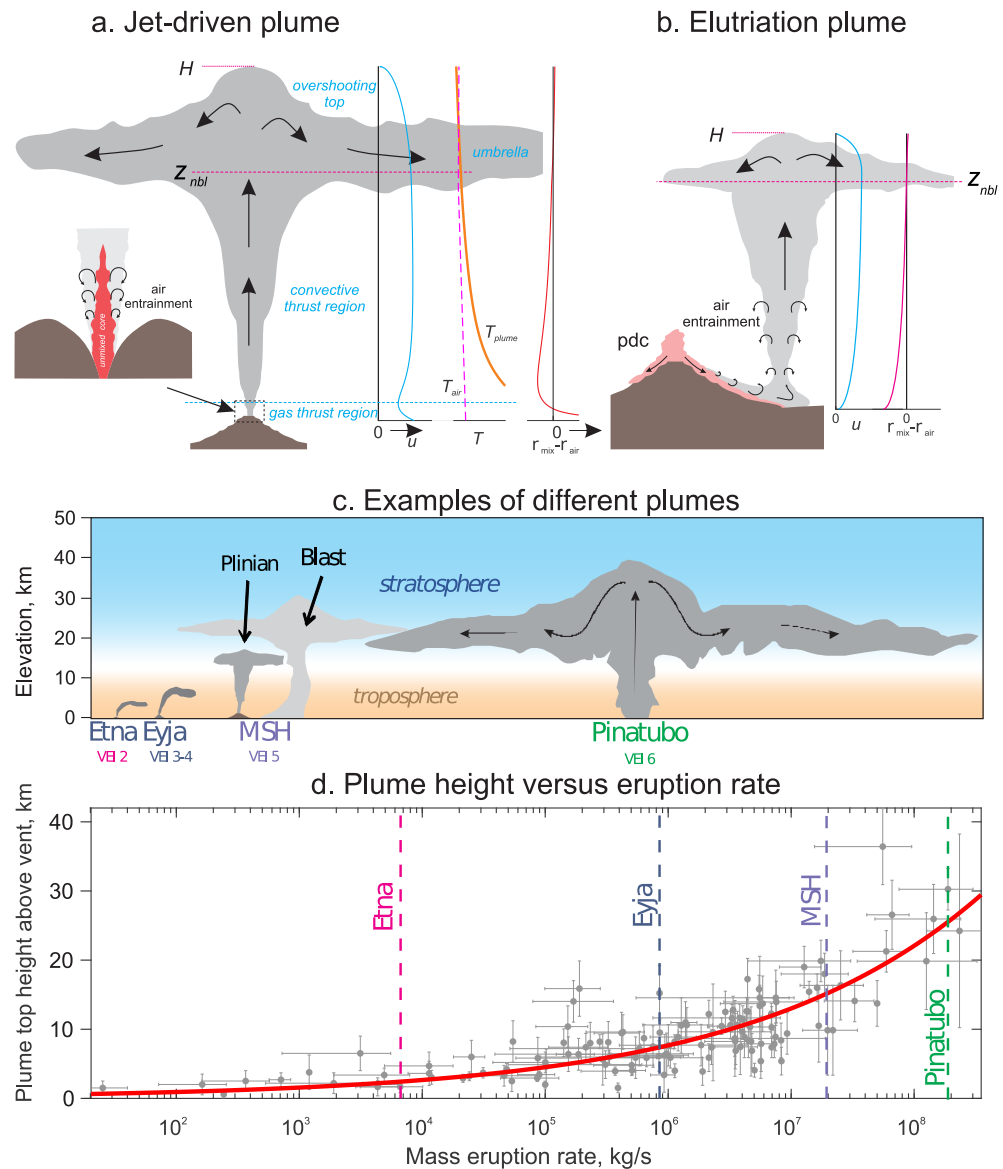


**Figure 4.** (a) Schematic illustration of the anatomy of a jet-driven plume, showing the gas-thrust region, the convective thrust region, the overshooting top, and (for large eruptions) the umbrella cloud. After rising, the plume subsides back to the neutral buoyancy elevation ( $z_{nbl}$ ) and spreads. Inset to left shows a close-up of the vent region with an unmixed core of magmatic material and gas (red), air entrainment along the jet margins (circulation arrows), and a mixed region of magmatic material and entrained air (gray). Also shown on the right are profiles of average ascent velocity ( $u$ ), temperature of the plume ( $T_{plume}$ ) and surrounding air ( $T_{air}$ ), and density of the plume mixture ( $\rho_{mix}$ ) minus that of the ambient air ( $\rho_{air}$ ). (b) Shows a coignimbrite plume rising from a pyroclastic density current. Profiles of velocity and plume density minus air density are also shown. (c) Shapes of some well-known plumes as a function of eruption size: Etna 2001 (Scollo et al., 2007), Eyjafjallajökull 2010 (Arason et al., 2011; M. T. Gudmundsson et al., 2012), Mount St. Helens, 18 May 1980, including both the Plinian column between 0900 and 1700 local time (left) and the coignimbrite plume that rose from 0845 to 0910 local time (right, Sparks et al., 1986), and the giant Pinatubo plume and umbrella cloud (Holasek et al., 1996; Koyaguchi & Tokuno, 1993). (d) Plume height versus mass eruption rate (MER) for 130 eruptions listed in the Independent Volcanic Eruption Source Parameter archive (IVESPA, Aubry et al., 2021). Heights and uncertainties are derived as described in IVESPA. Dashed lines of different colors correspond to the approximate MERs of eruptions illustrated in (c). The red line is the best-fit power-law estimation of plume top height  $H$  given MER,  $H = 0.345MER^{0.226}$  (Aubry, Engwell et al., 2023), where MER is in kg/s and  $H$  is in kilometers above the vent.

clouds, or elutriated ash clouds. These plumes differ from vent-fed plumes in that they do not contain a lower, negatively buoyant gas-thrust region. They also generally contain much finer ash than vent-fed plumes (Sparks et al., 1986, 1997, Section 4.8). Two- and three-dimensional modeling studies have found that transitional behavior, in which columns partially collapse and phoenix clouds rise from PDCs, develop in cases where the amount of gas entrained into the jet is marginally sufficient to develop buoyancy (Neri et al., 2002). Complex columns involving simultaneous collapse and buoyant rise have also developed in large, wet eruptions (Van Eaton et al., 2012a). Choked flow can also cause columns to oscillate with time, collapsing and rising over periods of minutes (Neri et al., 2002; Ogden et al., 2008; Y. J. Suzuki et al., 2016).

### 2.2.2. The Convective Thrust Region

For plumes that attain buoyancy, their upward motion is driven by heat. The buoyancy force is equal to the plume's cross-sectional area multiplied by the density difference between the plume and the surrounding air. Thus, all other things being equal, hotter plumes (which have lower density) rise faster than cooler ones. Bigger plumes cool more slowly with height, retain their buoyancy longer, and rise higher than smaller ones. In a stably stratified quiescent atmosphere, the height of the plume  $H$  is theoretically proportional to the fourth root of buoyancy flux (i.e., heat flux) (Morton et al., 1956). Magmatic absolute temperature varies by only about 20%–30% from the coolest to the hottest magmas. Similarly, vent-level atmospheric density, governed by atmospheric temperature and pressure, also varies by only about ~20%–30%. By contrast, MER can vary by at least five orders of magnitude (Settle, 1978; L. Wilson et al., 1978). Thus, we expect the heat flux that drives volcanic plumes to be controlled mainly by MER. Several empirical compilations of plume height and eruption rate support the proportionality  $H \propto \text{MER}^{1/4}$  (Mastin et al., 2009; Sparks et al., 1997; L. Wilson et al., 1978) (Figure 4d). This relationship is widely used to estimate MER for dispersion modeling (e.g., Aubry, Engwell et al., 2023; F. M. Beckett et al., 2020; Mastin et al., 2009), although uncertainty in MER for a given  $H$  is close to an order of magnitude, and the relationship ignores atmospheric and other effects, which are described below.

*Thermal lapse rate* is one such atmospheric influence. Plumes are buoyant because they are warmer than surrounding air, yet they cool adiabatically as they rise. In the troposphere, the ambient atmosphere also cools with elevation, making it easier for plumes to remain buoyant. In the stratosphere, however, the temperature increases with elevation while the plume continues to cool. This adverse atmospheric temperature gradient hinders ascent above the tropopause, requiring a greater heat flux to add a given increment of plume height. Adiabatic cooling may also cause stratospheric plumes to be cooler than the surrounding air, or air at any elevation at that location. This phenomenon, known as undercooling, has been detected in thermal satellite images at several eruptions and taken as an indication that the plume has risen into the stratosphere (Woods & Self, 1992).

*Atmospheric moisture* is a second atmospheric influence. Plumes that entrain moist ambient air will also cool adiabatically as they rise, but their cooling is moderated by the release of latent heat as water condenses. Like thunderheads, volcanic plumes that condense as they rise will remain warmer and buoyant to greater elevation than similar plumes that entrain dry air (Woods, 1993). In humid, tropical environments, this process can drive small plumes to rise to the tropopause before stalling (Tupper et al., 2009).

*Wind* is a third such influence. During the 2010 eruption of Eyjafjallajökull, plume height was seen to correlate inversely with wind speed (Woodhouse et al., 2013). Wind tends to bend the plume over, reducing its height. Wind also increases entrainment of air into the plume, increasing the mass that must be lifted without increasing the thermal energy available to lift it. These two effects result in lowering plume height for a given MER. Several studies highlight that wind effects result in serious underestimates of MER if empirical height-rate relations are used without consideration of wind (Bursik et al., 2012; Degruyter & Bonadonna, 2012; Woodhouse et al., 2013).

*External water* added at the vent can also influence plume height. Cold seawater or groundwater adds to the mass that must be lifted by the plume. Water can also cool the plume and, through expansion, convert some of the thermal energy that drives plume rise to explosive kinetic energy (Zimanowski, 1998). For eruptions involving MERs less than about  $3 \times 10^8$  kg/s, modeling studies (Koyaguchi & Woods, 1996; Woods, 1993) found that the vapourized water returns most or all its heat to the plume as it rises and condenses, resulting in little or no change in plume height. For larger eruptions however, the addition of water does reduce plume height by increasing plume density (Koyaguchi & Woods, 1996). These findings ignore the effects of surface water in suppressing exit velocity or gas exsolution. Studies that consider them (Rowell et al., 2022) found that a water depth of 50–100 m can increase the MER required for plumes to reach the tropopause by an order of magnitude.

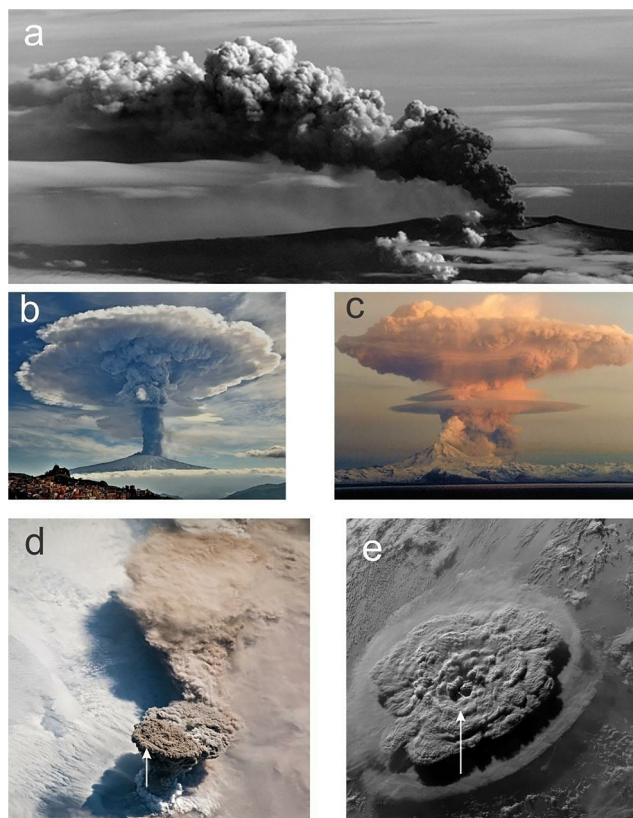


**Figure 5.** (a) The 4 May 2010 weak plume at Eyjafjallajökull. The plume on this day rose to several kilometers and then blew downwind without dropping greatly in elevation. Icelandic Meteorological Office image by Thorstein Jonsson. Published with permission. (b) Photograph by G. Famiani of a strong plume and umbrella cloud from an eruption of Mount Etna on 4 December 2015. Published with permission. (c) Thermal and umbrella cloud produced by elutriation of ash and gas from a pyroclastic density current (PDC) at Redoubt Volcano, Alaska, on 21 April 1990. Photo by R. Clucas. Used with permission. Skirt clouds form as moist air is drawn toward the rising plume, rises and condenses. The plume is offset to the right of the volcano because it rose from the PDC rather than the vent. (d) International Space Station image of the eruption of Raikoke volcano, Kuril Islands, 21 June 2019. Upwind stagnation point is shown by the arrow. Ash from earlier, less vigorous phases of the eruption trails off downwind toward the top of the image. (e) GOES-17 visible image of the 15 January 2022 umbrella cloud from Hunga volcano, Tonga. Arrow points to one of several gravity waves propagating through the cloud. A white ice-rich cloud is visible below the main umbrella cloud.

*Steam* rising from lava or PDCs mixing with water can boost a plume with little or no ash to great heights. This process was observed or inferred at Kīlauea in 2020 (Cahalan et al., 2023), Fukutoku-oka-no-ba in 2021 (Maeno et al., 2022) and may have contributed to the great height of the 57-km-high, ash poor Hunga plume in 2022 (Mastin et al., 2024).

### 2.2.3. Overshoot, Eruption Size and Plume Shape

Plumes pass their elevation of neutral buoyancy ( $z_{nb}$ ) at around the point in their trajectory where their buoyant ascent velocity is highest. Plumes whose ascent velocity is less than or comparable to that of ambient winds will be bent over to produce weak or bent plumes (Figure 5a), while those that ascend fast relative to wind speeds will produce vertical or strong plumes (Figure 5b). Model results (Costa, Suzuki, et al., 2016) suggest that a plume from a medium-sized eruption of about  $10^6$  kg/s may have an ascent velocity of several tens of meters per second at the neutral buoyancy elevation, whereas a Pinatubo-sized eruption ( $\sim 10^9$  kg/s) may ascend at more than 200 m/s. By comparison, tropospheric wind speeds are typically in the range of meters per second to tens of meters per second. Thus, when winds are present, eruptions ejecting less than about  $10^6$  kg/s of magma are more easily bent (Figure 5a), than those ejecting more than  $10^8$  kg/s (Figure 4c). The 15 June 1991 Pinatubo plume, for example, rose to 35–40 km elevation through the tropospheric winds of typhoon Yunya with seemingly little deflection by wind (Wolfe & Hoblitt, 1996).

The greater ascent velocity of large plumes also affects the height of the overshooting top. Bent plumes from smaller eruptions rise to their maximum height and then level off (Figure 5a) or slightly decrease in height (Arason et al., 2011; Figure 5) as they spread downwind. Morton et al. (1956) suggested a theoretical neutral buoyancy elevation that is about 76% of the total plume height. Empirical compilations give the same number on average (Aubry et al., 2021). But observations also suggest that big eruptions have greater overshoot than smaller ones. Pinatubo in 1991, for example, ejected ash to 35–40 km, then dropped more than 10 km, to feed an umbrella whose top lay at about 25 km elevation (Fero et al., 2009; Holasek et al., 1996). At Hunga in 2022, ash reached 50–57 km, then dropped below 35 km before spreading (Van Eaton et al., 2023).

The negative buoyancy of the overshooting top can lead to unstable fluctuations in plume-top height (Friedman et al., 2007). Three dimensional simulations of a Pinatubo-sized eruption show fluctuations of 5–10 km over several minutes (Y. J. Suzuki & Koyaguchi, 2009), even when the eruption rate is constant. Fluctuations may have been responsible for top-height estimates ranging between 35 and 40 km at Pinatubo (Holasek et al., 1996) and changes of more than 15 km over 10-min intervals during the 2022 eruption of Hunga volcano (Van Eaton et al., 2023).

#### 2.2.4. Gravitational Spreading

Gravitational collapse from the overshooting top causes the ash to drop to an elevation of neutral buoyancy. When the eruption rate is low and wind speeds are high, the ash is advected downwind with little radial spreading. At higher MERs, however, the ash spreads laterally, including in the crosswind and upwind directions. Upwind, the ash spreads until the magnitude of the radial velocity vector equals the wind speed at that elevation, at which point it stagnates and the cloud forms an anvil shape in cross section (Carey & Sparks, 1986) (Figure 5d, arrow). The most powerful eruptions produce nearly circular umbrella clouds that are not strongly influenced by ambient winds (Figure 5c). In the largest (VEI 7–8) eruptions, their outer edges may spin in response to Coriolis forces (Baines & Sparks, 2005). During vigorous umbrella growth, fluctuations in the plume-top height propagate downward and outward into the growing umbrella cloud as gravity waves (Figure 5e, arrow). During the 15 January 2022 eruption of Hunga volcano, the gravity waves were accompanied by outward-propagating rings of lightning within the cloud (Van Eaton et al., 2023).

The radius  $r$  of umbrella clouds has been estimated theoretically to grow with time  $t$  at a rate of  $r \propto t^{1/3}$  for clouds rising from discrete sources, and  $r \propto t^{2/3}$  for clouds fed from sustained sources (Sparks et al., 1986). Umbrella growth under different relationships between buoyancy and drag, may result in different exponents (Pouget et al., 2016), but in general, umbrella clouds observed in recent years from vent-derived plumes have fit well to the  $r \propto t^{2/3}$  relationship (Mastin & Van Eaton, 2020; Van Eaton et al., 2023). For sustained plumes, this relationship can be used to constrain MER (Costa et al., 2013; Pouget et al., 2013). This method has been used more often as modern satellite imagery with good time resolution has become available.

#### 2.3. Tephra Transport, Sedimentation, and Resuspension

A clast inside a plume experiences two opposing forces: the downward force of gravity and the upward drag force exerted on the clast by the rising mixture. The point at which the gravity force and the drag force are equal determines the terminal velocity of the clast. The ascending plume can transport a clast until the height where the vertical velocity of the plume matches the terminal velocity of the clast. At this point, the clast becomes suspended at that elevation and it is unable to ascend any farther. As volcanic plumes exhibit high turbulence, a clast at its suspended height will undergo continuous movement, eventually reaching the edges of the plume. When this happens, it will fall out from the column (as it no longer receives support from the rising mixture) and enter the atmosphere (Carey & Sparks, 1986). Larger clasts with high terminal velocity are lost close to the vent, while smaller clasts (ash particles) are transported at higher altitudes eventually reaching the neutral buoyancy and entering the umbrella cloud. Here, particles, experiencing the high turbulence of the umbrella, are swept sideways by the radial velocities and, as soon as they lose the support of the mixture, they leave the umbrella region and move downwind, forming volcanic clouds that may persist in the atmosphere for days to months. Here the dispersion and sedimentation of tephra particles are mainly governed by wind transport, turbulent diffusion and settling due to gravity, but can also be affected by wet deposition, particle aggregation and SDGIs (Durant (2015) and references therein).

### 2.3.1. Gravitational Settling

The residence time of tephra particles in the free atmosphere (i.e., above the atmospheric boundary layer which is about 1 km thick) is primarily controlled by their gravitational settling velocity. For simplicity, it is commonly assumed that volcanic particles settle at their terminal velocity (i.e., the velocity reached when gravitational, buoyancy and vertical drag forces acting on the particle are balanced) and under dry conditions. Settling velocity depends on the physical properties of tephra particles (size, density and shape) and on the characteristics of the atmosphere. A wide range of variability exists, spanning from settling velocities less than  $10^{-3}$  m/s for fine ash particles to values higher than 10 m/s for lapilli (Bagheri & Bonadonna, 2016). This means that, for example, the finest particles released at 10 km height can remain suspended into the atmosphere for months. The high variability exhibited by tephra particles in terms of size and shape make the quantification of settling velocity challenging and subject to considerable uncertainties. Particularly challenging to estimate is the particle drag coefficient, which is a term in the definition of settling velocity. Drag coefficient is a function of many parameters, in particular Reynolds number (i.e., a nondimensional number indicating the ratio between the inertial and viscous forces acting on a particle) and particle shape. For low values of Reynolds number ( $Re \ll 1$ ), inertial terms are negligible over the viscous ones, and, for spherical particles only, the drag coefficient can be computed analytically as  $24/Re$  (Stokes, 1851). This solution is valid for particles up about 50  $\mu\text{m}$  diameter (fine ash). At higher Reynolds numbers (from  $Re \geq 0.1$  up to  $Re = 10^5$ ), there are no analytical solutions for the drag coefficient, even for spherical particles, and estimates for spherical and nonspherical particles are derived from empirical correlations based on experiment results. One of the first empirical expressions of the drag coefficient specifically developed for volcanic particles of all shapes was proposed by L. Wilson and Huang (1979). Additional formulations valid under different ranges of validity and based on different shape descriptors were proposed over the years by Arastoopour et al. (1982), Clift and Gauvin (1971), Dellino et al. (2005), Dioguardi et al. (2018), Ganser (1993), and others.

Within the atmospheric boundary layer, additional factors influence the deposition of tephra particles, including the effects of terrain, vegetation and meteorological conditions. Near the ground, Brownian diffusion and eddy turbulence effects contribute to the dry deposition velocity for particles up to 100  $\mu\text{m}$  in diameter. However, for larger particles gravitational settling is still the dominant process (Folch, 2012).

### 2.3.2. Wet Deposition

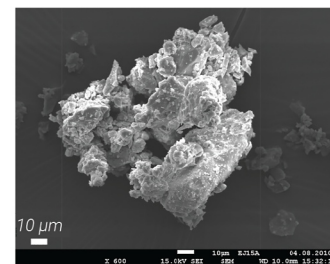
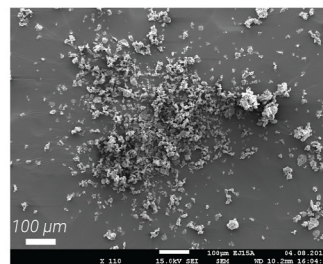
Wet deposition is an additional process responsible for the removal of volcanic particles from the atmosphere. Two types of wet deposition exist: in-cloud scavenging and below-cloud scavenging. In the first case, particles act as cloud (or ice) condensation nuclei or collide with cloud droplets (or ice crystals). When these hydrometeors grow to a certain size, they precipitate, removing the incorporated particles from the atmosphere. In below-cloud scavenging, rain droplets (or ice crystals) precipitating from a cloud collide with particles suspended below the cloud and bring them to the ground surface. Wet deposition can greatly enhance the atmospheric removal of very fine ash particles ( $<30 \mu\text{m}$ ), while for larger particles, gravitational settling is still the main process. The efficiency of wet deposition in removing airborne particles depends on the environmental conditions under which the eruption takes place. For hypothetical eruptions of Merapi volcano (Indonesia), Dare, Potts, and Wain et al. (2016) showed that dry sedimentation removes approximately 10% of volcanic ash from the atmosphere within 24 hr after the eruption, while during high rainfall seasons (December and January), an additional 30% of particles are removed by wet deposition.

### 2.3.3. Aggregation

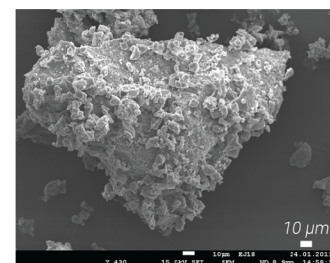
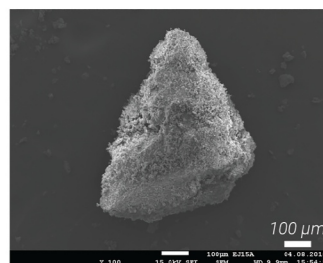
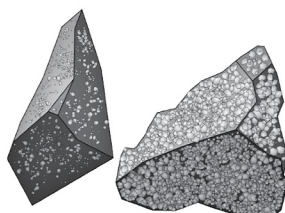
Most ash particles are known to fall as aggregates of various types including particle clusters (ash clusters PC1, coated particles PC2 and cored clusters PC3) and accretionary pellets (poorly structured pellets AP1, pellets with concentric structures AP2, and liquid pellets AP3) (Bagheri et al., 2016; Brown et al., 2012) (Figure 6). Ash clusters (PC1) consist of loosely packed ash particles of similar size ( $<100 \mu\text{m}$ ), while coated particles (PC2) consist of a coarse-ash particle ( $>63 \mu\text{m}$ ) covered by sparse fine-ash particles ( $<63 \mu\text{m}$ ) and cored clusters (PC3) consist of coarse-ash particles covered by a thick shell of fine-ash particles. Accretionary pellets are thought to likely form in humid conditions (wet aggregation) and sediment as roughly spherical clusters with no evident structure (AP1), spherical clusters with concentric layers (AP2, also called accretionary lapilli) or rain drops filled with ash particles of various sizes (AP3). With the exception of AP2 (Burns et al., 2017; Gilbert & Lane, 1994;

**a Particle clusters**

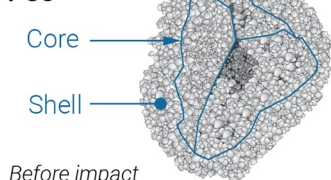
**Particle cluster  
PC1**



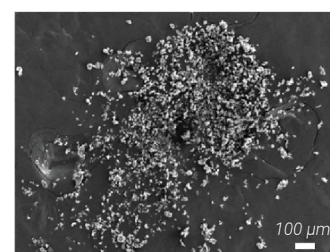
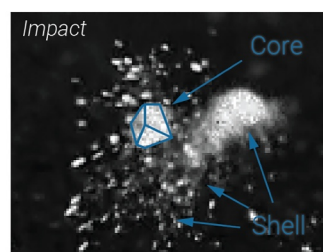
**Coated particle  
PC2**



**Cored cluster  
PC3**

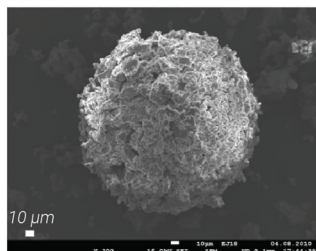


Before impact

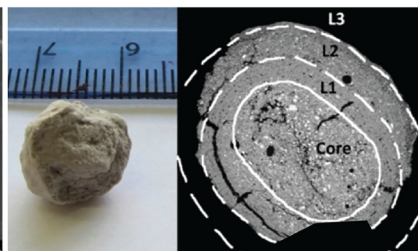


**b Accretionary pellets**

**AP1**



**AP2**



**AP3**

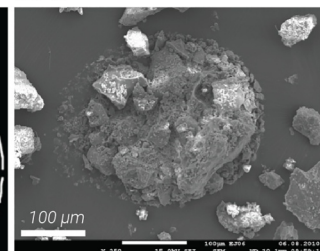


**Figure 6.** Aggregate types: particle clusters (PC1, PC2, and PC3) and accretionary pellets (AP1, AP2, and AP3) (Images modified from Bagheri et al., 2016; Bonadonna et al., 2011; Burns et al., 2017).

Mueller et al., 2016; Van Eaton & Wilson, 2013), all particle clusters and accretionary pellets typically break on impact with the ground and cannot be observed in the deposit (Brown et al. (2012) and references therein). Novel field-observation strategies that involve the combined use of various techniques such as high-speed camera and ash collection on adhesive carbon tape during fallout have provided key insights into the most fragile end-members of aggregates including size, settling velocities and density (Gabellini et al., 2020; Miwa et al., 2018; Taddeucci et al., 2011; Vecino et al., 2022). These investigations combined with detailed studies of tephra deposits have also shown how aggregate size and typology might vary non-systematically with distance from the vent, indicating a complex interaction between the spatiotemporally variable sources of liquid water and ice and the changes in eruptive styles. Aggregate growth and stability in volcanic plumes and clouds are especially

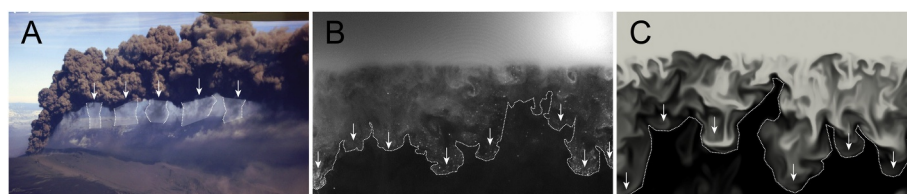


**Figure 7.** Settling-driven gravitational instabilities as observed (a) in the field (May 2010 Eyjafjallajökull eruption; photograph from Eliasson (2020)); (b) in experiments (Fries et al., 2021); and (c) in simulations (Lemus et al., 2021).

complex as they can go through multiple cycles of disaggregation and re-aggregation (e.g., Mueller et al., 2017). In addition, experimental studies suggest that both dry and wet aggregation can occur during the same eruption with electrostatic aggregates forming extremely rapidly and, in wet conditions, accretionary pellets more efficiently scavenging large particles (up to a few hundred microns) due to the associated stronger binding forces (James et al., 2003; Van Eaton et al., 2012b). Given that aggregation associated with ice seems less effective, wet aggregation is likely to be more efficient in the volcanic plume and proximal volcanic cloud where particle concentrations and liquid water contents are higher (possible formation of hydrometeors) (Costa et al., 2010). Nonetheless, hail-like growth of ash aggregates dominating ash sedimentation has also been observed to especially occur in case of wet plumes characterized by sustained updrafts (keeping particles aloft long enough to collide and aggregate) and reaching atmospheric levels colder than  $-20^{\circ}\text{C}$  (Durant et al., 2008; Van Eaton et al., 2015; Wallace et al., 2013). These conditions were met during the eruptions of Grímsvötn in 2011, Eyjafjallajökull in 2010, and Mount St. Helens in 1980. Indeed, volcanic hail was observed from each of these eruptions. Recent field observations have also demonstrated the electrical multipolar nature of ash aggregates and the key role played by multipoles in the formation of clusters in the absence of a primary liquid phase (Pollastri et al., 2022). Depending on cluster size and porosity, particle aggregation can simultaneously cause premature fallout of fine ash and delayed sedimentation (rafting effect) of the associated aggregate cores (typically in the coarse-ash size range) (Rossi et al., 2021).

### 2.3.4. Settling-Driven Gravitational Instabilities (SDGIs)

Premature fallout of volcanic ash can also be caused by SDGIs that reduce its residence time in the atmosphere (e.g., Carazzo & Jellinek, 2012; Durant, 2015). SDGIs occur when settling of volcanic ash at the boundary between volcanic clouds and surrounding atmosphere creates an interfacial region of excess density, called a particle-boundary layer, which, after reaching a critical thickness, becomes unstable, detaches, and protrudes downward creating a preferential transport path for volcanic ash (Fries et al., 2021; Manzella et al., 2015; Scollo et al., 2017) (Figure 7). Settling-driven gravitational instabilities significantly enhance sedimentation rates of volcanic ash and lead to locally increased ash concentration within fingers, potentially increasing aggregation efficiency (Carazzo & Jellinek, 2012, 2013; Lemus et al., 2021). Dedicated analytical and numerical models have been developed to explore the impact of particle aggregation on tephra sedimentation. These models are either based on adjusting the input grain size distribution (Bonadonna et al., 2002; Cornell et al., 1983; Mastin et al., 2013, 2016) or on the population balance theory (F. Beckett et al., 2022; Costa et al., 2010; de' Michieli Vitturi & Pardini, 2021; Folch et al., 2020; Ramkrishna & Singh, 2014; Smoluchowski, 1917). However, SDGIs still require a detailed parameterization. Given the complexity of all size-selective sedimentation processes, tephra sedimentation is commonly described as sedimentation of individual particles, especially for real-time forecasting that requires fast simulations (Folch, 2012).

### 2.3.5. Resuspension

Under specific meteorological and environmental conditions (e.g., strong winds, low soil moisture, and lack of vegetation), tephra deposits can be remobilized by wind and be re-injected into the atmosphere (Del Bello et al., 2018; Douillet et al., 2014; Jarvis et al., 2020; Liu et al., 2014; Miwa et al., 2018). Once the threshold friction velocity is exceeded by the wind, ash particles start to be entrained into the atmosphere with the largest particles (from  $\sim 50\ \mu\text{m}$  to 1 cm in diameter) moving by creep (i.e., rolling/sliding) or saltation (following ballistic trajectories) and the finest material being transported in suspension (Folch et al., 2014; Jarvis et al., 2020; Kok et al., 2012). The frequency and intensity of ash-remobilization events depends on the availability and compaction

of volcanic deposits, their specific features (e.g., grain size, particle density, particle shape), atmospheric conditions (e.g., wind, rainfall), land surface state (e.g., soil moisture, vegetation), and topography (Dominguez, Rossi, et al., 2020; L. Mingari et al., 2020). In contrast to primary tephra fallout, ash-remobilization by wind does not have a single source of emission, can occur in both fresh and ancient deposits, and can affect both proximal and distal areas (L. A. Mingari et al., 2017; T. M. Wilson et al., 2011). Notably, remobilized ash is characterized by a lower melting temperature than mineral dust, thus increasing the potential impact on aviation (Butwin et al., 2020), and higher PM10 (i.e., particles smaller than 10  $\mu\text{m}$ ) content with respect to primary fallout due to particle abrasion and disaggregation of particle clusters, thus increasing impact on public health (e.g., Dominguez, Bonadonna, et al., 2020).

### 3. Monitoring Tephra Plumes and Clouds

#### 3.1. Monitoring From the Ground

In the event of explosive eruptions of various types, ground-based monitoring systems enable the measurement of key features describing the dynamics of the tephra plumes and clouds. These features include, among others, spatial extent of the plume and related cloud (e.g., column height, extent of umbrella cloud, altitude, and thickness of the ash cloud), aerodynamic properties of tephra particles (e.g., size, shape, settling velocity), MER, ground sedimentation rate and eruption duration. Timely collection of such information during eruptions is well-suited for hazard assessment and can be used in synergy with satellite measurements and numerical modeling to evaluate the potential consequences of explosive eruptions (Chazette et al., 2012; Devenish et al., 2012; Pyle et al., 2013).

To date, not all of the approximately 1,500 active volcanoes on Earth have a systematic ground-based monitoring system (Loughlin et al., 2015; Sparks et al., 2012). Recent estimates suggest that only a third to a half of these volcanoes are monitored from the ground, but even fewer are considered well-monitored (Pritchard et al., 2022). Reasons for this shortcoming include the fact that many volcanoes are situated in remote areas with limited access, whether due to geographical or political reasons. Additionally, eruptions are relatively rare events, making the installation and maintenance costs of dedicated monitoring systems not always affordable when considering the cost-to-benefit ratio. This is particularly true for volcanoes located in uninhabited areas (Biggs et al., 2021; McKee et al., 2021). However, systematic ground-based observations are conducted through permanent networks for certain active volcanoes located in densely populated areas (e.g., Mount Etna in Italy, Sakurajima in Japan) or in sites where explosive eruption can cause air travel disruption at continental scale (e.g., Iceland) (Dürig et al., 2018; Iguchi et al., 2019; Scollo et al., 2009).

Below, the main tools and techniques used to monitor volcanic plumes and clouds from the ground are described and a summary is provided in Table 1. Additionally, we include information on in situ sampling from piloted aircraft and balloons, techniques employed during some eruptions, such as the Eyjafjallajökull eruption (Iceland, 2010).

##### 3.1.1. Visible Cameras

Visible cameras are sensors that collect visible light (400–700 nm) and convert it into images or videos that replicate human vision. State Volcano Observatories (SVOs) (see Section 4.4) often manage networks of visible cameras that help monitor volcanic activity at specific sites (Barnie et al. (2023) and references therein). Visible cameras are cheap and easily deployable tools that are becoming widely used to detect and characterize volcanic plumes. A major advantage of these sensors is the possibility to monitor plumes produced by different eruption styles, from low-altitude ash-poor plumes (Pfeffer et al., 2018) to those reaching heights up to about 15 km (Scollo et al., 2019). However, visible cameras can only work during the day and in favorable weather conditions. They are therefore complementary to other techniques such as those based on infrared sensors that can operate also at night. In some cases, plume images are automatically calibrated (also considering the effect of the wind) and operators can use them to extract estimates of plume height, for example, to report in the VONAs (Barnie et al., 2023; Scollo et al., 2014) (Figure 8). From such estimates, MER can be retrieved (from empirical relations, analytical or numerical eruption models) and used to initialize tephra dispersal models. Recently, software applications that automatically process high-resolution videos and images of plumes taken in the visible wavelength have emerged, although they are not yet used operationally (Aravena et al., 2023; Simionato et al., 2022; Valade et al., 2014). With these new systems, it is possible to automatically discriminate tephra plumes from the

**Table 1**

*Overview of the Different Techniques Used to Monitor Volcanic Plumes (Near Source) and Distal Volcanic Clouds From the Ground*

	Observed features	Spatial coverage	Particle range	Main pros. and cons.
Visible camera	PL	In situ- 10 s km		Estimation of plume height in real time, limited to daylight hours
Infrared camera	PL, PA	In situ	Fine ash	Useful for early warning
Radar	PL, PA	In situ- 100 s km	Coarse ash-lapilli	Works in real time under various conditions and distances from the vent but not sensitive to fine ash
Lidar	CL, PA	In situ- 1,000 s km	Fine ash	Monitors volcanic clouds in real time across various distances from the vent, influenced by atmospheric conditions
Infrasound microphone	PL	In situ- 1,000 s km		Useful for early warning of large eruptions at unmonitored volcanoes, signals may be attenuated by complex terrain
Disdrometer	PA	In situ	Coarse ash-lapilli	Low-cost, easily maintainable devices
Lightning antenna	PL, CL	In situ- 1,000 s km		Early warning system working round the clock
Petrological monitoring	PA	In situ	Coarse ash-lapilli	Accessing active volcanoes is challenging, needing prepared personnel, equipment, and infrastructure for timely sample analysis
Sampling from aircraft and balloons	PA, PL, CL	In situ- 1,000 s km	Fine ash	Good estimates of ash concentration and particle size distribution. Aircraft flights are expensive and can be risky

*Note.* *PL* indicates observations of the plume, such as height, shape, ascent velocity, and extension of the umbrella cloud. *CL* indicates observations of the volcanic cloud, including height and thickness. *PA* indicates observations of particle sizes, atmospheric concentration, fall rate, and additional features, such as particle shape and composition. *Fine ash* refers to particles with diameter less than 63  $\mu\text{m}$ , *coarse ash* to particles from 63  $\mu\text{m}$  to 2 mm, and *lapilli* to particles from 2 to 64 mm.

background and retrieve the main geometrical parameters, such as plume height and shape, as well as characterize plume motion in terms of ascent velocity and acceleration.

### 3.1.2. Thermal Infrared Cameras

Thermal infrared cameras (or IR cameras) are devices that create images from the infrared radiation (3–14  $\mu\text{m}$ ) emitted from the scene being observed. Different types of IR cameras can be used for volcano monitoring. If well positioned near the volcanic source, broadband FLIR-type cameras can detect volcanic plumes due to the temperature contrast between the hot plume and the background atmosphere (Spampinato et al., 2011). The routine use of this type of cameras is widespread for surveillance purposes, and these devices are utilized by numerous SVOs (e.g., Barsotti et al., 2023; Scollo et al., 2019). As an example, the Istituto Nazionale di Geofisica e Vulcanologia-Osservatorio Etneo (INGV-OE) manages a network of five fixed FLIR-type cameras situated on the flanks of Mount Etna. These cameras continuously acquire data, enabling the timely detection of volcanic activity, including explosions that result in the formation of tephra plumes (Corradino et al., 2020) (Figure 9). Recently, Bombrun et al. (2018) and Wood et al. (2019) proposed segmentation methods to automatically detect, track and characterize volcanic plumes from data acquired by broadband IR cameras.

Post-processing algorithms applied to measurements collected by multi-spectral IR cameras (i.e., cameras with several spectral channels) can provide quantitative information of volcanic plumes, such as height, shape, ascent velocity, particle size, and total mass of atmospheric fine ash (e.g., Cerminara et al., 2015; Ripepe et al., 2013). A. J. Prata and Bernardo (2009) first applied multi-spectral-IR sensors to detect and quantify volcanic plumes. Working in the IR region between 7 and 14  $\mu\text{m}$ , the authors showed that it is possible to discriminate ash particles among different atmospheric components. Moreover, they demonstrated that by inverting the IR measurements through a microphysical ash model, effective radius (mainly fine ash 1–10  $\mu\text{m}$ ), optical depth, and mass of atmospheric ash can be retrieved. One of the main advantages of this technique is the possibility to operate also at night, but a serious limitation is that ash detection is possible only if the cameras are positioned a few kilometers from the volcanic source (F. Prata, 2020). The theory behind IR discrimination of volcanic ash from ground-based measurements was described by A. J. Prata and Barton (1994). Later in the text (Section 3.2.1), IR discrimination of volcanic ash from satellite measurements will be described in detail. Finally, we notice that quantitative applications of IR cameras mainly concern small and mild ash-rich eruptions such as those that frequently occur at

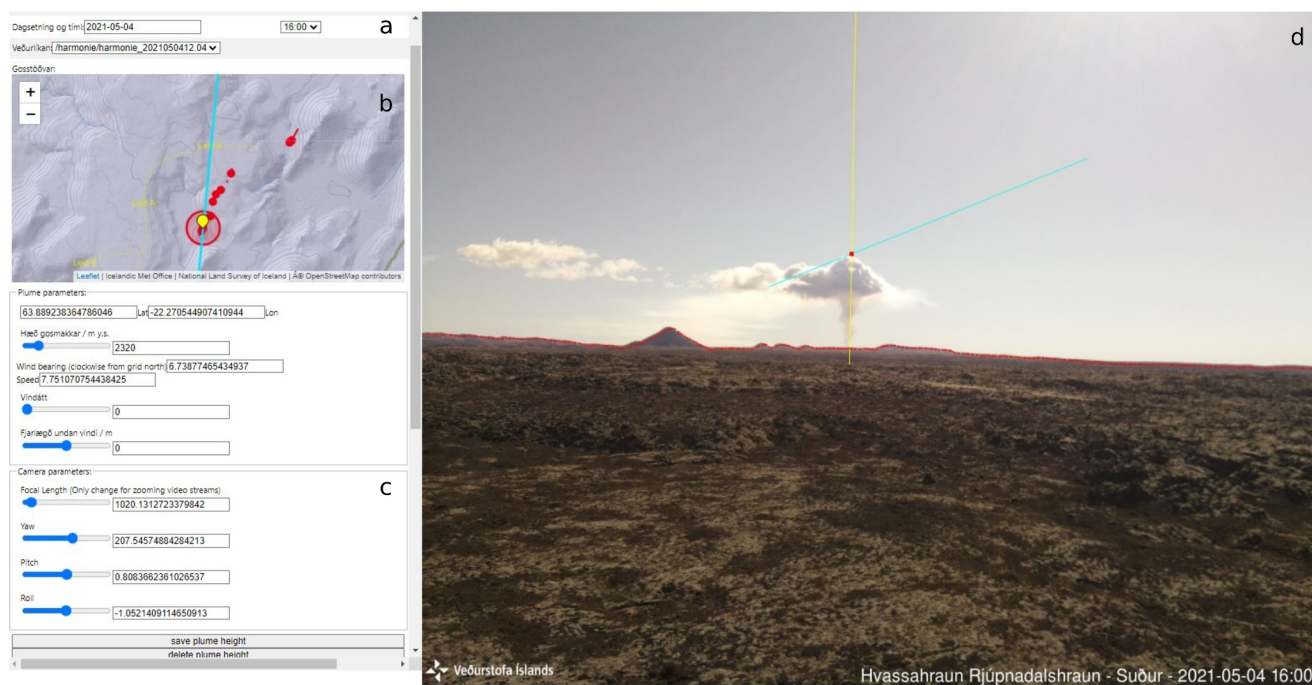


**Figure 8.** Screenshot of the web interface developed and managed by the IMO for real-time measurement of volcanic plume height. Visible images are acquired by webcams dispersed across Iceland to monitor volcanic activity. Through the web interface, an operator can produce real-time estimates of plume height from calibrated images. (a) Panel for selecting the camera, date, and wind profile. (b) Panel for selecting plume properties such as vent location and, if necessary, wind orientation. (c) Panel for updating camera orientation parameters. (d) Webcam image with the horizon plotted in red, the vertical above the vent location in yellow, and the horizontal plume height level in cyan. More information and a complete description of the tool can be found in [Barnie et al. \(2023\)](#).

Stromboli (Italy), Karymsky (Russia), and Santiaguito (Guatemala) volcanoes ([Harris et al., 2012](#); [Lopez et al., 2013, 2015](#); [Patrick et al., 2007](#); [Sahetapy-Engel & Harris, 2009](#)).

### 3.1.3. Weather Radars

Weather radars are systems traditionally dedicated to the study of hydrometeors and rain clouds. Radars send out pulses of microwave radiation that, due to the interaction with water droplets or ice particles, can be reflected back to the radar allowing the characterization of the target of interest (e.g., type and location of the precipitation). Weather radars operating at S band (approximately 10 cm wavelength), C band (approximately 6 cm wavelength), and X band (approximately 3 cm wavelength) can be used for volcano monitoring (a review on the use of radars for volcanological applications can be found in [Marzano et al. \(2013a\)](#)). These instruments have been successfully used to monitor volcanic eruptions since the 1970s ([Kienle & Shaw, 1979](#)). Over the years, many major eruptions have been monitored through radars, including Mount St. Helens (USA, 1980), Pinatubo (Philippines, 1991), and Eyjafjallajökull (Iceland, 2010, [Figure 10](#)) (a complete list up to 2013 and references can be found in [Mackie et al. \(2016\)](#)).

Through data supplied by radar systems, it is possible not only to detect volcanic plumes, but also to retrieve quantitative information of microphysical properties of tephra particles, geometrical characteristics of the plume, and MER ([Donnadieu, 2012](#); [Donnadieu et al., 2016](#); [Freret-Lorgeril et al., 2018](#); [Marzano et al., 2013a](#)). For example, the vertical profiles of radar reflectivity ( $ZH$ ) shown in [Figure 11](#) reveal that the average dimensions of the 2010 Eyjafjallajökull eruption plume were 10 km horizontally and 6 km vertically ([Mereu et al., 2015](#)).

Nowadays, the Volcanic Ash Radar Retrieval (VARR) procedure developed by [Marzano et al. \(2006\)](#) is one of the most applied techniques to process radar data for volcano monitoring. The VARR allows for the estimation of quantitative information of volcanic plumes and clouds from radar measurements. Briefly, the VARR is based on the construction of a forward microphysical model that relates the radar signal to the properties of the tephra particles. In the default configuration, tephra concentration and fall rate are calculated by applying a Bayesian

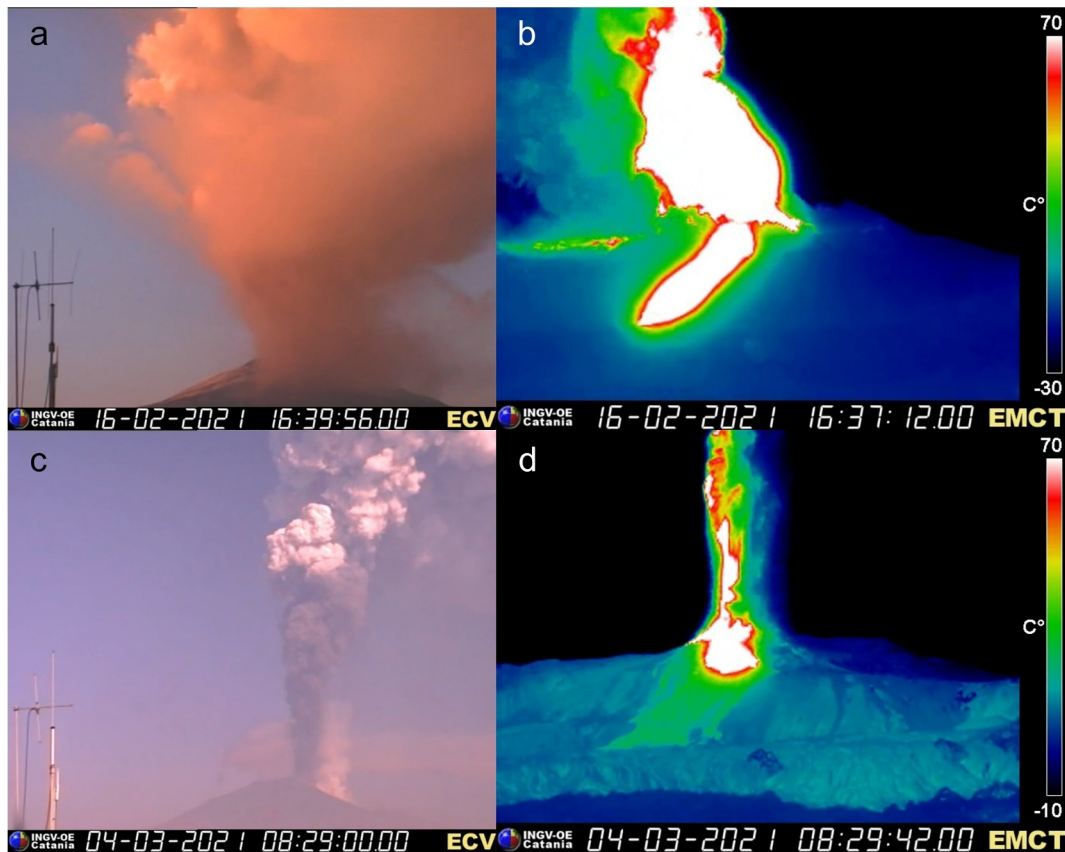


**Figure 9.** Visible and thermal images of Mount Etna plumes acquired by the monitoring network of INGV-OE. (a, c) Display visible images captured by the camera located 27 km south of the Southeast Crater of Mount Etna. (b, d) Present thermal images of the same plumes, taken by the Monte Cagliato thermal camera positioned 8 km east of the Southeast Crater. Courtesy of INGV-OE.

inversion to the radar reflectivity measurements. Further extensions enable the VARR to estimate mean particle diameter and airborne tephra particle size distribution and to extrapolate MER and amount of tephra deposited on the ground (Mereu et al., 2015).

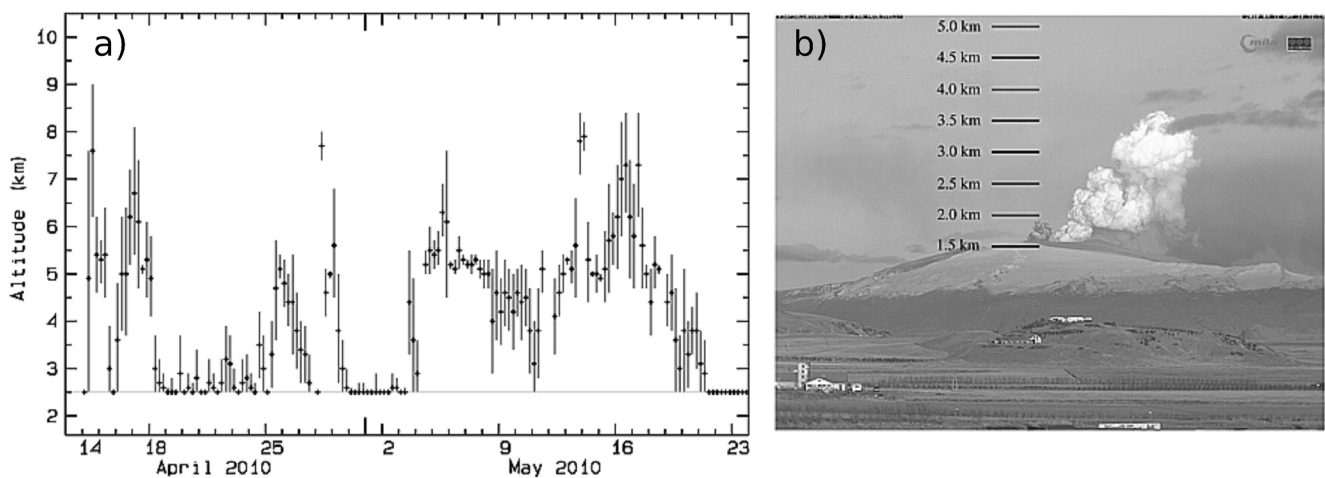


**Figure 10.** (a) Shows the 6-hr average altitude of the Eyjafjallajökull 2010 plume top as observed by the weather radar located at Keflavik International Airport. The bars indicate one standard deviation. (b) Shows an example of a visible image of the plume taken at 20:12:14 UTC on 17 April 2010 from the camera located at Hvolsvöllur. Figures from Petersen et al. (2012).

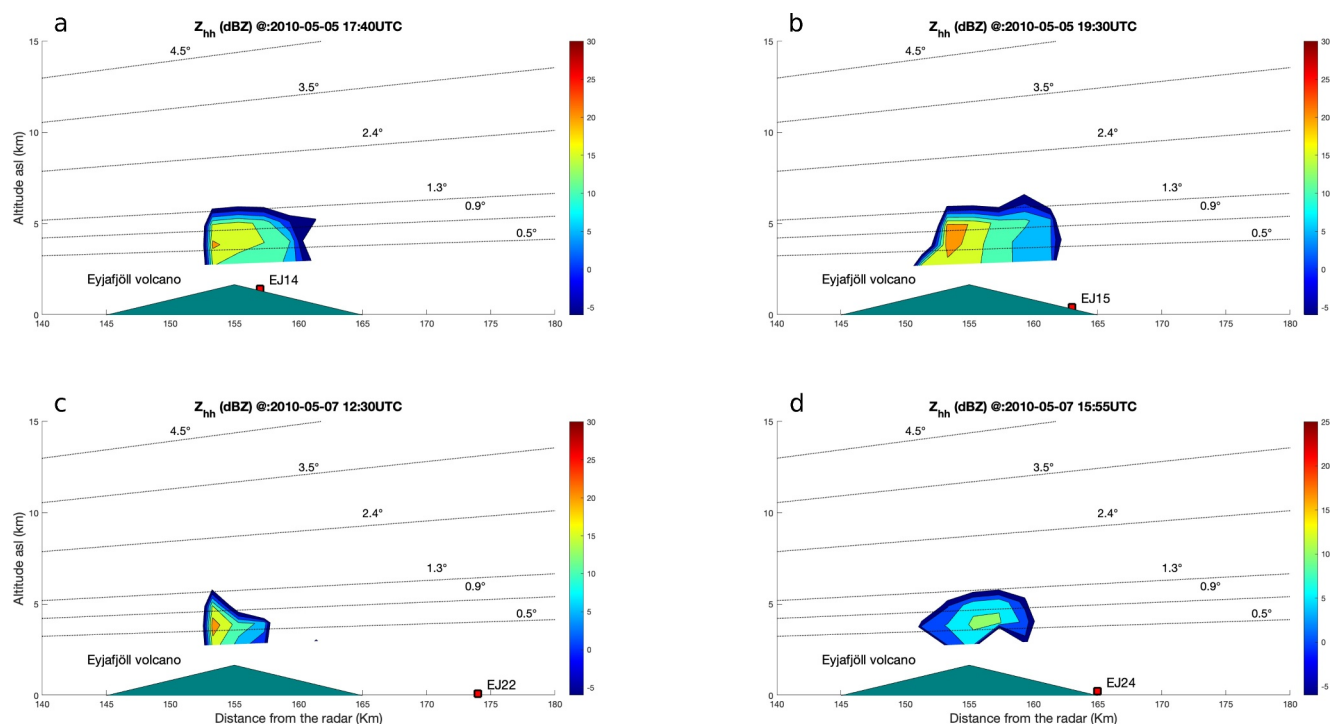


**Figure 11.** Vertical profiles of radar reflectivity ( $Z_{hh}$ ) during four instants of the volcanic activity of Eyjafjallajökull (Iceland) in May 2010. (a) Refers to 17:40 UTC on 5 May 2010, (b) 19:30 UTC on 5 May 2010, (c) 12:30 UTC on 7 May 2010, and (d) 15:55 UTC on 7 May 2010. The position of the radar sampling sites (EJn) is reported in each panel, while the lines of varying degrees indicate the angles of the radar. Figure courtesy Luigi Mereu.

The ability to work around the clock, in any weather conditions and with high temporal resolutions are the main advantages of radar measurements. Furthermore, these systems do not need to be located close to the volcanic source, but, depending on the instrument, distances up to some hundreds of kilometers are possible (Marzano et al., 2013a). Thus, radars are robust tools that can detect and characterize volcanic plumes produced by different eruption styles, from Plinian and sub-Plinian eruptions (Harris & Rose, 1983; Marzano, Lamantea, et al., 2013; Oswalt et al., 1996; Schneider & Hoblitt, 2013; Vidal et al., 2017) to less energetic events (Arason et al., 2013; Donnadieu et al., 2011; Iguchi et al., 2019). One of the major limitations in the implementation of radar systems comes from the fact that radars, due to their centimeter wavelengths, are mainly sensitive to coarse ash and lapilli, and are unable to detect the finest particles ( $<63 \mu\text{m}$ ). Therefore, depending on the style of the eruption and the properties of the erupted particles, the height of the column may not be detectable (or detected with high uncertainty and likely underestimated) if the top of the column consists of the finest particles (Rose et al., 1995b). Finally, due to their limited sensitivity, volcanic clouds with low ash concentrations are challenging to detect with radars.

### 3.1.4. Ground-Based Lidar

Ground-based lidar is a remote sensing technique that sends pulses of laser light into the atmosphere and collects the radiation backscattered by the atmospheric components interacting with the laser signal. The received radiation is proportional to the presence, range, concentration, and nature of the atmospheric components, such as water vapor, but also volcanic particles. While radars are sensitive to the coarse fraction of tephra, lidars are optimized to detect the finest particles dispersed in the troposphere and lower stratosphere and therefore are particularly suitable for long-range tracking of volcanic clouds (Bedoya-Velásquez et al., 2022; Boselli et al., 2018; Gasteiger et al., 2011; Jing et al., 2023; Mereu et al., 2018, 2021; Mortier et al., 2013).

Through lidar measurements it is possible to estimate not only the height and thickness of the clouds, but also the size and concentration of the particles; while limitations arise in detecting plumes at source, especially for large eruptions that produce optically thick plumes. Permanent lidar instruments are currently deployed at some well monitored volcanoes, such as Sakurajima (Japan, Iguchi et al., 2019) and Mount Etna (Italy, Scollo et al., 2020),

for the real-time monitoring of ash clouds. Non-volcano lidar networks, however, are able to detect and discriminate ash clouds if the clouds intersect their field of view. Examples include the networks EARLINET (European Aerosol Research Lidar Network) in Europe, that detected the ash cloud produced by the Eyjafjallajökull eruption (Iceland, 2010) thousands of kilometers away (Ansmann et al., 2010), and NASA MPLNET (Micropulse Lidar Network), which is instead deployed on global scale.

### 3.1.5. Infrasound Microphones

An infrasound microphone is a device that detects acoustic waves below the human audibility limit (<20 Hz). Infrasound is emitted by numerous natural phenomena, including severe weather, seismic events, and volcanic eruptions (Bai et al., 2023; Vergoz et al., 2022). In particular, explosive eruptions generate infrasound waves that can travel through the atmosphere reaching distances of hundreds to thousands of kilometers from the volcanic source (Matoza et al., 2018). The powerful eruption of the Hunga volcano in 2022 produced strong atmospheric vibrations that circumnavigated the Earth and were recorded globally by the International Monitoring System infrasound network (Campus, 2006; Vergoz et al., 2022). Infrasound equipment has also been deployed locally at several volcanoes to monitor their activity (e.g., Castaño et al., 2020; Marchetti et al., 2019; Matoza et al., 2007). One of the main advantages of infrasound monitoring is the ability to acquire signals continuously at local, regional, and global scales. Thus, infrasound monitoring is an excellent method for detecting and localizing large eruptions of poorly monitored or unmonitored volcanoes, as well as detecting lower-intensity events that might otherwise go unnoticed (De Angelis et al., 2012). Beyond this application, infrasound can provide insights into eruption dynamics and source mechanisms, with different types of volcanic activity (from Hawaiian to Plinian), showing different acoustic characteristics (De Angelis et al., 2019; Fee & Matoza, 2013). Of particular interest for volcano monitoring is the positive correlation between acoustic power and plume height that emerges for large eruptions (Fee et al., 2010). Furthermore, several studies show that quantitative estimates of plume height and MER can be derived from infrasound data (Caplan-Auerbach et al., 2010; K. Kim et al., 2015; Lamb et al., 2015; Ripepe et al., 2013). This application is not yet operational in real-time and requires additional research, but it demonstrates the great potential of infrasound monitoring.

### 3.1.6. Disdrometers

Disdrometers are optical or radar devices originally designed to measure properties of precipitating hydrometeors such as raindrops, snowflakes, and hail. Near volcanic vents, disdrometers can also be used to detect volcanic particles and characterize their aerodynamic properties such as size, shape, and falling velocity. Optical disdrometers measure size and falling velocity of the particles passing through a laser beam (e.g., OTT Parsivel2 (Kozono et al., 2019), Thies Clima Laser Precipitation Monitor (Freret-Lorgeril, Bonadonna, Rossi, et al., 2022), and ASHER (Marchetti et al., 2022)). The portion of the laser beam obscured by the particles and the corresponding reduction of output voltage are proportional to the size of the particles, while the duration of the reduction gives estimates of falling velocity (Löffler-Mang & Joss, 2000). Additionally, 2D Video Disdrometers (2DVD) can also measure particle shape (Suh et al., 2019). Radar disdrometers measure particle size and falling velocity by analyzing the signal backscattered by volcanic particles. Thus, inversion algorithms must be developed to derive particle number and properties from the radar signal (Bonadonna et al., 2011; Scollo et al., 2005). Disdrometers are relatively low-cost devices which can be installed and maintained quite easily around active volcanoes. The first real-time measurement of ash settling velocity was conducted at Mount Etna during the 2002–2003 activity using a radar disdrometer (Scollo et al., 2005). Particles between 0.2 and 1 mm were efficiently detected and the settling velocities that were measured (between 0.47 and 1.09 m/s) were in good agreement with those derived from analytical models and experimental data. At Sakurajima volcano, a permanent network of 13 optical disdrometers can detect volcanic particles ranging from 0.2 to 25 mm in size, and from 0.2 to 20 m/s for the falling velocity (Iguchi et al., 2019; Maki et al., 2021). Optical disdrometers can also provide accurate information on tephra sedimentation rate (Freret-Lorgeril, Bonadonna, Rossi, et al., 2022).

### 3.1.7. Lightning Antennas

The main method for detecting lightning storms from the ground is to use antennas that receive lightning signals in different frequency bands. Very low frequency (VLF, 3–30 kHz) and very high frequency (VHF, 30–300 MHz) antennas deployed for weather forecasts are also used for volcano monitoring (Cimarelli and Genareau (2022) and references therein). Indeed, it is well known that explosive eruptions of different sizes can produce lightning

generated by the separation of charge in the eruption column (Aizawa et al., 2016; Behnke et al., 2013, 2014; Cimarelli et al., 2016; McNutt & Williams, 2010). Recently, lightning detection is emerging as a routine technique for volcano monitoring at different scales, from regional to global. The World Wide Lightning Location Network and the Vaisala Global Lightning Data set (GLD360) detect lightning strokes in real-time on a global scale, and their data sets have been used to investigate the dynamics of eruptions such as the 2015 Calbuco eruption (Baissac et al., 2021; Van Eaton et al., 2016). While Very low frequency antennas can detect lightning at distances of up to 1000s of km during large explosive eruptions, VHF sensors can be deployed to study the physics of lightning generation and propagation near the vent (Cimarelli & Genareau, 2022). Prompt detection of volcano lightning can help to reveal the occurrence of an explosive eruption producing an ash rich plume and eventually an ash cloud posing a hazard for aviation (Coombs et al., 2018; Smith et al., 2018, 2021). Moreover, some studies have revealed that multiparametric observations of lightning can help to characterize the size of the eruption, as well as the characteristics of the plume (e.g., plume height and MER) and of the ash cloud (Behnke et al., 2013, 2014; A. T. Prata et al., 2020; Schultz et al., 2020; Van Eaton et al., 2016).

### 3.1.8. Petrological Monitoring

It is worth noting that petrological monitoring of erupted products (including tephra particles) may offer further insights into eruption dynamics in general and plume dynamics in particular (Cashman & Taggart, 1983; Liu et al., 2020; Pankhurst et al., 2022). If timely and efficient field investigations and laboratory analyzes are performed while the eruption is in progress, size distributions and components of the particles deposited on the ground (the airborne component is probably not detected) can be constrained in a few hours (Re et al., 2021), and the resulting information can be used together with data from different monitoring techniques and/or to initialize numerical models. Nowadays, syn-eruptive petrological investigations can potentially be conducted on multiple styles of eruption, from weak to more violent ones. However, there are still limitations regarding the effective possibility of carrying out this type of monitoring often due to the lack of in situ facilities or qualified personnel (Re et al., 2021).

### 3.1.9. In Situ Sampling From Piloted Aircraft and Balloons

In situ sampling of dilute ash clouds from piloted aircraft has been performed for the assessment of the presence, spatial extent, and maximum concentration of volcanic ash at some eruptions. Pioneering flights were conducted using research aircraft to sample the volcanic clouds produced by the 1990 eruption of Redoubt Volcano and the 1980–1981 eruptions of Mount St. Helens (Hobbs et al., 1982, 1991). More recently, the long-lasting and low-intensity eruption of Eyjafjallajökull (Iceland, 2010) was a perfect case study, with several campaigns conducted at different sites (e.g., Iceland, Switzerland, and Germany) and using different aircraft (e.g., the Falcon aircraft operated by the Deutsches Zentrum für Luft- und Raumfahrt (DLR) and the UK's BAe-146-301 Atmospheric Research Aircraft managed by the Facility for Airborne Atmospheric Measurements). The results of these campaigns are presented in Dacre et al. (2013); Johnson et al. (2012); Schumann et al. (2011); Turnbull et al. (2012); Weber et al. (2012). Also at Sakurajima volcano, frequent, low intensity ash emissions were observed from airplanes in 2013 (Eliasson, Yoshitani, et al., 2014). More case studies of observations of airborne ash from piloted aircraft can be found in Eliasson et al. (2016). Optical particle counters mounted on board of research aircraft and appropriately calibrated for ash particles permit a quick estimate of ash concentration and size distribution (with relative uncertainties). The inherent risk of flying within volcanic plumes and clouds significantly limits the applicability of this technique. However, data collected from measurement campaigns hold great value; for instance, they can be utilized to validate the results of transport and dispersion models. An illustrative example is the eruption of Grímsvötn (Iceland, 2011), where airborne measurements of ash concentrations enabled the continued operation of airports in Reykjavik and Keflavik. This occurred despite numerical forecasts predicting ash levels above the safety threshold for flying (Eliasson, Yasuda, et al., 2014).

Some properties of volcanic plumes and clouds can be measured in situ by balloons (both tethered and free-released) carrying appropriate instruments (e.g., optical particle counters, backscatter sounders, and particle collectors). Flights conducted inside the clouds provide estimates of the vertical extent and concentration of volcanic aerosols and allow for the sampling of volcanic species. Despite being limited in number, successful balloon campaigns have been conducted at Eyjafjallajökull (Iceland), Kilauea (Hawaii), and Turrialba (Costa Rica) volcanoes (Petäjä et al., 2012; Pieri et al., 2013; Vernier et al., 2020). Recently, in situ observations of the volcanic cloud produced by the Hunga eruption in 2022 were performed one week after the eruption using

balloons on La Réunion (Kloss et al., 2022). The cloud was sampled during three balloon flights from 19 to 25 km altitude, revealing the presence of very small optically absorbing particles (with a radius less than 0.5  $\mu\text{m}$ ) that were missed by satellite observations. In this sense, balloon observations appear to be complementary to satellite measurements, as they offer high-resolution measurements of volcanic aerosols (and also gasses) that are difficult to obtain with other techniques. Moreover, balloons represent a relatively low-cost technique that can be quickly deployed during or after volcanic eruptions.

### 3.2. Monitoring From Space

Satellite observations offer a broad suite of techniques to monitor volcanic ash plumes and clouds. Both active and passive techniques ranging from ultraviolet (UV) to microwave (MV) wavelengths have been developed for the purpose of studying airborne ash. Monitoring volcanic ash from satellites includes detection, discrimination, and quantitative retrievals where physical information on the ash cloud (typically particle size, optical depth, and height) is obtained. Measurements made by current satellite instruments used for monitoring volcanic ash do not just vary in wavelength but also in the measurement principle (e.g., active vs. passive sensing, nadir vs. limb viewing), instrument design (e.g., sounders, radiometers, spectrometers) and satellite orbit (e.g., polar-orbiting, geostationary, Lagrange points). As with most remote sensing problems, combining differing sensor capabilities (i.e., sensor synergy) often provides the best solution as use of one satellite instrument over another will result in a tradeoff. In the context of ash monitoring, different satellite sensors will be suitable for monitoring both different eruption styles and different stages of an eruption sequence. Modern operational ash monitoring relies heavily upon geostationary measurements as they provide frequent imagery (1–10 min) suitable for continuous monitoring of volcanoes with the major trade-offs being coarse pixel size ( $\sim 4 \text{ km}^2$  at nadir), geometric constraints at high latitudes (geostationary satellites cannot view the poles as they must be positioned above the equator to maintain a stationary orbit), and, at present, multi-spectral measurements (as opposed to hyperspectral, which offer several advantages over multi-spectral; see Section 3.2.2). In addition, techniques that exploit passive thermal infrared measurements are favored due to the operational requirements of day and night observation whereas UV measurements are useful for monitoring passive degassing and precursory activity. Challenges associated with monitoring high latitude volcanoes with geostationary measurements can be ameliorated with the use of polar-orbiting satellites that have high repeat overpass times at high latitude. Though not the topic of the present review, monitoring of volcanic sulfur dioxide ( $\text{SO}_2$ ) has been demonstrated to be useful as a proxy for tracking volcanic ash clouds (Carn et al., 2009; Sears et al., 2013) but must be used with caution as volcanic ash and  $\text{SO}_2$  do not always travel together (Schneider et al., 1999; Constantine et al., 2000; F. Prata et al., 2017). This section summarizes the modern satellite-based techniques used for ash monitoring and highlights their applicability for monitoring different volcanic eruption styles and phases.

#### 3.2.1. Multi-Spectral Thermal Infrared Sensors

Ash cloud monitoring can be done based upon manual inspection of visible and infrared multi-spectral imagery and was first demonstrated by using the Visible-Infrared Spin Scan Radiometer aboard the Geostationary Meteorological Satellite in the 1980s (Sawada, 1983, 1987, 1996). However, ash discrimination with a single channel during the day is challenging due to cases where other atmospheric aerosols (e.g., desert dust, biomass burning plumes, industrial smoke pollution) may appear similar to ash clouds or cases where an ash cloud may appear like a meteorological cloud or be too transparent to be distinguishable from the underlying surface (see Figure 1 of A. J. Prata (2009) for examples). At night, ash discrimination using a single thermal infrared channel is perhaps more challenging due to the possibility of non-volcanic clouds and aerosols existing at similar optical depths and heights in the atmosphere to ash clouds. Ash discrimination using two (or more) multi-spectral infrared measurements (typically 11 and 12  $\mu\text{m}$ ) solves many of the aforementioned problems (A. J. Prata, 1989a, 1989b; A. J. Prata et al., 1991; Holasek & Rose, 1991; Schneider et al., 1999; I. M. Watson et al., 2004). A. J. Prata (1989a, 1989b) showed that semi-transparent ash clouds can be effectively discriminated from semi-transparent meteorological (water/ice) clouds due to the absorption peak of silica (the primary mineralogical component of ash particles) near 9.5–10  $\mu\text{m}$  (Soda, 1961; Pollack et al., 1973; Volz, 1973; Grainger et al., 2013; G. S. Prata et al., 2019). The  $\text{SiO}_2$  absorption peak near 9.5–10  $\mu\text{m}$  means that ash particles absorb more strongly near 11  $\mu\text{m}$  than 12  $\mu\text{m}$  whereas the opposite is true for semi-transparent ice/water clouds (Inoue, 1985; Prabhakara et al., 1988). When the 11 and 12  $\mu\text{m}$  radiances are converted to brightness temperatures ( $\text{BT}_{11}$  and  $\text{BT}_{12}$ ), a brightness temperature difference ( $\text{BTD} = \text{BT}_{11} - \text{BT}_{12}$ ) will be negative for a semi-

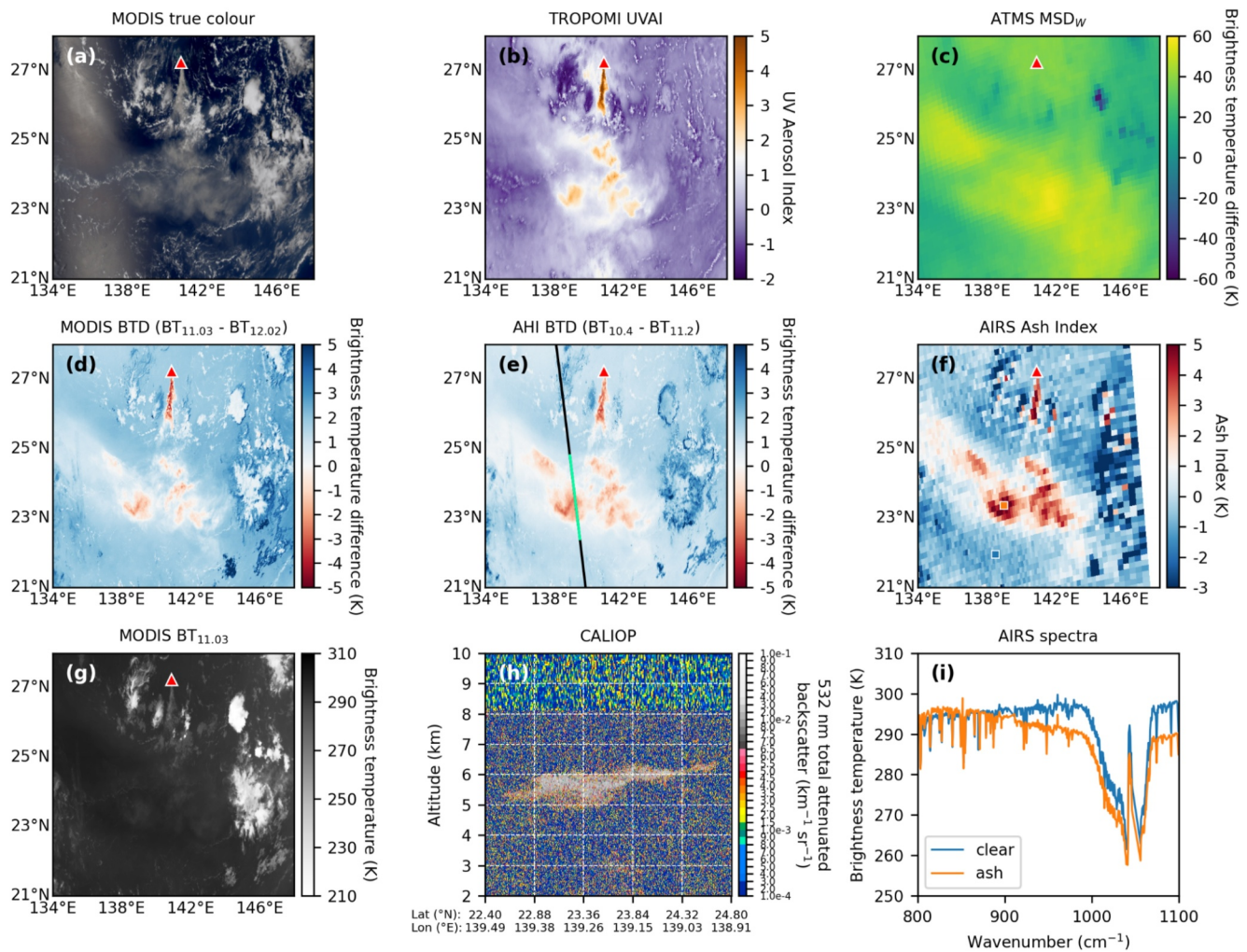


**Figure 12.** Multi-sensor ash detection of the 1 August 2020 Nishinoshima ash cloud. Nishinoshima volcano is indicated as a red triangle on panels (a)–(g). (a) MODIS-Aqua true-color composite image of two granules taken at nominal times of 04:05 and 04:10 UTC on 1 August 2020. (b) TROPOMI UV Aerosol Index (340–380 nm spectral contrast) for the granule from 03:13:45 to 04:12:08 UTC on 1 August 2020. (c) Advanced Technology Microwave Sounder window microwave spectral difference ( $MSD_w$ ) between the 165.50 GHz (channel 17) and 88.20 GHz (channel 16) from 03:36 to 03:42 UTC on 1 August 2020. (d) Same as (a) but for the brightness temperature difference (BTD) between 11 and 12  $\mu\text{m}$  channels. (e) AHI BTD between 10.4 and 11.2  $\mu\text{m}$  channels at a nominal time of 03:30 UTC on 1 August 2020 (note that the actual observation time will be offset from this by a few minutes). (f) AIRS Ash Index (see A. T. Prata et al. (2015) for details) from 04:05:31 to 04:11:30 UTC on 1 August 2020. (g) Same as (a) but for the brightness temperature at 11  $\mu\text{m}$ . (h) Cloud-Aerosol Lidar with Orthogonal Polarization total attenuated backscatter at 532 nm from 04:31:45 to 04:32:25 UTC on 1 August 2020. (i) AIRS spectral signatures for clear (blue) and ash contaminated (orange) pixels. The pixel locations for these spectra are indicated on (f) as blue (indicating clear) and orange (indicating ash) squares.

transparent ash cloud (Figure 12d), positive for a semi-transparent ice/water cloud and zero for an opaque cloud or clear surface (i.e.,  $BT_{11} \approx BT_{12}$ ); however, these inferences are only valid if it is assumed that the atmosphere is completely transmissive, the surface emissivity is 1 (at both wavelengths) and the channels are perfectly aligned and nadir-pointing. In practice, these assumptions are never fully satisfied leading to false positives or false negatives. False positives are considered to be cases where the BTD is negative but ash is not present whereas false negatives are considered to be cases where the BTD is zero or positive, but ash is present. All of the presently known false positives and negatives for the ash discrimination using the BTD method are given in Table 2. The BTD method works best when ash clouds are semi-transparent, there is a strong thermal contrast between the underlying land/sea surface (or cloud deck) and the temperature at the height of the ash clouds and when the particles are in the size range from 1 to 10  $\mu\text{m}$  (A. J. Prata & Grant, 2001; A. J. Prata & Prata, 2012; A. T. Prata, 2016; Wen & Rose, 1994). Thus, multi-spectral imagers are most suited to tracking ash clouds following the initial stages of an eruption (typically >30 min after eruption onset). Single-channel measurements from multi-spectral imagers can be used to identify a range of eruption style intensities based upon changes in

**Table 2**

*Known Cases Where False Positives (Brightness Temperature Difference [BTD] Is Negative But Ash Is Not Present) or Negatives (BTD Is Zero or Positive but Ash is Present) Can Occur If Using the BTD to Discriminate Ash Clouds in Passive Thermal Infrared Satellite Imagery*

Case	Description	Example references
<b>False positives</b>		
Channel misalignment, sensor calibration and noise	Negative BTDs have been observed due to the misalignment between multi-spectral channels (primarily near cloud edges). Additionally, cold cloud-top temperatures (<205 K) can result in negative BTDs due to sensor calibration biases. Modern day sensors are less prone to these effects due to improvements in sensor calibration and channel alignment	Potts and Ebert (1996) and Watkin (2003)
Surface emissivity	The difference between emissivity at 11 and 12 $\mu\text{m}$ can result in slightly negative BTDs over clear desert surfaces	Barton and Takashima (1986)
Surface inversions	Typically, over a clear land surface a positive BTD is expected due to the presence of water vapor. However, in the case of a low level temperature inversion (i.e., reversal of the thermal contrast) a slightly negative BTD can be observed	Platt and Prata (1993)
Cloud-top inversions	The inversion in temperature above cloud-tops (e.g., above convective storms and boundary layer stratus) can result in a negative BTD signal	Potts and Ebert (1996)
Desert dust	The high silica content of desert dust means negative BTDs are commonly observed for desert dust outbreaks	Gu et al. (2003)
Extreme view angles	At extreme view angles (e.g., observations of the Earth's limb from geostationary satellites) negative BTDs can be observed in the absence of ash, resulting in a false positive. In the presence of ash, due to the increased path length at extreme view angles, negative BTDs can be enhanced but this would not be regarded as a false positive	Gu et al. (2005) and A. T. Prata et al. (2021)
<b>False negatives</b>		
Water vapor	The BTD signal for ash clouds observed in humid atmospheres (e.g., the tropics) can be dampened or masked due to the positive BTD effect for water vapor. This can be resolved using an appropriate water vapor correction	Yu et al. (2002), Corradini et al. (2008), and Piscini et al. (2011)
Ice and liquid water interference	Ash particles that coexist in a volcanic cloud with ice particles and liquid water droplets can result in an overall positive BTD where the absorption properties of ice and water dominate. In addition, ash particles nucleated by ice can result in strongly positive BTDs	Rose, Delene, et al. (1995), Durant et al. (2008), F. Prata and Lynch (2019), and A. T. Prata et al. (2020)
Low thermal contrast	Ash clouds can be difficult to discriminate using a BTD if the thermal contrast between the surface and cloud-top is approximately equal. This can occur for high latitude volcanic ash clouds over land in the Kuril and Alaskan island chains	A. J. Prata and Grant (2001)
Low optical depth	Ash clouds may not return a negative BTD if their optical depth is below the detection sensitivity of the sensor being used	A. T. Prata et al. (2022)
High optical depth	Opaque ash clouds will return a BTD near zero as highly opaque clouds will act as gray bodies resulting in near equal values for the 11 and 12 $\mu\text{m}$ brightness temperatures. This commonly occurs at the beginning of a volcanic eruption	Schneider et al. (1995), Watkin (2003), F. Prata and Lynch (2019), and A. T. Prata et al. (2022)
Particle size	Radiative transfer theory shows that ash effective radii greater than $\sim 10 \mu\text{m}$ will return a BTD near zero or even a slightly positive BTD. Thus it is important to appreciate that thermal infrared measurements are sensitive to a subset of the overall size distribution of ash clouds	A. T. Prata et al. (2022)

brightness temperature in time (i.e., their vertical growth rate; Pavolonis et al., 2018); however, quantitative, microphysical information cannot be retrieved for ash plumes using thermal infrared measurements if they are opaque at these wavelengths. Whilst the BTD technique is still widely used by operational centers and the remote sensing research community, more sophisticated techniques such as water vapor-corrected BTDs (Yu et al., 2002), multi-channel techniques (Guéhenneux et al., 2015; Pavolonis et al., 2006),  $\beta$ -ratios (Pavolonis, 2010; Pavolonis et al., 2013, 2015a, 2015b), principal component analysis (Dean et al., 1994; Ellrod et al., 2003; Hillger & Clark, 2002a, 2002b; F. Prata & Lynch, 2019), robust statistical techniques (Marchese

et al., 2019; Pergola et al., 2004; Piscini et al., 2011), optimal estimation (A. T. Prata et al., 2022; Thomas & Siddans, 2015), and artificial neural networks (Gray & Bennartz, 2015; Petracca et al., 2022; Piscini et al., 2014) have been developed to improve upon a simple BTM. Thermal infrared retrieval algorithms are generally used to estimate the ash particle effective radius and the ash cloud optical depth (Corradini et al., 2008; A. J. Prata & Grant, 2001; F. Prata & Lynch, 2019; Wen & Rose, 1994). From this information an estimate of the ash mass loading ( $\text{kg}/\text{m}^2$ ) within a pixel can be made. The ash mass loading can be converted to a concentration ( $\text{kg}/\text{m}^3$ ), if further assumptions or independent measurements are made to constrain the geometric vertical thickness of the ash cloud (A. J. Prata & Prata, 2012). Ash mass loadings and/or ash concentrations derived from infrared imager measurements have numerous applications in numerical modeling (Section 4). Examples include dispersion model validation (A. T. Prata et al., 2021, 2022), data assimilation (Fu et al., 2017; L. Mingari et al., 2022; Pardini et al., 2020), inversion modeling (Chai et al., 2017; Harvey et al., 2022), and data insertion (A. M. Crawford et al., 2016; A. T. Prata et al., 2021; Wilkins et al., 2015; Wilkins, Watson, et al., 2016; Wilkins, Western, et al., 2016). More recently, optimal estimation algorithms (Rodgers, 1976, 2000), that account for prior information and attempt to simultaneously retrieve cloud-top height in addition to ash particle effective radius and optical depth have been developed (Francis et al., 2012; Kylling et al., 2014; Pavolonis et al., 2013, 2015a, 2015b; A. T. Prata et al., 2022).

### 3.2.2. Hyperspectral Thermal Infrared Sensors

Algorithms for ash discrimination using hyperspectral infrared sounding measurements have been developed since the launch of the Atmospheric Infrared Sounder (AIRS, operational from 2002-present; Chahine et al., 2006), the Infrared Atmospheric Sounding Interferometer (IASI, operational from 2007-present; Clerbaux et al., 2009) and Cross-track Infrared Sounder (CrIS, operational from 2012-present; Han et al., 2013). The simplest (and fastest) algorithms exploit similar wavelengths to those used for multi-spectral imager BTMs (Figure 12f; Hoffmann et al., 2014; A. T. Prata et al., 2015); however, the advantage of hyperspectral measurements is the thousands of channels that are available across the thermal infrared window, which can be used to analyze unique spectral signatures (Figure 12i; Clarisse & Prata, 2016; Clarisse et al., 2013; Gangale et al., 2010; Klüser et al., 2013). Optimal estimation techniques have also been developed to retrieve effective radius, optical depth, and cloud-top height (Clarisse et al., 2010; Sears et al., 2013; Taylor et al., 2023; Ventress et al., 2016). Generally, the advantage of hyperspectral retrievals over multi-spectral imager retrievals is better sensitivity to composition (Clarisse et al., 2013; Ishimoto et al., 2016) and optical depth (Griessbach et al., 2014) but at the expense of lower spatial resolution pixels and less frequent observations when compared to sensors onboard geostationary platforms (Dubuisson et al., 2014). Limb-viewing hyperspectral sounders have also been used to study volcanic ash (Grainger et al., 2013; Griessbach et al., 2014). The Michelson Interferometer for Passive Atmospheric Sounding (MIPAS) sensor, operational from 2002 to 2012, is a hyperspectral sounding instrument that viewed the atmosphere through the Earth's limb. Griessbach et al. (2014) found that ash can be discriminated based on the same principles as nadir-viewing ash discrimination, but due to the longer path length, MIPAS is sensitive to smaller particles and lower optical depths.

### 3.2.3. Ultraviolet Sensors

Detection of volcanic ash by passive UV sensors has been developed alongside thermal infrared techniques. Initial studies exploring the use of Nimbus 7/Total Ozone Mapping Spectrometer (TOMS) for aerosol monitoring showed that biomass aerosols could be discriminated by taking a UV reflectance difference between the 340 and 380 nm channels (Hsu et al., 1996). Seftor et al. (1997) demonstrated that volcanic ash from the 1982 El Chichón (Mexico) eruption could be identified in TOMS measurements and based on the work of Herman et al. (1997), showed that ash could be discriminated using the TOMS 340- and 380-nm channel pair. The technique developed to discriminate volcanic ash (and other UV-absorbing aerosols) is based upon the determination of the UV Aerosol Index (UVAI). The UVAI cannot distinguish between ash and other UV-absorbing aerosols when both are present as it is sensitive to iron and/or carbon, which is common to aerosols such as ash, mineral dust and biomass burning smoke. The UVAI is calculated by taking the logarithm (base 10) of the ratio of the observed backscattered radiance to the simulated (using a radiative transfer model) backscattered radiance and then multiplying by a scaling factor (see Equation 3 of Carn and Krotkov (2016), for example). A wavelength pair of UV channels that fall within a region where ozone absorption is negligible (i.e., 340–380 nm) are required to calculate UVAI (Figure 12b). Retrieval algorithms have been developed to obtain

optical depth, ash mass loading and particle size from satellite measurements of backscattered UV radiation (N. A. Krotkov et al., 1999). However, as with thermal IR retrieval algorithms, assumptions regarding the particle shape, distribution, height, and composition must be made which leads to large uncertainties in the retrieved parameters (Carn & Krotkov, 2016; Krotkov et al., 1999). Ash monitoring with UV sensors offer advantages over thermal IR monitoring for ash plumes at the initial stages of a sub-Plinian eruption (e.g., Raikoke 2019) because they do not require plume transparency or thermal contrast (discussed in Section 3.2.1). They also perform well in humid environments (e.g., Ambae 2018). Currently operational (at the time of writing), polar-orbiting sensors that can be used to track ash clouds based upon the UVAI include Ozone Monitoring Instrument (OMI; Torres et al., 2007), Ozone Mapping and Profiler Suite (OMPS; N. Krotkov et al., 2014), and TROPOspheric Monitoring Instrument (TROPOMI; De Laat et al., 2020); however, hyperspectral capabilities of existing UV sensors (such as OMI, OMPS, TROPOMI) are yet to be fully explored for the purposes of ash cloud property retrievals (see Carn and Krotkov (2016) for a detailed discussion of this topic). More recently, geostationary UVAI measurements have become available with the launch of the GEMS (Geostationary Environment Monitoring Spectrometer; operational from 2020–present; J. Kim et al., 2020), which provides observations over East Asia, and the TEMPO (Tropospheric Emissions: Monitoring of Pollution; operational from 2024–present; Naeger et al., 2021) instrument, providing observations over North America.

### 3.2.4. Microwave Sensors

Microwave sensors are useful for monitoring ash plumes at the initial stages of an eruption (within 30 min) because they are sensitive to large ash particles (millimeter) and have been used to study sub-Plinian to Plinian style eruptions (Marzano, Lamantea, et al., 2013; Marzano et al., 2018; Montopoli et al., 2013). Initial investigations into the capability for passive microwave sensors to study volcanic clouds showed that the 19–85 GHz range could be used for the detection of millimeter-sized volcanic particles (Delene et al., 1996). A scattering index (originally developed for microwave land surface characterization) was shown to be effective at delineating the nascent ash cloud from the 19 August 1992 Crater Peak (Mount Spurr) eruption when a brightness temperature threshold was applied. However, Marzano, Lamantea, et al. (2013) showed that snow covered surfaces can cause ambiguities when trying to identify the ash signal for frequencies less than 90 GHz. This work led to the development of the Window Microwave Spectral Difference ( $MSD_W$ ), which exploits the difference between two microwave brightness temperatures in the range 155–165 GHz and 85–95 GHz, and the Absorption Microwave Spectral Difference ( $MSD_A$ ), which exploits the difference between two higher frequency bands near 183 and 165 GHz (Marzano, Lamantea, et al., 2013; Marzano et al., 2018). In general, the  $MSD_W$  can be used to distinguish clouds from the surface whereas the  $MSD_A$  can be used to discriminate between meteorological cloud and volcanic ash (Romeo et al., 2023). Figure 12c shows an example of the  $MSD_W$  computed using the Advanced Technology Microwave Sounder (ATMS) and, when used in synergy with thermal ash discrimination algorithms (Figures 12d–12f), indicates that the Nishinoshima ash cloud at this time is likely composed of micron-sized particles. In general, passive microwave measurements are complementary to thermal infrared BTDs as they are able to discriminate larger (millimeter) sized particles in plumes that are opaque at thermal infrared wavelengths. Ash retrieval algorithms based upon the  $MSD_A$  are now being developed to simultaneously retrieve optical depth and particle size in an analogous way to thermal infrared retrieval algorithms. Recent analysis using the  $MSD_A$  derived for ATMS has shown that passive microwave radiometer retrievals are sensitive to larger particle sizes (0.28–2 mm), which is complementary to thermal infrared retrievals (Romeo et al., 2023).

### 3.2.5. Space-Borne Lidar

Space-borne lidar detection of volcanic clouds was demonstrated at the very early stages of the Cloud-Aerosol Lidar and Infrared Pathfinder Satellite Observations (CALIPSO) mission's lifetime. The Cloud-Aerosol Lidar with Orthogonal Polarization (CALIOP)'s “first-light” image was recorded on 7 June 2006 and revealed a stratospheric aerosol layer produced by the 20 May 2006 eruption of Soufriere Hills (Montserrat) volcano (Carn et al., 2009). The major advantage of space-borne lidar measurements over passive sensors is that active remote sensing provides direct measurements of volcanic ash cloud height and geometric thickness (A. J. Prata & Prata, 2012; A. T. Prata et al., 2015; Winker et al., 2012). Since the launch of CALIPSO, several techniques to discriminate ash clouds in lidar backscatter returns have been developed. These include multi-sensor techniques where thermal infrared BTDs are collocated with lidar signals (Figure 12h; A. T. Prata et al., 2015, 2017; Vernier et al., 2013) and techniques which classify ash particles based upon lidar measurements and ancillary reanalysis

data (M. H. Kim et al., 2018; Tackett et al., 2023; Winker et al., 2012). The unique benefits of measurements made by CALIOP have been enhanced through the sensor synergy enabled by NASA's Afternoon-train (A-train; Stephens et al., 2002). The ability to confirm the aerosol type appearing CALIOP vertical profiles using MODIS (e.g., F. Prata et al., 2017), AIRS (e.g., Gangale et al., 2010) and the Imaging Infrared Radiometer (IIR, also onboard CALIPSO; e.g., Vernier et al., 2013) have proved to be particularly useful. An example of sensor synergy involving CALIPSO is shown in Figure 12.

Another volcanic ash property that can be determined using space-borne lidar, is the particulate extinction-to-backscatter ratio (or "lidar ratio"). The lidar ratio can be retrieved from CALIOP measurements of volcanic ash layers only under certain conditions (A. T. Prata et al., 2017). Additionally, after retrieving the lidar ratio, one can also determine the particulate depolarization (a measure of particle sphericity) and the particulate color ratio (a measure of particle size). As ash particles are non-spherical, the depolarization ratio can be used to discriminate ash from spherical particles such as liquid water droplets and sulfates (A. T. Prata et al., 2017; Vernier et al., 2013; Winker et al., 2012). In addition, ash particles in aged ash layers are typically smaller than cloud layers composed of ice particles, meaning that the color ratio can be used to distinguish between ice and ash (A. T. Prata et al., 2017; Vernier et al., 2013). The main properties to discriminate ash clouds in lidar returns, used by the latest CALIOP aerosol feature-typing algorithm (version 4.5), include the mid-layer temperature, feature-integrated attenuated backscatter at 532 nm, estimated particulate depolarization ratio at 532 nm, and the feature color ratio (Tackett et al., 2023).

## 4. Numerical Modeling and Forecasting Strategies

### 4.1. Plume Modeling

Plume models simulate the dynamics of volcanic plumes (see Section 2.2 for the description of their physics). There are two main categories of models: one-dimensional (1D) and three-dimensional (3D) models. The theory of 1D models is based on the seminal paper by Morton et al. (1956), which derives conservation equations of buoyant plumes (not necessarily volcanic plumes) from the Navier-Stokes equations (the fundamental equations in fluid dynamics) under simplified assumptions. Specifically, Morton's theory assumes self-similar profiles of plume properties in the crossflow direction, allowing for the simplification of the conservation equations, which can be solved relatively easily. Subsequent works by L. Wilson (1976), Sparks (1986), and Woods (1988) applied Morton's theory to volcanic plumes, relaxing some initial assumptions, and forming the basis of the most recent 1D models.

1D models operate under several assumptions, such as steady-state conditions, thermal and mechanical equilibrium between solid and gaseous phases, and turbulence treated indirectly through entrainment coefficients. Despite their simplifications, 1D models are widely applied and developed today because they combine fast computational times (execution times are on the order of seconds) with a good representation of many features of volcanic plumes. Continuous improvements have been made to include additional features in 1D models, such as the effects of external wind (present in almost all the models), particle fallout and re-entrainment (e.g., Bursik, 2001; Folch et al., 2016), effects of moisture entrainment and latent heat release during water phase transitions (e.g., Degruyter & Bonadonna, 2012; de' Michieli Vitturi & Pardini, 2021; Devenish, 2013, 2016; Folch et al., 2016; Mastin, 2007; Woodhouse et al., 2013), addition of external water at the vent (e.g., Mastin, 2007), particle aggregation inside the plume (e.g., de' Michieli Vitturi & Pardini, 2021; Folch et al., 2016), and modeling of the expansion of the umbrella cloud (e.g., de' Michieli Vitturi & Pardini, 2021). A detailed review of many recent 1D models can be found in Costa, Suzuki, et al. (2016).

Input parameters of 1D models consist of ESPs and include vent elevation, MER, exit velocity (or alternatively, radius at the base of the plume), exit temperature, and exit water fraction. It is also necessary to define the grain-size distribution of the solid material ejected during the eruption. This information is known as total grain size distribution (TGSD) and some examples can be found in Bonadonna and Houghton (2005), Bonadonna et al. (2015), Costa, Pioli, and Bonadonna (2016), and in the IVESPA database (Aubry et al., 2021). Particle density and shape are additional inputs of plume models. Both can vary according to particle type; if the particle vesicularity varies significantly, density may also vary with particle size (Bonadonna & Phillips, 2003). These inputs define the properties of the mixture erupted from the vent, which has undergone the full conduit processes (expansion and fragmentation). In addition to volcanological input, 1D models that account for the effect of the wind require atmospheric properties (wind speed, pressure, temperature, density, and humidity) as vertical

profiles at the considered vent. These data are usually derived from radiosonde, numerical weather prediction models, or analytical relationships of standard atmosphere. By solving the set of conservation equations, along with constitutive equations, 1D models provide information on plume properties at different heights along the column, such as the mass fraction of gases and particles, ascent velocity, temperature, density, and particle size distribution. Models that also simulate particle fallout from the column provide the mass fluxes of particles lost from the column at various heights.

We notice that some models can be initialized with the height of the eruption column instead of MER (e.g., de' Michieli Vitturi & Pardini, 2021; Devenish, 2013, 2016; Folch et al., 2016). In this case, an inversion is performed by the model to determine the value of MER that produces the desired column height. This type of initialization is of particular value because column height, unlike MER, is a parameter that can be directly measured during eruptions (e.g., from calibrated visible cameras and weather radars, see Section 3.1), enabling the use of 1D models in operational settings. An example of this application is the VESPA system operated by the IMO, where MER of eruptions is computed by initializing the eruption column model PLUME-MoM (de' Michieli Vitturi et al., 2015), using estimates of column height provided by radar measurements. The MER retrieved from the inversion is then used to initialize Tephra transport and dispersal models (TTDMs), enabling real-time forecasts of ash cloud dispersal (see Barnie et al. (2023) and references therein).

3D models solve the time-dependent multiphase Navier-Stokes equations for the conservation of mass, momentum, and energy of the plume mixture and ambient air. Turbulence entrainment is simulated explicitly by resolving the eddy structure of the plume. Different models vary in how they treat the mixture of gas and particles forming the plume (e.g., perfect coupling or decoupling between the different phases), the resolution of turbulence (e.g., Large Eddy Simulation approach), and microphysical processes (e.g., phase changes of water, precipitation, and latent heat exchange). Model inputs are the same as those for 1D models (ESPs and atmospheric conditions), but the results are not averaged across vertical sections of the plume, allowing for the visualization of the spatio-temporal evolution of plume properties. Y. J. Suzuki et al. (2016) provide an intercomparison study of four 3D plume models and show that, despite some intrinsic differences, there is good consistency in terms of maximum plume height, neutral buoyancy, and umbrella spreading. High-Performance Computing is necessary to run these models, and execution times are at least on the order of hours. Thus, 3D models are mainly used for research, while their application for operational purposes is currently prohibitive.

#### 4.2. Models Used to Simulate Tephra Transport, Dispersal, and Sedimentation

The characterization of the mechanisms of the transport, dispersal, and sedimentation of tephra through the atmosphere is a major research topic in physical volcanology. Tephra transport and dispersal models are fundamental tools for constraining eruption parameters of past eruptions from the geological record, as well as for quantifying the hazard from airborne particles by merging various wind and emission scenarios in a probabilistic way. Following the seminal works of T. Suzuki (1983) and Armienti et al. (1988), volcanologists developed a first generation of tephra sedimentation models. These models were built upon simplifications that allowed for analytical (Gaussian) solutions of the Eulerian advection-diffusion-sedimentation equation, such as the HAZ-MAP (Macedonio et al., 2005) and TEPHRA (Bonadonna, Connor, et al., 2005) models. This development enabled standard methodologies for long-term ground hazard mapping. However, given their underlying simplifications, Gaussian models simulate the resulting ground deposit but do not consider the transient dispersal of tephra particles in the atmosphere. This limitation motivated the development of a second generation of "volcanology-native" TTDMs based on numerical solutions. Examples include FALL3D, Ash3d, and VOL-CALPUFF, the latter derived from the CALPUFF air quality modeling system (see Table 3 for references). Following the establishment in the 1990s of the network of Volcanic Ash Advisory Centers (VAACs) operated by national weather forecasting organizations, several other models originally intended for atmospheric transport and dispersion of different substances (e.g., radionuclides, atmospheric aerosols, pollutants, etc.) were adapted to simulate long-range transport of volcanic clouds. Over the years, continuous improvements in these "atmospheric-native" models have been incorporated into their operational setups. Examples include:

- The UK Met Office's Numerical Atmospheric-dispersion Modeling Environment (NAME) model,
- The Air Resources Laboratory's Hybrid Single-Particle Lagrangian Integrated Trajectory (HYSPLIT) model of the U.S. National Oceanic and Atmospheric Administration,

**Table 3**  
*List of Models Classified by Community Origin and Modeling Framework (Gaussian, Eulerian, Lagrangian)*

Model origin	Frame	Model name	Reference	VAAC
Volcanology (first generation)	Gaussian	HAZMAP	Macedonio et al. (2005)	
		TEPHRA	Bonadonna, Connor, et al. (2005)	
Volcanology (second generation)	Eulerian	FALL3D <sup>a</sup>	Folch et al. (2020)	Buenos Aires
		Ash3d <sup>b</sup>	Schwaiger et al. (2012)	
Atmospheric sciences	Lagrangian	VOL-CALPUFF	Barsotti et al. (2008)	
	Semi-Lagrangian	MOCAGE-accident	Martet et al. (2009)	Toulouse
	Lagrangian	FLEXPART <sup>c</sup>	Pisso et al. (2019)	
		NAME	A. Jones et al. (2007)	London
		MLDP0	D'Amours et al. (2010)	Montreal
	JMA-ATM	Shimbori and Ishii (2021)	Tokyo	
	HYSPLIT <sup>d</sup>	Stein et al. (2015)	Darwin, Washington, Anchorage, Wellington	

<sup>a</sup>Available at: <https://gitlab.com/fall3d-suite/>. <sup>b</sup>Available at: <https://vsc-ash.wr.usgs.gov/ash3d-gui/#/>. <sup>c</sup>Available at: <https://git.nilu.no/flexpart/flexpart>. <sup>d</sup>Available at: <https://www.ready.noaa.gov/HYSPLIT.php>.

- The Japan Meteorological Agency (JMA) Atmospheric Transport Model (JMA-ATM), which actually unifies the former global (JMA-GATM) and regional (JMA-RATM) model configurations,
- The Canadian Meteorological Center Modèle Lagrangien de Dispersion de Particules d'ordre zéro (MLDP0),
- The “FLEXible PARTicle dispersion model” (FLEXPART) model of the Norwegian Climate and Environmental Research Institute (NILU),
- The Météo-France “Modèle de Chimie Atmosphérique à Grande Échelle” (MOCAGE), with particular model configuration called “accident,” that neglects chemistry and can model volcanic ash as a tracer with sedimentation and releases adapted to volcanic emissions.

Finally, other models constrained to research applications (not listed in Table 3) include the U.S. WRF-Chem community model (e.g., Hirtl et al., 2020; Stuefer et al., 2013), the System for Integrated modeling of Atmospheric coMposition (SILAM) of the Finnish Meteorological Institute (e.g., Kerminen et al., 2011), the ICON-ART model of the German Weather Service (e.g., Rieger et al., 2015), including a pre-operational emergency setup, or the ATLAS model (Reckziegel et al., 2019).

A key distinction between different modeling approaches is the frame of reference: Lagrangian and Eulerian. Tephra transport and dispersal models based on the Lagrangian approach track the position of particles transported by the atmospheric flow. Lagrangian “particles” do not grow or split and can be viewed as air parcels containing the mass of many real physical particles. In contrast, Eulerian TTDMs utilize a fixed frame of reference (grid), where the properties of the cloud and the deposit are computed as a function of time. These models solve the Eulerian representation of the conservation equations of continuum mechanics (conservation of mass) with the equations describing advective and diffusive fluxes. Different models differ in the underlying meteorological drivers, parameterizations of physical processes (e.g., diffusion, sedimentation, aggregation, wet/dry deposition, etc.), description of the emission term in terms of source strength and vertical distribution, numerical strategies, and other capabilities like computation of backward trajectories and source term inversion. A review of the state of the art of the most commonly used TTDMs up to 2012 can be found in Folch (2012), who provides detailed information on the physics, numerics, model initialization, and expected results for the models listed in Table 3. Since then, improvements in model physics, solving algorithms, and code performance have been implemented in many TTDMs, leading to the release of updated versions (see Table 3 for the latest references). Additionally, extensive research over the past decade has focused on consolidating and operationalizing new modeling strategies, such as ensemble modeling and data assimilation, to produce probabilistic results that properly address the many sources of uncertainty affecting the use of TTDMs (these topics will be discussed further in the following sections).

#### 4.2.1. Model Initialization: Meteorological Data

Depending on the simulation setting, different kinds of meteorological data are required to run TTDMs. For very local scale representations (order of 1 km), a vertical profile defined above the vent reporting the main atmospheric quantities (pressure, wind velocity, temperature, and humidity) can be used assuming horizontal homogeneity of the atmospheric state (same as for the plume modeling). However, if complex topography is present, the atmospheric flow variations can be important, so very high-resolution four-dimensional meteorological fields are necessary (Poulidis et al., 2018). Equally, for scales from regional to global (order of 100–1,000 s of km), four-dimensional atmospheric data sets are needed to describe the horizontal and vertical variations of atmospheric variables over time. These data sets (forecast or reanalysis) are produced by numerical weather prediction models and supply the main properties of the atmosphere (usually pressure, temperature, wind speed, and direction, precipitation, and humidity) at different atmospheric levels (pressure, hybrid, or model levels), as well as at different spatial and temporal resolutions. For historical eruptions, meteorological data from reanalysis can be used, such as NCEP-NCAR reanalysis (Kalnay et al., 2018), ECMWF-ERA40 and -ERA5 data sets (Hersbach et al., 2020; Uppala et al., 2005). Meteorological reanalysis data combine past observations with the results of numerical models, applying data assimilation techniques to provide a description of recent climate. For example, the NCEP-NCAR Reanalysis 1 data is provided on a  $2.5^\circ \times 2.5^\circ$  global grid horizontally, with a vertical range from 1,000 to 10 hPa, and covers the time span from 1948 to the present. It can supply data four times daily, as well as daily and monthly values. The ECMWF-ERA5 data also has global coverage but on a  $0.25^\circ \times 0.25^\circ$  horizontal grid and a vertical range from 1,000 to 1 hPa, covering the period from 1940 to the present with hourly data. Some applications of TTDMs using these data sets are shown in Fero et al. (2009) and Folch et al. (2012). Real-time forecasts of eruptions require data from numerical weather forecasting models such as the Global Forecasting System (GFS) from NCEP (NCEP, 2015) or the Integrated Forecasting System from ECMWF. For example, GFS data are global data containing 384 hr of forecast, supplied at different horizontal resolutions (e.g.,  $0.25^\circ \times 0.25^\circ$  or  $0.5^\circ \times 0.5^\circ$ ) and with a temporal resolution of 3 hr. Model forecast runs occur at 00, 06, 12, and 18 daily. To be used by the TTDMs, meteorological data sets require to be interpolated both in space and in time in order to fit the setting of the TTDM (spatial and temporal resolution). This approach, known as off-line approach, is followed by the majority of TTDMs currently employed and listed in Table 3.

On the contrary, the in-line approach involves coupling the numerical weather prediction model with the TTDM (e.g., Hirtl et al., 2019; Ngan et al., 2015; Stuefer et al., 2013). In this case, the evolution of the atmosphere is solved simultaneously with the transport of volcanic particles, eliminating the need to interpolate the meteorological data set to meet the requirements of the tephra transport simulation. This approach, which is receiving growing attention, enhances the accuracy of the simulation of tephra motion, but requires higher computational time compared to the traditional off-line approach and it is not currently used operationally, but only for research.

#### 4.2.2. Model Initialization: Eruption Source Parameters

Two possible mechanisms are responsible for injecting tephra particles into the atmosphere: direct injection from an eruption column and particle resuspension, that is, remobilization of particles already deposited on the ground by wind erosion (Folch et al., 2014; L. Mingari et al., 2020). While resuspension is receiving increasing attention, direct injection from eruption columns is, by far, the most commonly considered and modeled mechanism. In the case of direct injection, defining the source conditions involves describing *what*, *how much*, and *how* tephra particles are injected into the atmosphere, as well as specifying *how long* the emission lasts (date of start and end). Particle characterization (which answers *what*) requires defining TGSD, particle density, and shape, as in plume modeling. Generally, users can input their own TGSD and physical particle characteristics. Additionally, users may have the option to choose TGSD estimations, such as Gaussian, bi-Gaussian, Weibull distributions, or more complex schemes as proposed by Costa, Pioli, and Bonadonna (2016), where TGSD is inferred from magma viscosity. This latter capability has been included in the latest release of FALL3D (Folch et al., 2020).

The amount of material exiting the vent in a given amount of time (which answers *how much*) is denoted by the MER. While MER generally refers to the entire eruption mixture, comprising solid particles and gasses, only its solid fraction is relevant to tephra particles. In TTDMs, users normally have the option to input MER directly or adopt some parameterization scheme. These schemes compute MER either from column height (e.g., Mastin et al., 2009) or from a combination of column height and meteorological conditions, such as Aubry, Engwell et al. (2023), Degrueter and Bonadonna (2012), and Woodhouse et al. (2013). Additionally, results of integral 1D

plume models (e.g., de' Michieli Vitturi & Pardini, 2021; Devenish, 2013, 2016; Folch et al., 2016) or more complex 3D models can also be used to estimate MER (Cao et al., 2021; Y. J. Suzuki et al., 2016), providing a better description of eruption and meteorological conditions. To address the question of *how* tephra particles enter the atmosphere, different vertical distributions can be adopted to describe the altitude-dependent emission of particles into the atmosphere from an eruption column. Example distributions include punctual, uniform, umbrella-Suzuki, shown in Figure 13 (Pfeiffer et al., 2005), and those provided by 1D and 3D column models. An alternative approach is to initialize TTDMs from a virtual source coinciding with the ash cloud as supplied by the satellite retrievals (A. M. Crawford et al., 2016; A. T. Prata et al., 2021; Wilkins et al., 2015; Wilkins, Watson, et al., 2016; Wilkins, Western, et al., 2016). This technique, known as data insertion, requires certain assumptions about cloud height, thickness, and particle size. However, it avoids the need to describe the volcanic source, which is often highly uncertain. For this reason, data insertion is particularly suitable for remote volcanoes where observational constraints on eruption parameters are usually lacking due to the absence of a monitoring network. Optimal ESPs retrieved from inversion techniques using observations of volcanic clouds can also be used to initialize TTDMs. This topic will be discussed in more detail in Section 4.3.

Some TTDMs, such as FALL3D, Ash3d, NAME, and HYSPLIT, offer the possibility to inject particles into the atmosphere from resuspension mechanisms. Forecasting of ash resuspension episodes is required by the VAACs (ICAO, 2021; Jarvis et al., 2020) and is typically simulated based on various emission schemes originally derived for mineral dust (Folch et al., 2014; Leadbetter et al., 2012; L. A. Mingari et al., 2017; L. Mingari et al., 2020; Reckziegel et al., 2016). In case of particle resuspension, the emission rate is defined as the vertical flux of particles that are re-injected into the atmosphere due to the action of the wind (Folch et al., 2014). Some ash remobilization schemes parametrize the vertical emission flux as a function of friction velocity (i.e., a parameter that describes the turbulent transfer of momentum between the atmosphere and the ground surface) and particle diameter (Marticorena et al., 1997; Westphal et al., 1987). Other schemes relate the vertical flux to the saltation of larger particles that trigger the vertical emission of the smaller ones (Shao et al., 1993). In all the schemes, the emission occurs if friction velocity exceeds a threshold value which represents the resistance of the surface against wind erosion (L. Mingari et al., 2020).

It is important to note that model initialization can vary depending on the purpose of the simulation. To simulate the large-scale transport of ash particles, it may be sufficient to release only the fraction of MER composed of fine particles that do not deposit near the vent and remain suspended in the atmosphere. Gouhier et al. (2019) estimated that, depending on the type of eruption, ash particles transported over long distances represent between 0.1% and 6.9% of those emitted. From a modeling perspective, it is often assumed that only particles with a diameter smaller than 100  $\mu\text{m}$  and representing 5% of the total erupted mass are released into the atmosphere (F. M. Beckett et al., 2020). Moreover, the resolution of meteorological data can be coarser, as the focus is on simulating high-altitude transport where atmospheric characteristics are generally more stable. These assumptions are made to reduce the computational times of the simulations, which is an important requirement, especially for operational forecasting.

A different and more accurate initialization is necessary when simulating proximal dispersion and sedimentation. In this case, it is important to have an accurate estimate of MER (or plume height), TGSD, and particle properties. The meteorological data also needs greater accuracy and higher spatial and temporal resolution, possibly including a correct representation of the topography around the vent. These precautions are necessary to obtain an accurate estimate of the deposition rate and the distance reached from the vent (e.g., Andronico et al., 2024).

#### 4.2.3. Simulated Processes and Numerical Results

Once in the atmosphere, TTDMs simulate the transport of tephra particles by the wind (advection) and the turbulent motion produced by smaller-scale unresolved eddies (diffusion). While advection moves the tephra cloud according to the main wind components, diffusion spreads the cloud horizontally and vertically. Lagrangian models parametrize atmospheric diffusion by adding stochastic fluctuations in velocity components with random walk processes (F. M. Beckett et al., 2020; D'Amours et al., 2015). Eulerian models use the eddy diffusivity tensor, which parameterizes subgrid-scale transport of energy and momentum (Jacobson, 1999).

The third process simulated by TTDMs is the removal of tephra particles from the atmosphere by sedimentation and deposition on the ground. In the free atmosphere, sedimentation by gravity is the primary mechanism responsible for the settling of particles (see Section 2.3.1). TTDMs compute gravitational settling velocity

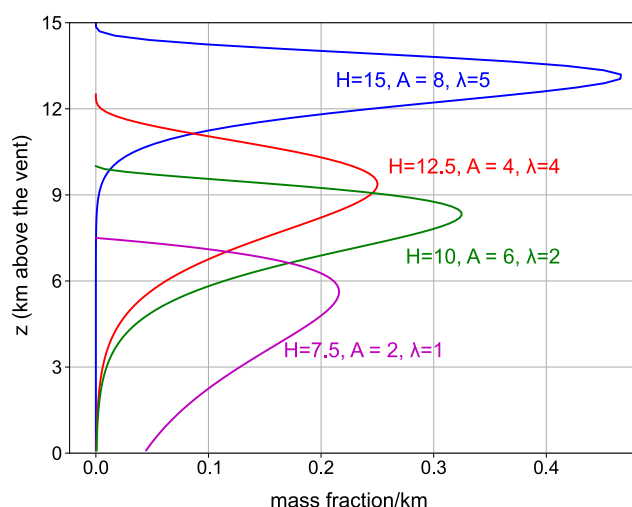


**Figure 13.** Example of vertical distributions that can be used to initialize Tephra transport and dispersal models. The Suzuki mass loss distribution is expressed by the formula:  $S(z) = \{1 - z/H \exp[A(z/H - 1)]\}^4$ , where  $S$  is the mass of material lost by the plume per unit height of the plume,  $z$  is the altitude of the plume,  $H$  the maximum plume height,  $A$  and  $\lambda$  two non-dimensional parameters. Different vertical profiles (i.e., different ways to release mass of tephra as a function of plume height) can be drawn by varying  $H$ ,  $A$ , and  $\lambda$ .

(assumed equal to terminal velocity) using particle diameter, density, and shape factor and apply different formulations for the calculation of the drag coefficient. For example, the latest version of FALL3D proposes three possible formulations for the drag coefficient: *ganser* (Ganser, 1993), *pfeiffer* (Pfeiffer et al., 2005), and *dioguardi* (Dioguardi et al., 2018). In dry conditions and near the surface, deposition of smaller particles ( $<100 \mu\text{m}$ ) also depends on the interaction between the particles and the atmospheric layers above the ground. In this case, the terminal velocity computed for the gravitational regime is corrected by including the contribution of additional terms that account for the resistance encountered by a particle suspended close to the ground (Feng, 2008). As stated in Section 2.3.2, wet deposition represents the removal via in-cloud and below-cloud scavenging. Typically, wet deposition is modeled by defining a scavenging coefficient, which depends on the precipitation rate, the type of precipitation (rain or snow), and the deposition process (in-cloud or below-cloud). Examples can be found in Dare, Smith and Naughton (2016), Folch et al. (2020), Leadbetter et al. (2015), and Webster and Thomson (2017). Particle aggregation can either enhance or delay sedimentation of tephra particles (Brown et al., 2012; Rossi et al., 2021) (see Section 2.3.3). However, aggregation is a complex and highly uncertain process to simulate and incurs a high computational cost. Therefore, TTDMs usually account for aggregation in a simplified way, involving the modification of the TGSD by adding or removing particle classes from the original distribution (F. M. Beckett et al., 2020; Costa et al., 2010; Folch et al., 2010).

TTDMs provide results for tephra particles suspended in the atmosphere as well as deposited on the ground. For suspended material, concentration (mass per unit volume) and column mass load (column mass per unit area) are frequently calculated. In Lagrangian models, gridded concentration is computed from particle trajectories by calculating the mass of particles in each cell of a 3D array covering the domain of interest (D'Amours et al., 2015). The concentration will depend inversely on the volume of the cell and directly on the mass of all the particles in that volume (Draxler & Hess, 1997). A sufficient number of particles must be simulated to obtain an accurate estimation of the atmospheric concentration at the desired spatial and temporal resolution, and, depending on the simulation, this requirement may result in high computational costs. The use of kernel density estimators can mitigate this limitation. In this case, particle masses are distributed in space according to specific kernels (e.g., uniform, Gaussian, or parabolic), with kernel bandwidths usually defined as a function of particle age (A. Crawford, 2020). Thus, a single particle may be spread over multiple grid cells, and the gridded concentration is computed by summing the total mass in each cell. This technique usually produces smoother concentrations than the “pure particle” approach but involves a limited number of computational particles. Eulerian models calculate concentration explicitly in each grid cell and, for this reason, can be computationally more expensive than Lagrangian models, although in the latter the computational cost increases with the number of particles released.

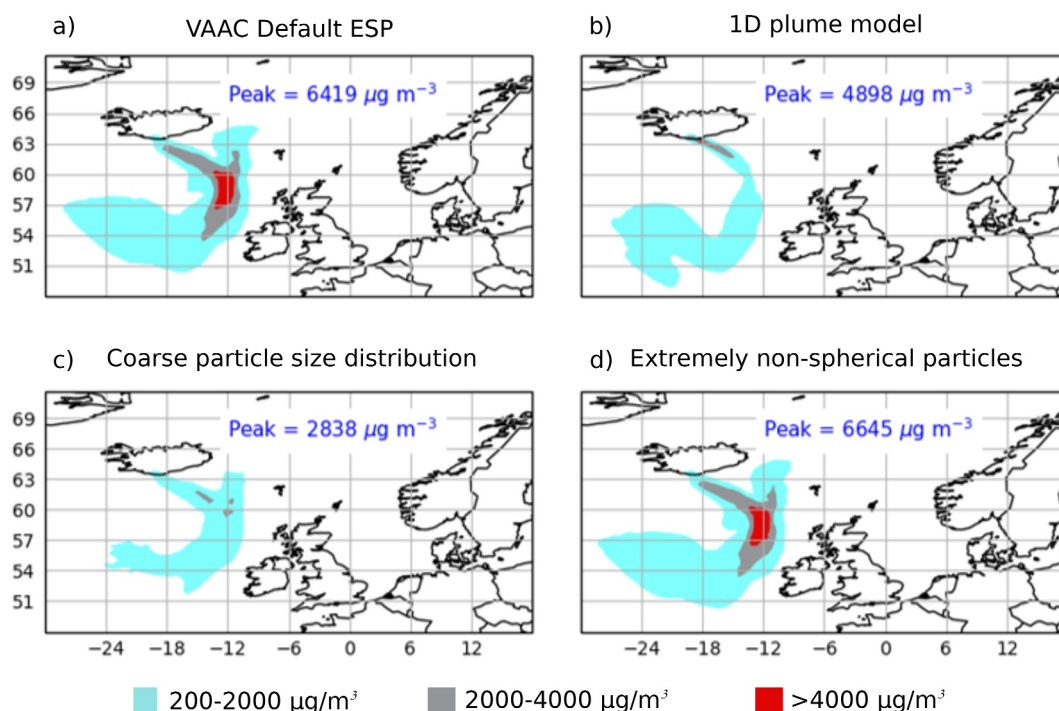


**Figure 14.** Effects of different initialization schemes on the results produced by Tephra transport and dispersal models. Six-hour averaged predicted ash concentration in the ash cloud of the 2010 Eyjafjallajökull eruption. Results are obtained from the Numerical Atmospheric-dispersion Modeling Environment model. The four maps show simulations initialized with various methods: (a) default initialization at the London Volcanic Ash Advisory Center (VAAC) (mass eruption rate [MER] estimated from the empirical relationship of Mastin et al. (2009) from plume height, mass is released uniformly from the vent to the top plume height, default particle size distribution and particle sphericity of 0.5), (b) MER and vertical distribution determined from the 1D plume model from Devenish (2013), (c) coarse particle size distribution derived from ground samples of the eruption of Hekla 1991 (Iceland), (d) non spherical particles with sphericity of 0.3. More information on the initialization schemes available at the London VAAC can be found in Table 1 of F. M. Beckett et al. (2020). Figure adapted from F. M. Beckett et al. (2020).

Different initialization strategies have a significant impact on the results provided by TTDMs about atmospheric ash concentration, both in terms of spatial extent of the simulated cloud and concentration at specific locations (Figure 14). Another important output obtained by TTDMs is the column mass load, which is the vertical integration of the mass of tephra in the atmosphere expressed as the mass of tephra per unit of area. Model validation is frequently done by comparing the calculated column mass load with the same quantity obtained from satellite retrievals (Corradini et al., 2010; Gouhier et al., 2020; Ishii et al., 2023; Kristiansen et al., 2015; Osman et al., 2020; A. T. Prata et al., 2022; Zidikheri et al., 2018). Alternatively, the horizontal extension of the simulated ash cloud is compared as categorical variable, that is, the presence or not of volcanic ash, against the detection of ash from satellite data considering an ash load threshold frequently between 0.1 and 0.2 g/m<sup>2</sup>, that is, limit of satellite detection (Collini et al., 2013; Dacre et al., 2016; M. S. Osoro et al., 2013; Webley et al., 2009). When using satellite retrievals to validate the results of TTDMs, it is important to consider that retrieval techniques based on radiative transfer theory are sensitive to particles with effective radii up to 10 µm. Therefore, proper caution should be exercised when comparing satellite data with the results of TTDMs, which do not have limits on the simulated particle sizes.

On the ground, TTDMs produce outputs displaying the thickness or the load (mass per unit area) of the resulting tephra deposit (e.g., Bonadonna, Phillips, & Houghton, 2005; Folch et al., 2009; Hurst & Davis, 2017). Simulated ground loads are often compared against loads derived from deposit sampling, serving both for model validation and for a more accurate characterization of the transport and deposition dynamics of tephra particles (e.g., Andronico, Del Bello, et al., 2021; A. T. Prata et al., 2021).

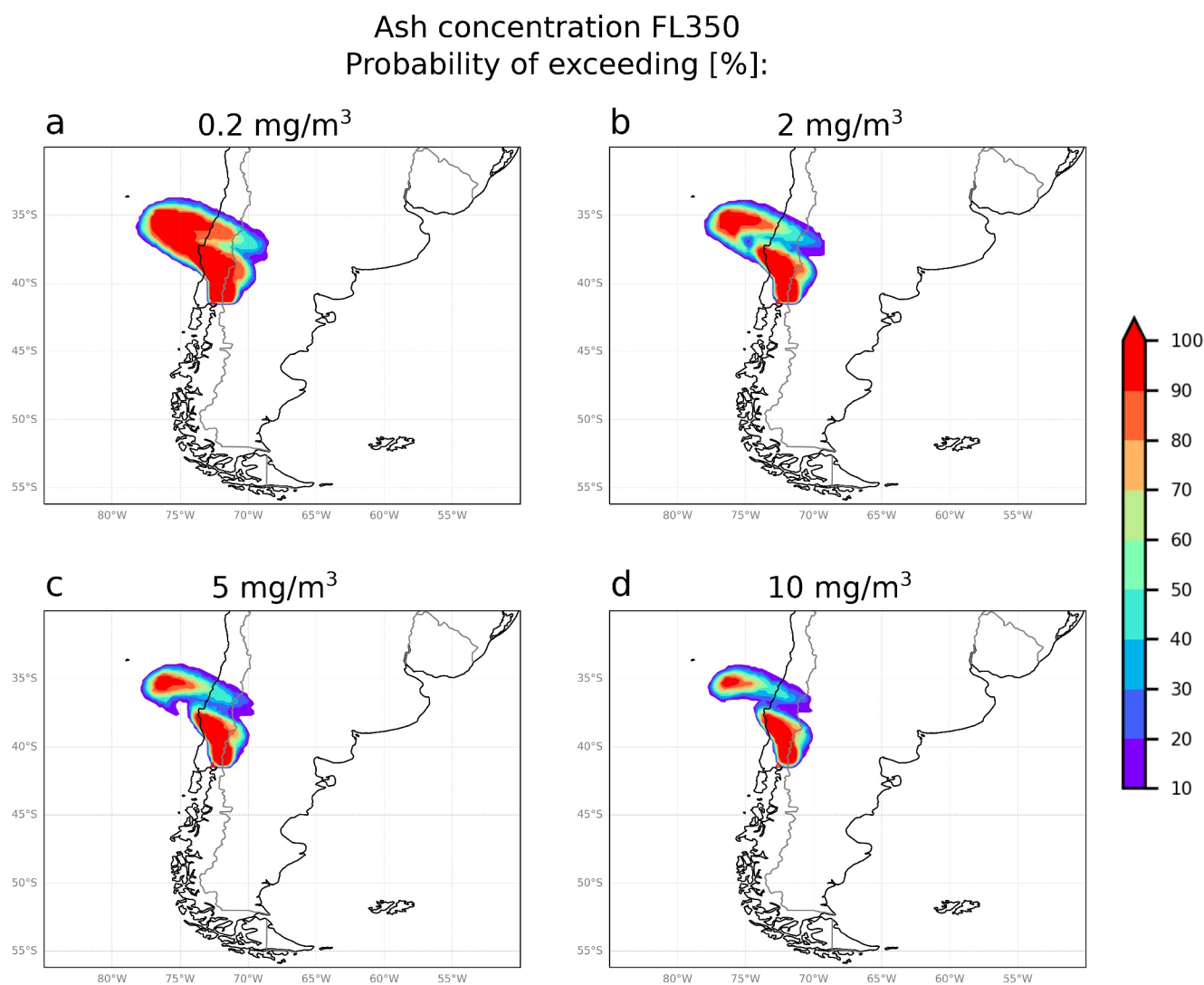


**Figure 15.** Example of probabilistic forecasts supplied by the Volcanic Ash Advisory Center Buenos Aires for the eruption of Calbuco (Chile, 2015). The four panels show the probability of exceeding ash concentration levels of 0.2 (panel a), 2 (panel b), 5 (panel c), and 10  $\text{mg}/\text{m}^3$  (panel d) for a specific Flight Level (FL350 in this case). The ensemble of simulations was generated by varying the plume top height (which affects the mass eruption rate estimations following Woodhouse et al. (2013)), altering the shape of the vertical profile of emissions by perturbing the Suzuki A parameter, and perturbing the wind field. The probability density functions were considered uniform, and random perturbations of the column height and wind field were applied, considering a 20% relative variation from the control setup. The Suzuki A parameter range was set to 2.

### 4.3. Ensemble Forecasting and Data Assimilation

In recent years, probabilistic approaches have emerged as the most robust way to provide maps of atmospheric tephra dispersal, even for operational applications. Various sources of uncertainty impact the accuracy of TTDM results, including uncertainties in ESPs, meteorological conditions, and model parametrization. Incorporating these elements and reflecting them in the results enhances the reliability of the forecasts supplied by TTDMs.

Probabilistic maps of atmospheric tephra concentration are generated by running ensembles of TTDM simulations (scenarios), each initialized with specific input conditions (eruptive and meteorological) and/or model parametrizations. To quantify uncertainties in eruptive conditions, ensemble construction is usually performed by defining probability distribution functions for some ESPs (typically only key parameters such as column height, MER, eruption duration, and TGSD). Sampling techniques (e.g., Monte Carlo or Latin Hypercube Sampling) are applied to generate a discrete number of eruption input conditions (usually tens to thousands). Each eruption condition is then used to initialize a simulation, leading to the creation of an ensemble of runs. Uncertainties in atmospheric conditions can be accounted for by using ensemble data sets produced by numerical weather

prediction models. These data sets are constructed by running many realizations of the numerical weather prediction model under perturbed initial conditions to obtain a set of different but equally probable states of the atmosphere. The paper by Trancoso et al. (2022) shows an example of ensemble construction where both eruption and meteorological uncertainties are accounted for. After running the ensemble of simulations, numerical results are processed and expressed in statistical terms, such as the probability of exceeding certain thresholds of atmospheric concentration (Figure 15). Some examples of ensemble forecasting are presented in Dare, Smith and Naughton (2016), Folch, Mingari, and Prata (2022), Pardini et al. (2022), and Plu et al. (2021).

As a further step, ensemble-based forecasting can significantly benefit from data assimilation procedures aimed at improving the numerical results with information from observational data. In this framework, the numerical results define the a-priori forecast state from which the a-posteriori state is obtained once the observational data have been included. Data assimilation schemes can be applied to improve both the estimation of ESPs and the tracking of ash clouds. Optimized ESPs can be estimated using inversion modeling techniques based on a series of satellite observations or sampling of the deposit (e.g., Constantinescu et al., 2024; Eckhardt et al., 2008; Moiseenko & Malik, 2019). A first inversion scheme was developed by Seibert (2000) for anthropogenic sulfur emissions and subsequent works further refined this approach for volcanic species such as ash and SO<sub>2</sub> (e.g., Eckhardt et al., 2008). For the 2010 volcanic eruption of Eyjafjallajökull, Stohl et al. (2011) proposed an inversion scheme through which the authors estimated, for the first time, the volcanic ash source strength as a function of height and time. The authors set thousands of different a-priori emission scenarios, and for each of them, numerical simulations were performed through FLEXPART to evaluate the atmospheric ash loadings at different times. Time-consistent numerical forecasts and satellite retrievals were input into the inversion algorithm, which optimally combined all the information to provide the best a-posteriori ash emission profiles as a function of time and height. The parameters considered in the inversion scheme were column mass load and cloud height, both supplied by the satellite retrievals and by the numerical forecasts, allowing for a meaningful comparison. The numerical forecasts obtained from optimum emission profiles were then evaluated using independent observational data coming from webcams, lidars, and aircraft. The algorithm proposed by Stohl et al. (2011) was later applied by Kristiansen et al. (2012, 2015), expanding the method to different case studies, numerical models, meteorological data, and observations. Another inversion algorithm was developed by Zidikheri et al. (2014). In this scheme, which is inherently probabilistic, the emission profile is not reconstructed in detail, but a best estimate of top plume height is obtained from a parametric study where the results of numerical simulations are compared against satellite observations.

Other methods to enhance numerical forecasts using observational data involve the application of variational and sequential techniques of data assimilation. Variational assimilation seeks to find the best estimate of the state of a system by minimizing a cost function, which represents the difference between the a-priori model state from simulations and the model state derived from observations collected in a time window, typically a few hours. In Lu et al. (2016) (and previous works), a variational algorithm called *Trj4Dvar* is proposed to estimate ash emission profiles (both rate and vertical structure) by refining the results of numerical transport models with observational data from ground- and satellite-based measurements. Another variational data assimilation scheme for volcanic ash was proposed by Ishii (2018). In this study, the author obtained ash emission vertical profiles as a function of particle size by assimilating data from meteorological radar and information on the fall deposit. The study demonstrated that the ash fall forecast derived from the assimilated emission profiles is more consistent with the ash fall observations than the a-priori guess. The main limitation of the method is that fine ash emissions from the upper region of the eruption column are not represented by the ash fall observations since finer particles are not present in the deposit. Thus, further research is needed to incorporate data from satellite sensors which, in contrast to the deposit, carry information about the finest particles.

Another type of data assimilation increasingly applied in volcanology is sequential data assimilation. In sequential methods, the numerical model is integrated forward in time and, whenever measurements are available, these are assimilated to produce an updated state (usually called *analyzed state*) with minimized errors relative to previous model results and observations. The *analyzed state* is then used to reinitialize the model before the integration continues. When new observations become available, a new assimilation cycle is performed, and a *new analyzed state* is computed. Among sequential methods, Kalman Filters are widely applied algorithms that have undergone significant development in both mathematical formulations and applications since their initial formulation (Kalman, 1960). One notable innovation has been the development of the Ensemble Kalman Filters to address large-scale problems (Burgers et al., 1998; Evensen, 1994). Classical Kalman Filters often require

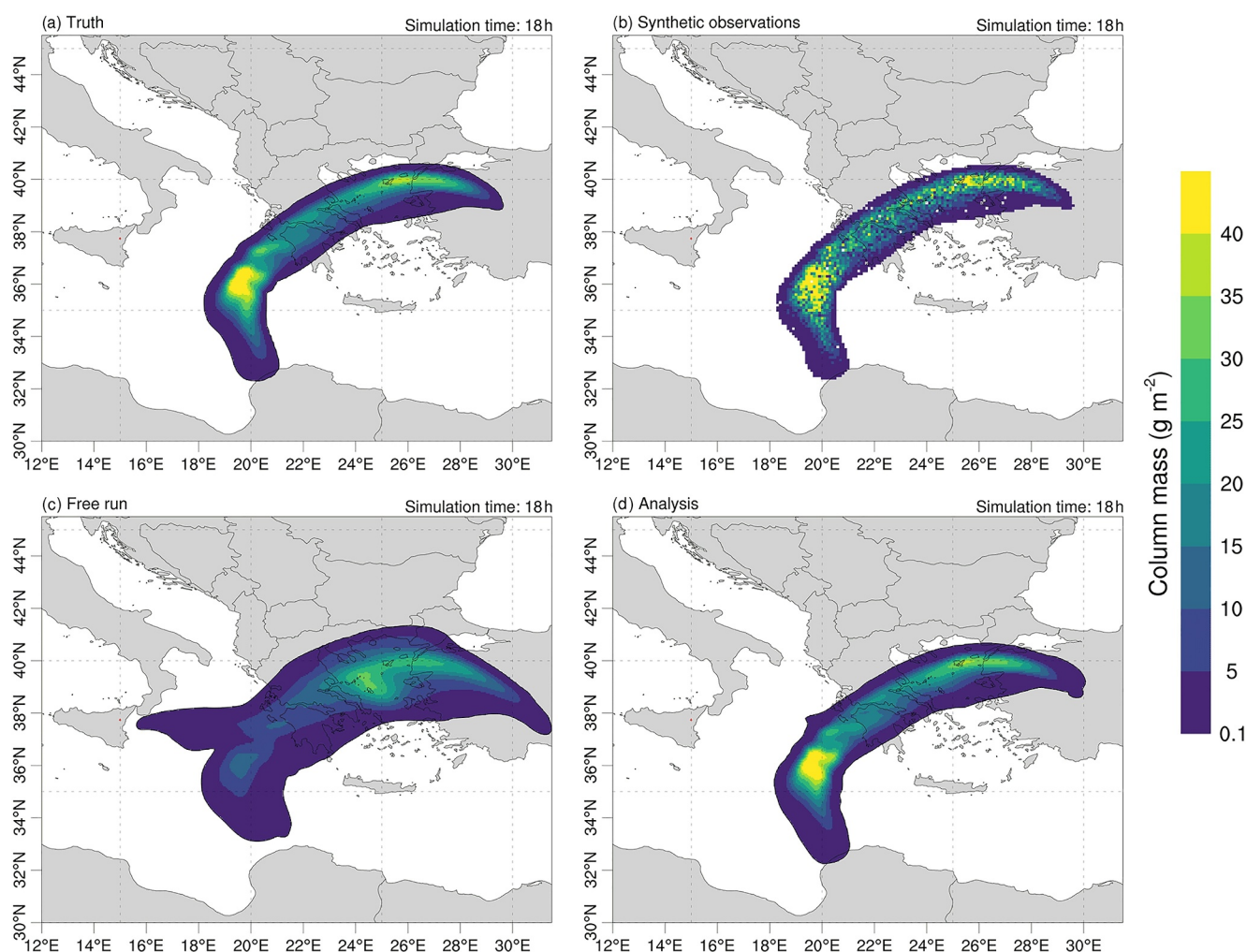


**Figure 16.** Spatial distribution of column mass load of volcanic ash for a data assimilation experiment performed using the FALL3D model and an eruption occurring at Mount Etna as a case of study. Panel (a) gives the true state from a single run performed by assuming a time-varying emission. In panel (b) synthetic satellite observations of the volcanic cloud are represented. The a-priori state, obtained without data assimilation, is displayed in panel (c), while in panel (d) is shown the a-posteriori state obtained by combining numerical results and observation through a data assimilation scheme based on Kalman Filters. Figure from L. Mingari et al. (2022).

substantial computational resources to handle and compute error statistics. Ensemble Kalman Filters overcome this limitation by applying a Monte-Carlo method to evaluate error statistics. Ensemble Kalman Filters compute error statistics using an ensemble of model realizations to represent the state estimate as a mean state (i.e., ensemble mean) and a covariance matrix (i.e., ensemble covariance). Studies by Fu et al. (2017), L. Mingari et al. (2022), S. Osoro et al. (2020), and Pardini et al. (2020) show the application of Ensemble Kalman Filters to enhance the tracking and forecasting of volcanic ash clouds (Figure 16). These investigations involve testing different TTDMs, such as HYSPLIT and FALL3D, along with observational data, both real and synthetic, from satellite and aircraft sensors. The authors demonstrated that ash forecasts strongly benefit from the assimilation of observational data, although some typical limitations of Kalman Filters may lead to suboptimal filter performance. For instance, a basic assumption of Kalman Filters is that all error and noise processes are Gaussian. This assumption is not always met by the a-priori state produced by TTDMs, where non-Gaussian and positively skewed distributions of the variables to be assimilated are present (e.g., column mass load). Thus, assimilation results should be carefully checked, and appropriate methodologies should be adopted to handle this problem. Together with Kalman Filters methods, recent works have developed filtering techniques where large ensembles are filtered with respect to observations to produce refined forecasts (Capponi et al., 2022; Zidikheri & Lucas, 2021a, 2021b).

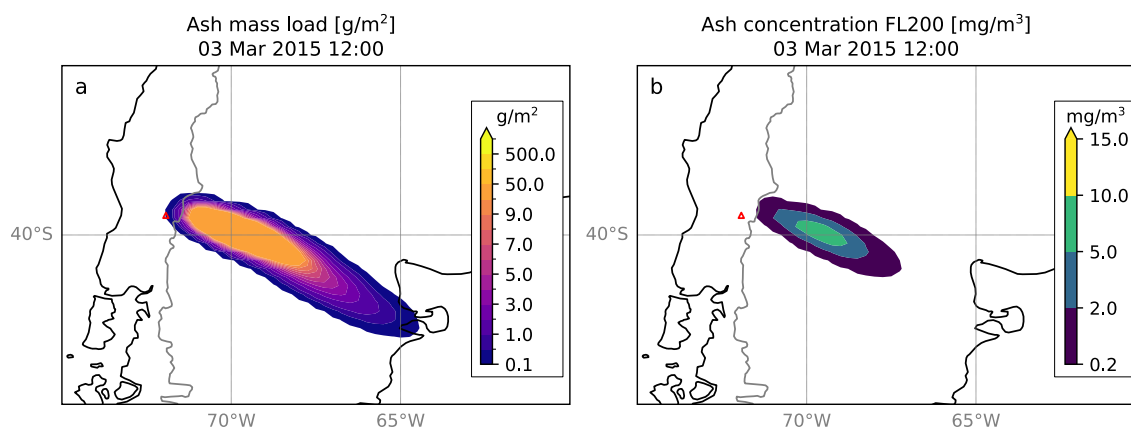


**Figure 17.** Examples of operational numerical forecasts supplied by the Volcanic Ash Advisory Center (VAAC) Buenos Aires showing ash mass load (panel a) and concentration at FL200 (panel b) for an eruption at Villarrica volcano that occurred on 3 March 2015 (the location of the volcano is indicated with a red triangle). The forecasts are valid on 3 March 2015 at 12:00 UTC and are produced running the FALL3D model in a deterministic mode, with meteorological conditions from Global Forecasting System, a 12 km plume top height (mass eruption rate estimated using Woodhouse et al. (2013)), and 1 hr of release. The operational configuration of VAACs is presented in F. M. Beckett et al. (2024). The thresholds of ash concentration in panel (b) are based on International Airways Volcano Watch Roadmap (ICAO, 2021).

Although data assimilation is primarily a research topic at present, some operational applications are emerging and are currently being implemented for the real-time forecasting of volcanic clouds. In recent years, a data assimilation procedure based on the Inversion Technique for Emission Modeling (InTEM) inversion technique (Pelley et al., 2015, 2021) has been implemented for operational forecasting by the London VAAC. This procedure combines satellite retrievals of ash mass loading with results from the NAME model to improve the estimates of MER, time variation, and vertical distribution of ash emission profiles at the vent (F. M. Beckett et al., 2020). Additionally, the Darwin VAAC uses data insertion and ensemble filtering for operational forecasting, combining numerical results from HYSPLIT, VOLcanic Cloud Analysis Toolkit (VOLCAT) satellite retrievals of ash mass loading, and the polygon that encloses the observed volcanic ash produced by a forecaster (Zidikeri & Lucas, 2021a, 2021b).

#### 4.4. Operational Numerical Forecasting

We refer to *operational numerical forecasting* as the use of TTDMs to provide real-time forecasts of tephra dispersal and deposition during explosive eruptions. The production of forecasts specifically designed for aviation safety (in this case the focus is on atmospheric ash clouds) is the object of extensive work and regulation. In the framework of the International Airways Volcano Watch (IAVW) administered by the ICAO, nine VAACs, SVOs, Meteorological Watch Offices (MWO), and Area Control Centers (ACCs) collaborate in the surveillance of volcanic emissions to contribute to flight safety (Lechner et al., 2018). In particular, VAACs are responsible for running TTDMs to forecast the expected extent of volcanic ash clouds (ICAO, 2010; Annex 3). Figure 17 provides an example of operational numerical forecasts supplied by the VAAC Buenos Aires for Villarrica volcano (Chile). Additionally, specialized agencies use TTDMs for national civil protection to mitigate the impacts of tephra fallout and atmospheric dispersion. For instance, the Japanese Meteorological Agency (JMA) produces daily forecasts of volcanic tephra fallout when an eruption occurs, which are used to recommend actions for the public (Hasegawa et al., 2015). Other national-level entities like IMO, INGV, and USGS, which manage the SVOs in Iceland, Italy, and the United States respectively, run TTDMs for operational forecasting over regional or local domains (Figure 18). During explosive eruptions, they often produce forecasts of atmospheric concentration and cumulative tephra load at the ground. This information is crucial not only for airport operations but also for informing civil protection authorities about potential impact on infrastructure and population.

To provide reliable forecasts, observational data of the ongoing eruption should be used to initialize TTDMs. For monitored volcanoes, some important ESPs can be retrieved in real-time from ground or satellite observations. These typically include column height, eruption onset, and eruption duration. However, in cases of unfavorable meteorological conditions or limited visibility of the volcanic activity (e.g., nighttime), difficulties may arise in constraining such parameters, even for well monitored volcanoes. Other ESPs, such as TGSD and MER, are more

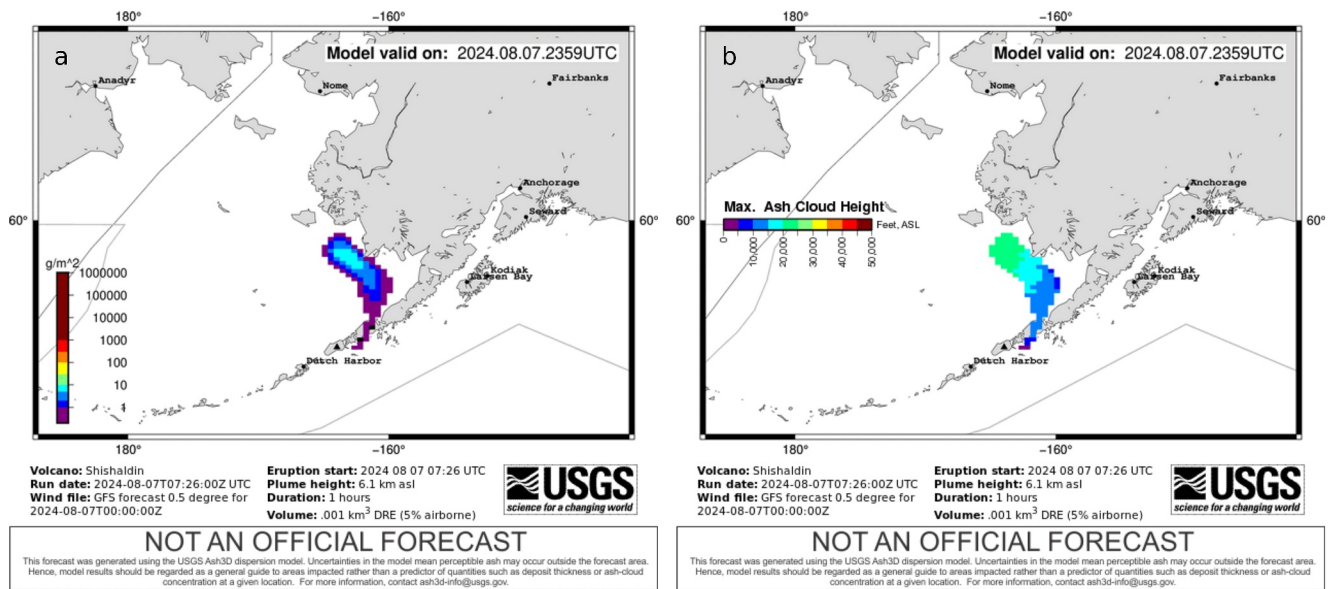


**Figure 18.** Example output from the operational dispersion model Ash3d, used at the Alaska Volcano Observatory to forecast ash hazards during periods of unrest. The example shown simulates a hypothetical ash cloud from Shishaldin volcano on 7 August 2024, using source parameters that are considered realistic for that volcano. Panel (a) shows ash column amount in  $\text{g}/\text{m}^2$  as simulated by Ash3d, while panel (b) shows the maximum height of the cloud in feet above the sea level. Results are publicly available at the Alaska Volcano Observatory website: <https://avo.alaska.edu/>.

challenging to constrain in real-time (Zidikheri et al., 2017). While estimates of MER can be supplied from column height using parametrization schemes (e.g., Mastin et al., 2009), TGSD usually remain unconstrained and defined from tabulated data of past eruptions (e.g., the IVESPA database). The lack of key parameters for model initialization inevitably introduces uncertainties in model results, which should be carefully quantified and treated using appropriate techniques (e.g., Pardini et al., 2022).

The role of the SVOs and VAACs is crucial for the initialization of TTDMs with timely information of the ongoing eruption (Engwell et al., 2021). SVOs have the legal mandate to monitor volcanoes and inform the aviation stakeholders about impending eruptions and, whenever an eruption starts, to provide information about the ongoing activity. Within the IAVW framework, SVOs are required to develop capabilities to assess key ESPs which are needed by the VAACs to produce volcanic ash forecasts that will, eventually, be distributed to the airline companies for safety risk assessment. Specifically, the Annex 3 of the Convention on International Civil Aviation (ICAO, 2010) states that SVOs are recommended to distribute the following information: “for volcanic eruption: the date/time (UTC) of report and time of eruption (UTC) if different from time of report; name and, if known, number of the volcano; location (latitude/longitude); and description of the eruption including whether an ash column was ejected and, if so, an estimate of height of ash column and the extent of any visible volcanic ash cloud, during and following an eruption.” Further, in the Handbook for IAVW (ICAO, 2020), SVOs are recommended to distribute the above information through a structured and formatted message, namely a VONA. VONAs are primarily distributed to the aviation community via email and are often, but not always, made public on institutional websites (Barsotti et al., 2024). In the current VONA structure, *field\_13* requires to report the best estimate of ash-cloud top, as this parameter has the largest effect on model results and it would have a major impact on the extent and location of the area forecast to be contaminated by ash (F. M. Beckett et al., 2020; Pardini et al., 2022).

In the framework of IAVW, the VAACs continuously monitor satellite products, volcano web cameras, and in situ data, 24 hr a day to detect the onset of an eruption or the presence of ash in the atmosphere due to ash remobilization. According to the Handbook for IAVW (ICAO, 2020), as soon as VAACs identify atmospheric ash or are notified of its presence by an ACC, MWO, SVO, or any other source, they are required to run the TTDM and produce a volcanic ash advisory. Volcanic ash advisories contain information about the eruption, the vertical and horizontal extent of the ash cloud, its direction and speed of movement, and the forecast movement of the ash cloud (ICAO, 2020). If information regarding the onset of the eruption or the presence of volcanic ash in the

atmosphere is received from a source other than an ACC or MWO, the VAACs should immediately convey this information by phone to the ACC and/or MWO directly affected by the volcanic ash. Subsequently, they should issue a volcanic ash advisory to notify the rest of the users. As aircraft far from a volcanic cloud can reach speeds of 850–900 km/hr at cruising altitudes, covering great distances in a short time, the VAAC can issue an initial volcanic ash advisory without a forecast to promptly alert air traffic controllers about the hazardous conditions, and, as soon as possible, issue a following complete advisory including the forecast.

To produce real-time estimates of cloud height, SVOs rely on data from monitoring networks, which include visible and infrared cameras, weather radars, ground-based lidars and satellites (see Section 3 for more details). Direct (visual) observations from the ground are also used, but they often underestimate the actual altitudes of volcanic plumes. When SVOs monitor volcanoes with ground-based instruments, the onset of an eruption can be detected within the first few minutes. However, in cases where volcanoes are not monitored with ground instruments, the onset can be detected by satellites, which may introduce a latency of more than 10 min. VAACs also estimate cloud height by combining infrared satellite data and atmospheric data, continuously monitoring volcanic activity throughout the year and maintaining constant communication with SVOs. To estimate plume height in real-time using satellite data, the correlation between the coldest brightness temperature in the 11  $\mu\text{m}$  infrared band of the plume, obtained from satellite imagery, and an atmospheric thermal profile is frequently used. The atmospheric thermal profile can be derived from a nearby radiosonde (Sawada, 1987) or extracted from an atmospheric model (Pavolonis et al., 2015a). Depending on the structure of the atmospheric thermal profile, the correlation may yield a unique solution or multiple solutions, particularly in the presence of a thermal inversion (Horváth et al., 2022). From a satellite perspective, automated systems can also support SVOs and VAACs. An example is the VOLCAT, which integrates data from various geostationary and polar-orbiting satellites to provide early detection of eruptions and estimate ESPs such as cloud height and ash mass loading (Pavolonis et al., 2015a, 2015b, 2018). Moreover, during flights, pilots can report observations of volcanic ash emissions to the ACCs, which are distributed in the aeronautical communication system as Pilot Special Reports (PIREP).

During an ongoing event, the eruption conditions often change over time, and these changes may occur without warning and in unexpected ways. The accuracy of operational numerical forecasting is highly dependent on the ability to update the initialization of TTDMs (and thus the final forecasts) based on the latest available information on eruption conditions. Therefore, real-time accessibility to monitoring data and estimates produced by SVOs should be ensured especially for operational numerical forecasting. However, at present, the capability of SVOs worldwide to disseminate information in real-time via VONA is highly uneven and depends on the level of preparedness, as well as on the availability of resources and infrastructures.

#### 4.5. Long-Term Aviation Hazard Assessment

Alongside the operational use during eruptive crises, TTDMs are widely applied also for quantifying volcanic hazards associated with hypothetical future eruptions at volcanoes that are not necessarily restless. In this case, we refer to long-term hazard assessment. For tephra dispersal, it aims at supplying hazard maps showing to which extent airspaces might be impacted by tephra produced by hypothetical explosive eruptions (Figure 19). The outcomes of this analysis could support civil aviation authorities, airline companies, and decision-makers in defining risk mitigation plans to carry out in case of an eruption, but also in land-use planning and for identifying vulnerable areas at risk (Montesinos et al., 2022; Titos et al., 2022).

Traditionally, long-term hazard assessment relies on the definition of “eruption scenarios” constructed from the knowledge of the investigated volcanic system (Bonadonna, 2006; Bonadonna et al., 2021). Different eruption styles are generally translated into different scenarios, and complex eruptions can be defined, spanning from individual eruptive episodes to long-lasting activity where different eruptive episodes of different size and intensity may occur over a certain period of time. Several uncertainties affect the definition of a scenario. While estimates of possible column height, eruptive volume, and eruption duration should be supplied, such estimates are often very uncertain, especially for long-quiescent volcanoes. Depending on the volcanic system, even the location of the eruptive vent can be unknown or subject to high uncertainties. Despite uncertainties and unknowns, eruption scenarios are defined from historical and/or geological records of the volcano under study (or analog volcanoes), expert opinion (M. S. Bebbington et al., 2018), reconstructed ESPs (Aubry et al., 2021; Engwell et al., 2021; Mastin et al., 2009), and observational data collected during similar volcanic events. In some instances, long-term hazard assessment investigating impact on aviation has been conducted for a single specific

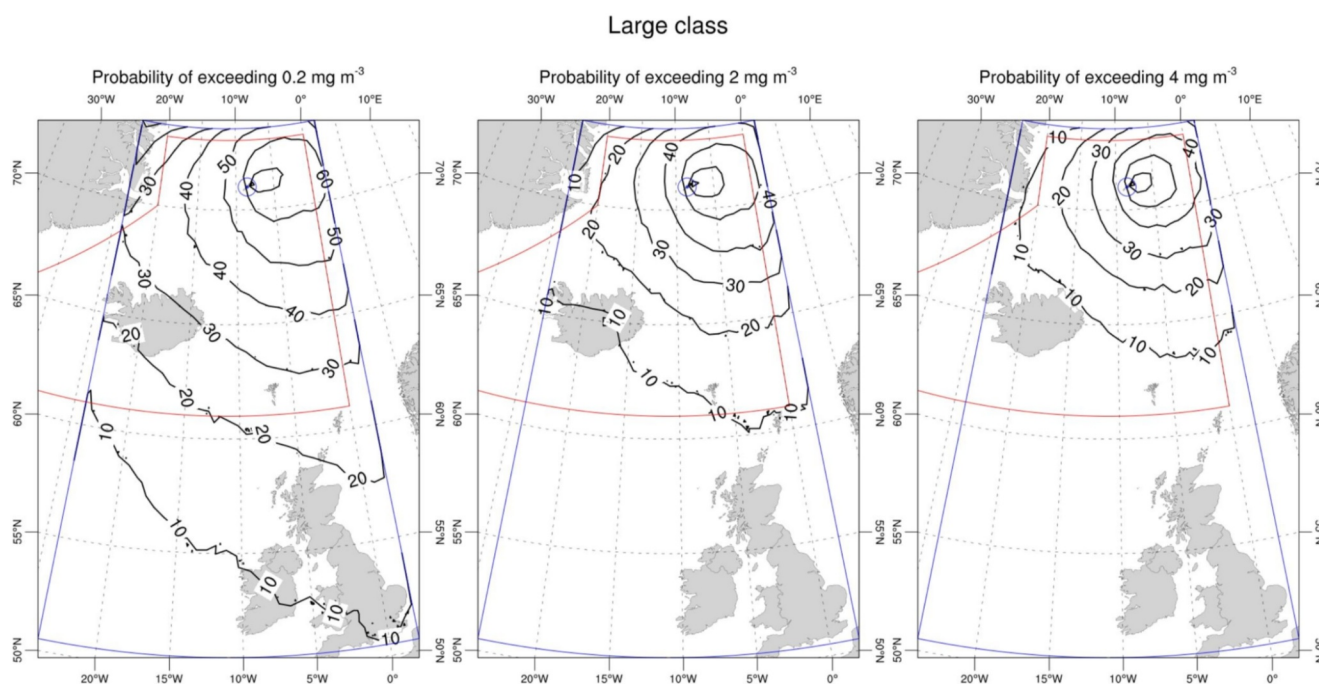


**Figure 19.** Some results of the long-term hazard assessment conducted at Jan Mayen volcano (Norway). The three panels display the probability of exceeding ash concentrations of 0.2 (left), 2 (middle), and 4  $\text{mg m}^{-3}$  (right) at FL050. The eruption scenario considered to construct these maps assumes Volcanic Explosivity Index = 4, total erupted volume  $>0.5 \text{ km}^3$ , and a duration of 1–5 days (referred to as large class). Figure extracted from Titos et al. (2022).

eruptive scenario (Barsotti et al., 2018; Bonasia et al., 2014; Folch & Sulpizio, 2010; Sulpizio et al., 2012), in others these studies have been performed by accounting for a plethora of scenarios and conducting a fully probabilistic hazard assessment (Biass et al., 2014; Montesinos et al., 2022; Titos et al., 2022; Volentik & Houghton, 2015).

In addition to which scenario to simulate and how, it is also important to account for the variability of the meteorological conditions under which eruptions may occur. Such future conditions are uncertain but, at the same time, need to be carefully constrained since they influence the release of tephra particles into the atmosphere and their subsequent atmospheric transport and deposition. Considering the complexity of the problem, probabilistic approaches enable these analyses, including the many sources of uncertainty present in both eruption and meteorological conditions. To do this, ensemble-based simulations are performed as done for the ensemble-forecasting. In the case of probabilistic long-term hazard assessment, the eruption conditions are sampled from probability distributions (probability density functions) derived from analyses conducted over the investigated volcano (e.g., from historical/geological records, expert opinion, observations), or the scenario is predefined and identified by a specific set of parameters (scenario-based approach). The meteorological conditions are sampled from a reanalysis data set of a sufficient duration to incorporate much of their likely variability (usually one or two decades). This means that the eruption start time is defined stochastically by randomly sampling a start date in the reanalysis data set. This methodology assumes that a record of past meteorological conditions is representative of the future state of the atmosphere. We highlight that the rapid climate changes driven by anthropogenic activities may have some effects on this hypothesis. It is now clear that volcanic activity (from pre-eruptive to post-eruptive processes) can be impacted by climate change and such effect should be taken into consideration in the light of volcanic hazard assessment (Aubry et al., 2022). Once a proper set of initial volcanological and meteorological conditions has been defined, ensembles of simulations are run in order to produce the probabilistic outcomes of interest. Usually, hundreds to thousands of simulations need to be performed to fully capture the variability of the conditions under which tephra emission and dispersion take place. However, the computational times are not subject to the limitations typical of the operational forecasting (Bonasia et al., 2014; Titos et al., 2022).

Long-term hazard assessment is a fundamental tool for volcanic hazard mitigation and extensive analyses should be performed to cover the majority of the active or quiescent volcanoes, especially those considered hazardous

and located in densely populated areas. We also remark the importance of updating old analyses in the light of new observational data and recent advances in numerical modeling.

## 5. Conclusions and Future Directions

Recent decades have seen a substantial advancement in our conceptual understanding of what drives tephra plumes and the dynamics of volcanic clouds. Quantitative descriptions of tephra generation within the conduit, plume ascent, and cloud dispersal have become possible through the application of principles from disciplines, such as fluid dynamics and thermodynamics. These contributions have facilitated the development of numerical models, which, as a consequence of advances in computational capacity and capability, have now become fundamental tools in volcanology for both research and hazard-oriented applications.

A growing number of techniques and applications that are well-established in atmospheric science are being increasingly applied to the study of volcanic processes, significantly enhancing the modeling of tephra dispersal. For example, data assimilation and plume-in-grid models (Carrassi et al., 2018; Karamchandani et al., 2002; Marécal et al., 2023; Sun et al., 2022), which are common in atmospheric science, have only begun to be explored in volcanology over the past decade, and their application is expected to expand rapidly in the future. This process has evolved and benefited from our increasing capabilities for observing tephra plumes and clouds from different platforms (ground, space, and airborne). These observations are of paramount importance today, enhancing the theoretical understanding of explosive eruptions, the modeling, and the hazard assessment. As a consequence, a large number of eruptions can be considered well-studied today, including low-magnitude events that were generally underrated.

Nevertheless, the natural variability exhibited by explosive eruptions in terms of their style, location, and peculiar features makes it extremely challenging to attain a comprehensive understanding of their dynamics and complicates our monitoring capabilities. A key challenge has always been to relate models to observations. Large plumes occur infrequently, and all plumes, both large and small, have been difficult to characterize, given the limitations of satellite technology, ground-based instrumentation, and visual observations. Global compilation of observations of plume height and MER, for example, seem not accurate enough to resolve effects of wind or humidity, which we predict are important (Aubry, Engwell et al., 2023; Mastin, 2014). Thus, observational improvements are likely the next frontier, and are advancing rapidly. Utilizing such observations to enhance modeling, particularly for poorly explored processes like aggregation and in-plume water changes, and achieving a deep integration between monitoring and modeling is another key aspect for the future.

### 5.1. Future Trends in Ground-Based Monitoring

Emergent technologies, such as infrasound (Fee & Matoza, 2013) and global lightning detection networks (Nag et al., 2015), are expected to improve and be consolidated as monitoring techniques. This will undoubtedly facilitate early detection of explosive eruption, with benefits for timely risk mitigation plans. The extensive data set obtained through these systems will likely contribute to the training of machine learning algorithms for the rapid discrimination and possibly quantification of volcanic activity. Examples can be already found in Cannata et al. (2011), L. M. Watson (2020), Witsil and Johnson (2020), and we expect that applications will increase in the future. Such a trend is expected to involve other mature monitoring techniques, such as visible and thermal cameras among others. Prototype workflows for automated plume detection and, for example, estimation of plume height without the need for an operator are currently emerging, despite not yet being used operationally (Aravena et al., 2023; Corradino et al., 2020; Guerrero Tello et al., 2022; Simionato et al., 2022; Valade et al., 2014; Wilkes et al., 2022).

At the present time, good chances exist to provide real-time estimates of plume/cloud height during explosive eruptions (as we discussed in Section 3). However, real-time information on particle size is still missing due to the inherent difficulties in retrieving this parameter while the eruption is ongoing. Developments in existing monitoring techniques are expected to fill this gap. In recent years, studies conducted at Sakurajima (Japan), Mount Etna (Italy), and Stromboli (Italy) have shown that disdrometers are promising tools for real-time characterization of tephra particles and ground accumulation (Freret-Lorgeril et al., 2019; Freret-Lorgeril, Bonadonna, Rossi, et al., 2022; Kozono et al., 2019; Takishita et al., 2022). In particular, recent studies have demonstrated the capacity of optical disdrometers to provide information on both individual particles and falling aggregates

necessary to derive the TGSD needed for tephra dispersal forecasting (Freret-Lorgeril, Bonadonna, Rossi, et al., 2022).

Multi-sensor strategies that combine different methodologies and sensors provide additional insights into ESPs, such as plume height, MER, and TGSD (Corradini et al., 2016; Freret-Lorgeril et al., 2021; Freret-Lorgeril, Bonadonna, Corradini, et al., 2022; Poret et al., 2018; Scollo et al., 2020). However, their application is not straightforward, especially in real-time scenarios. Reasons include frequent limitations in the monitoring apparatus at specific volcanoes, as well as variability in eruption style and conditions that hinder the use of various tools due to the limits of each technique. When possible, multi-sensor approaches have proven to be successful in enabling a comprehensive characterization of source dynamics (especially if also including data from satellite-based sensors) and improving the initialization of numerical models, including both plume models and TTDMs. However, further tests and verification are needed to expand this approach to various volcanoes and eruption styles.

UV cameras used in volcanology for measuring SO<sub>2</sub> emissions, can be deployed for the detection and characterization of volcanic ash plumes (Burton, 2016). Although UV cameras have not yet been extensively used for the ground-based quantification of ash emission, a few studies show promising results. The first application was proposed by Yamamoto et al. (2008) at Santiaguito volcano. By combining field measurements and fundamental fluid-dynamics, the authors proposed a method to constrain ash mass distribution inside the plumes produced by small scale eruptions. In a subsequent paper also focused on mild explosions at Santiaguito volcano, Esse et al. (2018) show that with UV imaging it is possible to quantify ash settling velocity by measuring the depolarization of scattered sunlight by non-spherical ash particles.

Unmanned Aerial Vehicles (UAVs) have been recently deployed for the real-time detection of volcanic plumes and clouds. Compared to research aircraft, UAVs are less expensive, safer and enable more deployable instruments to monitor low-intensity ash emissions. Since the pioneering campaign conducted by McGonigle et al. (2008) at La Fossa crater (Italy) to measure fluxes of volcanic carbon dioxide, new campaigns have been conducted at Mount Ontake (Japan; Mori et al., 2016), Yasur volcano (Vanuatu; Gomez & Kennedy, 2018), and Fuego volcano (Guatemala; Schellenberg et al., 2019). The aim of these studies is to demonstrate that UAVs equipped with appropriate instruments can help to detect ash plumes, sample ash particles and, as shown by Gomez and Kennedy (2018), to reconstruct the 3D structure of the plume.

Finally, we highlight the growing role of social media in crowdsourcing and sharing observations about volcanic eruptions and potential volcanic crises (Balague-Tarriela et al., 2022). This role is twofold. On one end, the rapid dissemination of information builds social awareness of volcanism. On the other hand, photos and videos from people witnessing an eruption can provide valuable observations of that event, essentially filling gaps when official monitoring systems are lacking or rendered inoperative by the event.

## 5.2. Future Trends in Satellite-Based Monitoring

Since the first attempts to objectively and quantitatively monitor volcanic ash from satellites were made, tremendous advances in sensor technology have occurred. Perhaps the most significant paradigm shift in sensor technology over the last decade has been the move toward advanced geostationary imagers. Advanced geostationary imagers (e.g., ABI, AHL, FCI, AMI, AGRI) now have high temporal (1–10 min) and spatial (0.5–2 km) resolution in addition to new channels that capture the spectral signature of common volcanic cloud constituents such as SO<sub>2</sub>, sulfates, ash, and ice. For example, A. T. Prata et al. (2022) found that by using multiple thermal infrared channels, which are now available from most advanced geostationary imagers, allow for the retrieval of a wider range of ash particle sizes than traditional approaches which only use two channels (i.e., the 11 and 12 μm channels). The practical implication of this finding is that drifting ash clouds may now be tracked for longer as smaller particles will have longer atmospheric residence times (Rose & Durant, 2009; Rose et al., 2001). Geostationary satellites now cover almost the entire globe (with Sun-synchronous satellites covering the poles), which has led to new geometric height estimation methods (Horváth, Carr, et al., 2021; Horváth, Girina, et al., 2021) and, owing to their overlapping fields of view, offer the opportunity to estimate height at high temporal frequency based upon parallax methods (Carr et al., 2022; Proud et al., 2022). The higher temporal frequency of modern satellites increases the opportunity of catching the maximum height of a fluctuating plume such as that in the 2022

Hunga eruption (Proud et al., 2022). Some of the new generation of geostationary satellites also host lightning mappers such as the Geostationary Lightning Mapper onboard GOES third generation satellites, Lightning Mapping Imager onboard the FengYun-4 series and the recently launched Lightning Imager onboard the Meteorat Third Generation satellite, MTG-I1. Volcanic lightning can be detected from lightning mappers positioned in geostationary orbit (e.g., Schultz et al., 2020) and so it is expected that methods for monitoring volcanic ash using lightning mappers will be developed into the future. In addition, the tremendous amount of data that geostationary satellites generate mean that research is now moving toward machine learning algorithms to not just improve ash discrimination (Gray & Bennartz, 2015; Pavolonis et al., 2015b; Petracca et al., 2022; Picchiani et al., 2011) and retrieval algorithms (Bugliaro et al., 2022; Piontek, Bugliaro, Kar, et al., 2021; Piontek, Bugliaro, Schmidl, et al., 2021; Piscini et al., 2014) but also take advantage of the unique temporal information that these satellites provide.

Advances in hyperspectral thermal infrared sounding of ash from polar orbit are expected to continue into the future with the launch of the IASI-New Generation (IASI-NG) sensor (Crevoisier et al., 2014; Vittorioso et al., 2021). The improved spectral resolution afforded by IASI-NG (double that of IASI) will lead to improved ash cloud height estimation, better ash composition characterization and may lead to algorithms that retrieve the ash particle size distribution directly (F. Prata & Lynch, 2019). Though there is a long heritage of algorithms developed for hyperspectral UV sensing of non-volcanic aerosols (Torres et al., 2007), for volcanic ash, these measurements are yet to be fully explored, in part due to the limited amount of complex refractive index data available (Carn & Krotkov, 2016). However, recent efforts have been made to better constrain these unknowns (Ball et al., 2015; Reed et al., 2018; Rocha-Lima et al., 2014) and it is expected that hyperspectral UV retrievals of volcanic ash will be developed in the future. Whilst much of the research on UV ash monitoring has involved analysis of Sun-synchronous satellites, the DSCOVR/EPIC platform, which is positioned at the Earth-Sun Lagrange point 1 (L1), has led to advances in tracking volcanic SO<sub>2</sub> at high cadence (every ~1 hr for the sunlit Earth; Carn et al., 2018) and can also be used to track volcanic ash using the UVAI (Gorkavvi et al., 2021). In the future, we expect to see more studies that leverage improved temporal tracking of ash from UV sensors in geostationary orbit such as GEMS with coverage over East Asia, the recently launched TEMPO with coverage over North America and the soon to be launched Sentinel-4 mission with coverage over Europe.

Whilst the majority of space-borne lidar research on volcanic ash has utilized CALIPSO data, the mission ended on 1 August 2023. The ICESat-2 mission is also an elastic backscatter lidar (Abdalati et al., 2010) and could therefore be used to monitor the vertical properties of ash clouds (e.g., geometric height and thickness); however, with the recent launch of the EarthCARE satellite (on 29 May 2024), new measurements from its Atmospheric Lidar (ATLID; Van Zadelhoff et al., 2023) offer an opportunity to continue the legacy of CALIPSO for volcanic ash monitoring. As discussed in A. T. Prata (2016), the EarthCARE mission (Illingworth et al., 2015; Wehr et al., 2023) promises to deliver advances in sensor synergy akin to NASA's A-train (Stephens et al., 2002) but aboard a single satellite platform, which includes a lidar, radar, multi-spectral imager, and broadband radiometer. Though the EarthCARE era has only just begun, we expect that its temporally and spatially collocated measurements utilizing both passive and active sensors across the visible, infrared, and microwave parts of the electromagnetic spectrum coupled with the new paradigm of advanced geostationary sensors will provide a more complete picture of volcanic ash dispersion into the atmosphere from source to long-range transport.

Though we expect to see further advances, some gaps in our present satellite-based ash monitoring capabilities are worthy of discussion. Namely, the inability to actively profile volcanic ash clouds (i.e., using lidar) at high temporal frequency and the limitations in retrieving certain particle size ranges that fall within tephra TGSDs. A lidar positioned in geostationary orbit would potentially allow for time and height resolved measurements of the 4D evolution of ash clouds. Direct observations of ash concentration, permitted by geostationary lidar, would provide a valuable data set for verifying dispersion model output and support new ash concentration forecast requirements from VAACs. Until geostationary lidar is achieved, it seems that the best technique to overcome this limitation is to combine polar-orbiting and geostationary imager measurements (for horizontal dispersion information) with dispersion models (for vertical profile information) using data insertion, assimilation and/or inversion (described in Section 4).

To date, algorithms designed for UV, visible, and thermal infrared measurements have been successfully applied to determine the properties of micron-sized ash particles and similar techniques have been applied to microwave sensors to retrieve properties of millimeter-sized ash particles. However, techniques to determine ash particle

sizes lying between these size ranges are still in their infancy. The far-infrared (FIR; 15–100  $\mu\text{m}$ ) and terahertz (THz) regions (0.1–10 THz; 0.03–3 mm) of the electromagnetic spectrum can be used to study sub-millimeter-sized particles from space (Eriksson et al., 2020; Li et al., 2023; Palchetti et al., 2020). Examples of upcoming missions aiming to retrieve ice particle properties in these size ranges include the Far-Infrared Outgoing Radiation Understanding and Monitoring (FORUM) mission (Palchetti et al., 2020; selected by ESA for launch in 2027) and Ice Cloud Imager onboard the MetOp-Second Generation mission (Eriksson et al., 2020; scheduled for launch in 2026). The challenge in the context of tephra monitoring in the atmosphere will be to determine how these FIR and THz measurements can be applied to volcanic ash clouds.

### 5.3. Future Trends in Modeling and Services

The April–May 2010 eruption of Eyjafjallajökull marked a turning point in tephra dispersal prediction and led to the definition of new guidelines for flying in the presence of volcanic clouds, shifting from a “zero-ash tolerance” to an “ash-avoidance” approach. This policy requires robust forecasting products based on a proper treatment of the many sources of uncertainties affecting the use of TTDMs (e.g., uncertainties in source term conditions, meteorological input and model parametrization). The first IAVCEI-WMO workshop on Ash Dispersal Forecast and Civil Aviation held in Geneva in October 2010 aimed at defining the needs of the tephra dispersal community with the objective to improve the numerical forecasting of volcanic clouds from a collaborative effort between researchers and operational institutions. The main recommendations and conclusions highlight the importance of dealing with uncertainties by producing ensemble forecasting combining TTDMs with observations (Bonadonna et al., 2012). These recommendations are still valid today for the definition of the new operational products supplied by the VAACs (Engwell et al., 2024). In this sense, between the end of 2024 and 2025, VAACs will start producing Quantitative Volcanic Ash information (QVA) in a progressive way for significant ash clouds, where significant indicates an ash cloud that poses a widespread impact on aircraft operations and air navigation (ICAO, 2021). QVA information will be a deterministic and probabilistic numerical ash concentration dispersion forecast based on the thresholds provided by the International Coordinating Council of Aerospace Industries Associations, from very high ( $>10 \text{ mg/m}^3$ ) to very low ( $<0.2 \text{ mg/m}^3$ ) concentrations.

The need to produce probabilistic operational forecasts highlights two important topics: the proper definition of the eruption source conditions (usually through Probability Density Functions) and the growing role of High-Performance Computing for volcanological applications.

When possible, field measurements and observational data (possibly indicating measurement uncertainty) should be used to define the main ESPs such as column height, MER, eruption duration and TGSD. Numerical modeling will likely benefit from the increasing observational capability of volcanic phenomena and advancing in measurement techniques of erupted products. Recent works show that numerical outcomes are greatly improved when observational data (with their uncertainties) are used to initialize and guide TTDM simulations for both hazard assessment and reconstruction of past events (Andronico et al., 2024; Dioguardi et al., 2020). To this end, research and operational institutions need to communicate efficiently to ensure that information on eruption dynamics is shared clearly and without ambiguity. Moreover, the increasing use of multi-sensor strategies, which combine data from various analyses and sensors, will likely contribute to improving the definition of the inputs required by TTDMs (and also plume models). For example, a better characterization of TGSD from analyses of tephra fall deposits, combined with satellite retrievals of ash cloud properties, will enhance our ability to simulate tephra dispersion and deposition (Freret-Lorgeril, Bonadonna, Corradini, et al., 2022; Poret et al., 2018). This is because the concentration of ash in the atmosphere is highly sensitive to the TGSD used to initialize the models, but TGSD is often highly uncertain, especially in real-time applications (Pardini et al., 2016; Scollo et al., 2008).

With present computational capabilities and data volumes entering the Exascale Era, scientists are becoming able to combine capability computing (i.e., higher resolution, increased degree of model sophistication, multi-scale, multi-physics) and capacity computing (multiple scenarios to deal with uncertainties, data assimilation, fusion of models and observations and hybrids thereof) into emerging products and services. For example, since 2018 the EuroHPC Center of Excellence for Exascale in Solid Earth (ChEESSE) is developing models, workflows, and services, with a particular focus on volcanology (Folch et al., 2023) that are paving the way for a number of future HPC-oriented applications, including:

- A comprehensive portfolio of probabilistic volcanic dispersal hazard maps quantifying the long-range hazard posed to aviation by multiple volcanoes, something not available yet. As an example, ChEESSE-2P (second

phase of ChEESA, 2023–2026) is exploring the impact on the main long-range air routes potentially caused by thousands of eruption scenarios originating from volcanoes across Europe, yielding the first integrated mapping accounting for multi-source at continental scale.

- As done in other application areas (e.g., urban-scale pollution), wind downscaling strategies are being adopted also for tephra dispersal modeling to capture local-scale effects and make current volcanic forecasts realistic below km-scale resolutions. This aspect is pivotal for a proper response during crises and prompt early-warning of proximal fallout and severe ash/gas pollution conditions expected in populated regions around volcanoes.
- Highly-resolved and accurate three-dimensional multiphase computational fluid dynamic plume simulations (e.g., Brogi et al., 2021). An emerging trend here is the multiscale simulation capability of phreatic eruptions (from sub-meter scale for the initial water flashing phase to kilometer scale for the flow and ballistic impacted area) and related urgent computing simulations to be used in the framework of a volcanic unrest and related longer-term hazard assessments.
- Ensemble-based approaches to optimally reconstruct the tephra fallout deposits from recent or even from ancient eruptions, for which the meteorological conditions are unknown (e.g., L. Mingari et al., 2023). This is relevant for quantifying and better constraining past eruption scenarios, and therefore improving our future hazard assessments, including those related to atmospheric concentration.
- The use of digital twins for volcanic systems and related impacts. Digital twins are virtual lifecycle environments that contain a data-informed replica of a real system, model-based prediction capabilities for future scenarios and, if possible and ideally (e.g., twins on industrial applications), the ability to provide feedback to modify the real system. Such environments are particularly tailored to assist in hazard assessment, territorial planning, early warning forecast, and urgent computing. For example, the Horizon Europe DT-GEO project (2022–2025, GA No. 101058129) is deploying a pre-operational prototype of digital twin on geophysical extremes addressing, in particular, specific hazardous phenomena from volcanoes (volcanic unrest, ash and gas dispersal, lava flows). The longer-term ambition of this project is the integration of volcano twin components in the Destination Earth initiative that is implementing a highly-accurate digital model of the Earth (Bauer et al., 2021).

Last but not least, the emerging potential of machine learning (and of artificial intelligence in general) in the detection and forecasting of tephra, yet limited to a few ash retrieval algorithms. On the other hand, the use of large synthetic data sets from TTDMs to train data-driven models is almost unexplored, despite the promising results obtained in other atmospheric dispersal applications (e.g., Mendil et al., 2022), when machine learning models are used in unseen conditions (i.e., not included in the training data set).

## Glossary

<i>Ash:</i>	solid fragments (tephra) produced during explosive eruptions with a diameter less than 2 mm. Fragments with a diameter of less than 63 $\mu\text{m}$ are typically referred to as fine ash.
<i>Detection:</i>	the ability for a sensor to measure a change in optical depth at the wavelength being measured.
<i>Discrimination:</i>	the ability to distinguish tephra from other features. For instance, it involves differentiating volcanic ash from other elements in a typical satellite scene (e.g., from a clear land/ocean surface, clouds, aerosols, and gasses).
<i>Explosive eruption:</i>	an eruption in which magma is fragmented into solid clasts by gas pressure before exiting from the vent.
<i>Magma:</i>	molten rock inside the earth consisting of three main components: silicate melt, solid crystals and gas bubbles.
<i>Mass Eruption Rate (MER):</i>	amount of material erupted from a volcano within a time unit, typically measured in kilograms per second (kg/s).

<i>Neutral buoyancy level:</i>	altitude at which the density of the plume is equal to the density of the atmosphere.
<i>Retrieval:</i>	is used to refer to the conversion of satellite-measured radiances to some physical property of the ash cloud/plume such as effective radius, optical depth and cloud-top height.
<i>Tephra:</i>	general term that refers to all fragmental material produced by a volcanic eruption. Tephra is classified into: blocks and bombs (>64 mm in diameter), lapilli (2–64 mm in diameter) and ash (<2 mm in diameter).
<i>Volcanic Explosivity Index (VEI):</i>	an eight-point scale (ranging from 0 to 8) used to measure the size of an explosive eruption based on factors such as magnitude (total mass or volume of material erupted), intensity (rate at which magma is discharged), and destructive power.
<i>Volcanic cloud:</i>	mass of volcanic particles and gasses that drifts downwind from a volcano due to atmospheric winds.
<i>Volcanic plume:</i>	hot mixture of volcanic particles, gasses and entrained atmospheric air form during explosive eruptions. A plume rises vertically in a volcanic column and then spreads horizontally forming the umbrella cloud.

### Acronyms

ABI:	Advanced Baseline Imager
ACC:	Area Control Center
AGRI:	Advanced Geostationary Radiation Imager
AHI:	Advanced Himawari Imager
AIRS:	Atmospheric Infrared Sounder
AMI:	Advanced Meteorological Imager
ATMS:	Advanced Technology Microwave Sounder
BT:	Brightness Temperature
BTD:	Brightness Temperature Difference
CALIOP:	Cloud-Aerosol Lidar with Orthogonal Polarization
CALIPSO:	Cloud-Aerosol Lidar and Infrared Pathfinder Satellite Observations
CMC:	Canadian Meteorological Centre
CrIS:	Cross-track Infrared Sounder
ESP:	Eruption Source Parameter
ECMWF:	European Centre for Medium-Range Weather Forecasts
FLEXPART:	FLEXible PARTicle dispersion model
FCI:	Flexible Combined Imager
GOES:	Geostationary Observing Environment Series
GMS:	Geostationary Meteorological Satellite
HYSPLIT:	Hybrid Single Particle Lagrangian Integrated Trajectory Model
HPC:	High-Performance Computing

IASI:	Infrared Atmospheric Sounding Interferometer
IAVW:	International Airways Volcano Watch
ICAO:	International Civil Aviation Organization
IMO:	Icelandic Meteorological Office
INGV:	Istituto Nazionale di Geofisica e Vulcanologia
JMA:	Japanese Meteorological Agency
MER:	Mass eruption rate
MIPAS:	Michelson Interferometer for Passive Atmospheric Sounding
MOCAGE:	Modèle de Chimie Atmosphérique à Grande Échelle
MODIS:	Moderate Resolution Imaging Spectroradiometer
MLDP0:	Modèle Lagrangien de Dispersion de Particules d'ordre zéro
MSD:	Microwave Spectral Difference
MWO:	Meteorological Watch Office
NAME:	Numerical Atmospheric-dispersion Modeling Environment
NCEP:	U.S. National Centers for Environmental Prediction
NILU:	Norwegian Climate and Environmental Research Institute
NOAA:	U.S. National Oceanic and Atmospheric Administration
OMI:	Ozone Monitoring Instrument
OMPS:	Ozone Mapping and Profiler Suite
SVO:	State Volcano Observatory
TOMS:	Total Ozone Mapping Spectrometer
TROPOMI:	TROPOspheric Monitoring Instrument
TTDM:	Tephra transport and dispersion model
USGS:	US Geological Survey
UVAI:	UV Aerosol Index
VAAC:	Volcanic Ash Advisory Center
VISSR:	Visible-Infrared Spin Scan Radiometer
VOLCAT:	VOLcanic Cloud Analysis Toolkit
VONA:	Volcano Observatory Notice for Aviation

### Data Availability Statement

All the data supporting figures extracted or adapted from published papers are available through the references cited in the captions. The dataset used to produce Figure 4d can be accessed from the IVESPA website [ivespa.co.uk](https://ivespa.co.uk) (Aubry et al., 2021). The simulations performed to produce Figures 15 and 17 were done using the FALL3D numerical model available at <https://zenodo.org/records/6343786> (Folch, Costa, et al., 2022), while the meteorological data is sourced from the Global Forecasting System 0.25° resolution produced by NCEP (NCEP, 2015) accessed on 01 October 2023. The result files of the FALL3D simulations shown in Figures 15 and 17, along with

the Python scripts used to generate the figures, can be found in the Zenodo repository at <https://zenodo.org/records/13316791> (Pardini et al., 2024).

### Acknowledgments

We thank Thomas Aubry, David Schneider, and the three anonymous referees for their insightful comments on the article. C. Bonadonna was supported by the Swiss National Science Foundation (Grant 200020\_204315). F. Pardini and M. de' Michieli Vitturi were supported by the INGV project Rete Multiparametrica (D.P. n.74/2020). Any use of trade, firm, or product names is for descriptive purposes only and does not imply endorsement by the U.S. Government. Open access publishing facilitated by Istituto Nazionale di Geofisica e Vulcanologia, as part of the Wiley - CRUI-CARE agreement.

### References

- Abdalati, W., Zwally, H. J., Bindschadler, R., Csatho, B., Farrell, S. L., Fricker, H. A., et al. (2010). The ICESat-2 laser altimetry mission. *Proceedings of the IEEE*, 98(5), 735–751. <https://doi.org/10.1109/JPROC.2009.2034765>
- Aizawa, K., Cimarelli, C., Alatorre-Ibargüengoitia, M. A., Yokoo, A., Dingwell, D. B., & Iguchi, M. (2016). Physical properties of volcanic lightning: Constraints from magnetotelluric and video observations at Sakurajima volcano, Japan. *Earth and Planetary Science Letters*, 444, 45–55. <https://doi.org/10.1016/j.epsl.2016.03.024>
- Alatorre-Ibargüengoitia, M. A., Scheu, B., & Dingwell, D. B. (2011). Influence of the fragmentation process on the dynamics of Vulcanian eruptions: An experimental approach. *Earth and Planetary Science Letters*, 302(1–2), 51–59. <https://doi.org/10.1016/j.epsl.2010.11.045>
- Alexander, D. (2013). Volcanic ash in the atmosphere and risks for civil aviation: A study in European crisis management. *International Journal of Disaster Risk Science*, 4(1), 9–19. <https://doi.org/10.1007/s13753-013-0003-0>
- Andronico, D., Cannata, A., Di Grazia, G., & Ferrari, F. (2021). The 1986–2021 paroxysmal episodes at the summit craters of Mt. Etna: Insights into volcano dynamics and hazard. *Earth-Science Reviews*, 220, 103686. <https://doi.org/10.1016/j.earscirev.2021.103686>
- Andronico, D., Del Bello, E., D'Oriano, C., Landi, P., Pardini, F., Scarlato, P., et al. (2021). Uncovering the eruptive patterns of the 2019 double paroxysm eruption crisis of Stromboli volcano. *Nature Communications*, 12(1), 4213. <https://doi.org/10.1038/s41467-021-24420-1>
- Andronico, D., D'Oriano, C., Pardini, F., La Spina, A., Vitturi, M. D. M., Bonfanti, P., et al. (2024). The 23–24 March 2021 lava fountain at Mt Etna, Italy. *Bulletin of Volcanology*, 86(6), 56. <https://doi.org/10.1007/s0044>
- Ansmann, A., Tesche, M., Groß, S., Freudenthaler, V., Seifert, P., Hiebsch, A., et al. (2010). The 16 April 2010 major volcanic ash plume over central Europe: EARLINET lidar and AERONET photometer observations at Leipzig and Munich, Germany. *Geophysical Research Letters*, 37(13), L13810. <https://doi.org/10.1029/2010GL043809>
- Arason, P., Petersen, G. N., & Björnsson, H. (2011). Observations of the altitude of the volcanic plume during the eruption of Eyjafjallajökull, April–May 2010. *Earth System Science Data*, 3(1), 9–17. <https://doi.org/10.5194/essd-3-9-2011>
- Arason, P., Petersen, G. N., & Björnsson, H. (2013). Estimation of eruption site location using volcanic lightning. In *Icelandic Met Office Vedustofar Islands Report*, 6. Retrieved from [https://en.vedur.is/media/vedurstofan/utgafa/skyrslur/2013/VI\\_2013\\_006.pdf](https://en.vedur.is/media/vedurstofan/utgafa/skyrslur/2013/VI_2013_006.pdf)
- Arastoopour, H., Wang, C. H., & Weil, S. A. (1982). Particle—Particle interaction force in a dilute gas—Solid system. *Chemical Engineering Science*, 37(9), 1379–1386. [https://doi.org/10.1016/0009-2509\(82\)85010-0](https://doi.org/10.1016/0009-2509(82)85010-0)
- Aravena, A., Carparelli, G., Cioni, R., Prestifilippo, M., & Scollo, S. (2023). Toward a real-time analysis of column height by visible cameras: An example from Mt. Etna, in Italy. *Remote Sensing*, 15(10), 2595. <https://doi.org/10.3390/rs15102595>
- Aravena, Á., Cioni, R., de' Michieli Vitturi, M., & Neri, A. (2018). Conduit stability effects on intensity and steadiness of explosive eruptions. *Scientific Reports*, 8(1), 4125. <https://doi.org/10.1038/s41598-018-22539-8>
- Armienti, P., Macedonio, G., & Pareschi, M. T. (1988). A numerical model for simulation of tephra transport and deposition: Applications to May 18, 1980, Mount St. Helens eruption. *Journal of Geophysical Research*, 93(B6), 6463–6476. <https://doi.org/10.1029/JB093iB06p06463>
- Aubry, T. J., Carazzo, G., & Jellinek, A. M. (2017). Turbulent entrainment into volcanic plumes: New constraints from laboratory experiments on buoyant jets rising in a stratified crossflow. *Geophysical Research Letters*, 44(20), 10198–10207. <https://doi.org/10.1002/2017GL075069>
- Aubry, T. J., Engwell, S., Bonadonna, C., Carazzo, G., Scollo, S., Van Eaton, A. R., et al. (2021). The independent volcanic eruption source parameter archive (IVESPA, version 1.0): A new observational database to support explosive eruptive column model validation and development. *Journal of Volcanology and Geothermal Research*, 417, 107295. <https://doi.org/10.1016/j.jvolgeores.2021.107295>
- Aubry, T. J., Engwell, S. L., Bonadonna, C., Mastin, L. G., Carazzo, G., Van Eaton, A. R., et al. (2023). New insights into the relationship between mass eruption rate and volcanic column height based on the IVESPA data set. *Geophysical Research Letters*, 50(14), e2022GL102633. <https://doi.org/10.1029/2022GL102633>
- Aubry, T. J., Farquharson, J. I., Rowell, C. R., Watt, S. F., Pinel, V., Beckett, F., et al. (2022). Impact of climate change on volcanic processes: Current understanding and future challenges. *Bulletin of Volcanology*, 84(6), 58. <https://doi.org/10.1007/s00445-022-01562-8>
- Ayris, P. M., & Delmelle, P. (2012). The immediate environmental effects of tephra emission. *Bulletin of Volcanology*, 74(9), 1905–1936. <https://doi.org/10.1007/s00445-012-0654-5>
- Bagheri, G., & Bonadonna, C. (2016). Aerodynamics of volcanic particles: Characterization of size, shape, and settling velocity. In *Volcanic ash* (pp. 39–52). Elsevier. <https://doi.org/10.1016/B978-0-08-100405-0.00005-7>
- Bagheri, G., Rossi, E., Biass, S., & Bonadonna, C. (2016). Timing and nature of volcanic particle clusters based on field and numerical investigations. *Journal of Volcanology and Geothermal Research*, 327, 520–530. <https://doi.org/10.1016/j.jvolgeores.2016.09.009>
- Bai, L., Liu, C., Ji, Y., & Zhu, W. (2023). Infrasound waves and sulfur dioxide emissions caused by the 2022 Hunga volcanic eruption, Tonga. *Frontiers in Earth Science*, 11, 1144496. <https://doi.org/10.3389/feart.2023.1144496>
- Baines, P. G., & Sparks, R. S. J. (2005). Dynamics of giant volcanic ash clouds from supervolcanic eruptions. *Geophysical Research Letters*, 32(24). <https://doi.org/10.1029/2005GL024597>
- Baissac, D. M., Nicora, M. G., Bali, L. J., Badi, G. A., & Ávila, E. E. (2021). Volcanic alert system by lightning detection using the WWLLN-ash cloud monitor. *Journal of South American Earth Sciences*, 108, 103234. <https://doi.org/10.1016/j.jsames.2021.103234>
- Balangué-Tarriela, M. I. R., Lagmay, A. M. F., Sarmiento, D. M., Vasquez, J., Baldago, M. C., Ybañez, R., et al. (2022). Analysis of the 2020 Taal Volcano tephra fall deposits from crowdsourced information and field data. *Bulletin of Volcanology*, 84(3), 35. <https://doi.org/10.1007/s00445-022-01534-y>
- Ball, J. G. C., Reed, B. E., Grainger, R. G., Peters, D. M., Mather, T. A., & Pyle, D. M. (2015). Measurements of the complex refractive index of volcanic ash at 450, 546.7, and 650 nm. *Journal of Geophysical Research: Atmospheres*, 120(15), 7747–7757. <https://doi.org/10.1002/2015JD023521>
- Bamber, E. C., Arzilli, F., Polacci, M., Hartley, M. E., Fellowes, J., Di Genova, D., et al. (2020). Pre- and syn-eruptive conditions of a basaltic plinian eruption at Masaya volcano, Nicaragua: The Masaya Triple layer (2.1 ka). *Journal of Volcanology and Geothermal Research*, 392, 106761. <https://doi.org/10.1016/j.jvolgeores.2019.106761>
- Barnie, T., Hjörvar, T., Titos, M., Sigurðsson, E. M., Pálsson, S. K., Bergsson, B., et al. (2023). Volcanic plume height monitoring using calibrated web cameras at the Icelandic meteorological Office: System overview and first application during the 2021 Fagradalsfjall eruption. *Journal of Applied Volcanology*, 12(1), 4. <https://doi.org/10.1186/s13617-023-00130-9>

- Barone, B., Letelier, R. M., Rubin, K. H., & Karl, D. M. (2022). Satellite detection of a massive phytoplankton bloom following the 2022 submarine eruption of the Hunga Tonga-Hunga Ha'apai Volcano. *Geophysical Research Letters*, *49*(17), e2022GL099293. <https://doi.org/10.1029/2022GL099293>
- Barsotti, S., Di Rienzo, D. I., Thordarson, T., Björnsson, B. B., & Karlsdóttir, S. (2018). Assessing impact to infrastructures due to tephra fallout from Öræfajökull volcano (Iceland) by using a scenario-based approach and a numerical model. *Frontiers in Earth Science*, *6*, 196. <https://doi.org/10.3389/feart.2018.00196>
- Barsotti, S., Neri, A., & Scire, J. S. (2008). The VOL-CALPUFF model for atmospheric ash dispersal: 1. Approach and physical formulation. *Journal of Geophysical Research*, *113*(B3), 3208. <https://doi.org/10.1029/2006JB004623>
- Barsotti, S., Parks, M. M., Pfeffer, M. A., Óladóttir, B. A., Barnie, T., Titos, M. M., et al. (2023). The eruption in Fagradalsfjall (2021, Iceland): How the operational monitoring and the volcanic hazard assessment contributed to its safe access. *Natural Hazards*, *116*(3), 3063–3092. <https://doi.org/10.1007/s11069-022-05798-7>
- Barsotti, S., Scollo, S., Macedonio, G., Felpeto, A., Peltier, A., Vougioukalakis, G., et al. (2024). The European Volcano Observatories and their use of the aviation colour code system. *Bulletin of Volcanology*, *86*(3), 23. <https://doi.org/10.1007/s00445-024-01712-0>
- Barton, I. J., & Takashima, T. (1986). An AVHRR investigation of surface emissivity near Lake Eyre, Australia. *Remote Sensing of Environment*, *20*(2), 153–163. [https://doi.org/10.1016/0034-4257\(86\)90020-9](https://doi.org/10.1016/0034-4257(86)90020-9)
- Bauer, P., Stevens, B., & Hazeleger, W. (2021). A digital twin of Earth for the green transition. *Nature Climate Change*, *11*(2), 80–83. <https://doi.org/10.1038/s41558-021-00986-y>
- Baxter, P. J., Ing, R., Falk, H., & Plikaytis, B. (1983). Mount St. Helens eruptions: The acute respiratory effects of volcanic ash in a North American community. *Archives of Environmental Health: An International Journal*, *38*(3), 138–143. <https://doi.org/10.1080/00039896.1983.10543994>
- Bebbington, M., Cronin, S. J., Chapman, I., & Turner, M. B. (2008). Quantifying volcanic ash fall hazard to electricity infrastructure. *Journal of Volcanology and Geothermal Research*, *177*(4), 1055–1062. <https://doi.org/10.1016/j.jvolgeores.2008.07.023>
- Bebbington, M. S., Stirling, M. W., Cronin, S., Wang, T., & Jolly, G. (2018). National-level long-term eruption forecasts by expert elicitation. *Bulletin of Volcanology*, *80*(6), 1–22. <https://doi.org/10.1007/s00445-018-1230-4>
- Beckett, F., Rossi, E., Devenish, B., Witham, C., & Bonadonna, C. (2022). Modelling the size distribution of aggregated volcanic ash and implications for operational atmospheric dispersion modelling. *Atmospheric Chemistry and Physics*, *22*(5), 3409–3431. <https://doi.org/10.5194/acp-22-3409-2022>
- Beckett, F. M., Bensimon, D., Crawford, A., Deslandes, M., Guidard, V., Hort, M. C., et al. (2024). VAAC model setup Tables 2023. *Zenodo*. <https://doi.org/10.5281/zenodo.10671098>
- Beckett, F. M., Witham, C. S., Leadbetter, S. J., Crocker, R., Webster, H. N., Hort, M. C., et al. (2020). Atmospheric dispersion modelling at the London VAAC: A review of developments since the 2010 Eyjafjallajökull volcano ash cloud. *Atmosphere*, *11*(4), 352. <https://doi.org/10.3390/atmos11040352>
- Bedoya-Velásquez, A. E., Hoyos-Restrepo, M., Barreto, A., García, R. D., Romero-Campos, P. M., García, O., et al. (2022). Estimation of the mass concentration of volcanic ash using ceilometers: Study of fresh and transported plumes from La Palma volcano. *Remote Sensing*, *14*(22), 5680. <https://doi.org/10.3390/rs14225680>
- Behnke, S. A., Thomas, R. J., Edens, H. E., Krehbiel, P. R., & Rison, W. (2014). The 2010 eruption of Eyjafjallajökull: Lightning and plume charge structure. *Journal of Geophysical Research: Atmospheres*, *119*(2), 833–859. <https://doi.org/10.1002/2013JD020781>
- Behnke, S. A., Thomas, R. J., McNutt, S. R., Schneider, D. J., Krehbiel, P. R., Rison, W., & Edens, H. E. (2013). Observations of volcanic lightning during the 2009 eruption of Redoubt Volcano. *Journal of Volcanology and Geothermal Research*, *259*, 214–234. <https://doi.org/10.1016/j.jvolgeores.2011.12.010>
- Bennett, F. D. (1971). Vaporization waves in explosive volcanism. *Nature*, *234*(5331), 538–539. <https://doi.org/10.1038/234538a0>
- Biass, S., Scaini, C., Bonadonna, C., Folch, A., Smith, K., & Höskuldsson, A. (2014). A multi-scale risk assessment for tephra fallout and airborne concentration from multiple Icelandic volcanoes—Part 1: Hazard assessment. *Natural Hazards and Earth System Sciences*, *14*(8), 2265–2287. <https://doi.org/10.5194/nhess-14-2265-2014>
- Biggs, J., Ayele, A., Fischer, T. P., Fontijn, K., Hutchison, W., Kazimoto, E., et al. (2021). Volcanic activity and hazard in the east African Rift zone. *Nature Communications*, *12*(1), 6881. <https://doi.org/10.1038/s41467-021-27166-y>
- Black, B. A., Lamarque, J. F., Marsh, D. R., Schmidt, A., & Bardeen, C. G. (2021). Global climate disruption and regional climate shelters after the Toba supereruption. *Proceedings of the National Academy of Sciences*, *118*(29), e2013046118. <https://doi.org/10.1073/pnas.2013046118>
- Blackburn, E. A., Wilson, L., & Sparks, R. J. (1976). Mechanisms and dynamics of strombolian activity. *Journal of the Geological Society*, *132*(4), 429–440. <https://doi.org/10.1144/gsjgs.132.4.0429>
- Bombrun, M., Jessop, D., Harris, A., & Barra, V. (2018). An algorithm for the detection and characterisation of volcanic plumes using thermal camera imagery. *Journal of Volcanology and Geothermal Research*, *352*, 26–37. <https://doi.org/10.1016/j.jvolgeores.2018.01.006>
- Bonadonna, C. (2006). Probabilistic modelling of tephra dispersion. In H. M. Mader, S. G. Coles, C. B. Connor, & L. J. Connor (Eds.), *Statistics in volcanology* (pp. 243–259). The Geological Society. <https://doi.org/10.1144/IAVCEI001.19>
- Bonadonna, C., Biass, S., Menoni, S., & Gregg, C. E. (2021). Assessment of risk associated with tephra-related hazards. In *Forecasting and planning for volcanic hazards, risks, and disasters* (pp. 329–378). Elsevier. <https://doi.org/10.1016/B978-0-12-818082-2.00008-1>
- Bonadonna, C., Cioni, R., Pistolesi, M., Elissondo, M., & Baumann, V. (2015). Sedimentation of long-lasting wind-affected volcanic plumes: The example of the 2011 rhyolitic Cordón Caulle eruption, Chile. *Bulletin of Volcanology*, *77*(2), 1–19. <https://doi.org/10.1007/s00445-015-0900-8>
- Bonadonna, C., Connor, C. B., Houghton, B. F., Connor, L., Byrne, M., Laing, A., & Hincks, T. K. (2005). Probabilistic modeling of tephra dispersal: Hazard assessment of a multiphase rhyolitic eruption at Tarawera, New Zealand. *Journal of Geophysical Research*, *110*(B3), B03203. <https://doi.org/10.1029/2003JB002896>
- Bonadonna, C., Folch, A., Loughlin, S., & Puempel, H. (2012). Future developments in modelling and monitoring of volcanic ash clouds: Outcomes from the first IAVCEI-WMO workshop on ash dispersal forecast and civil aviation. *Bulletin of Volcanology*, *74*, 1–10. <https://doi.org/10.1007/s00445-011-0508-6>
- Bonadonna, C., Genco, R., Gouhier, M., Pistolesi, M., Cioni, R., Alfano, F., et al. (2011). Tephra sedimentation during the 2010 Eyjafjallajökull eruption (Iceland) from deposit, radar, and satellite observations. *Journal of Geophysical Research*, *116*(B12), B12202. <https://doi.org/10.1029/2011JB008462>
- Bonadonna, C., & Houghton, B. F. (2005). Total grain-size distribution and volume of tephra-fall deposits. *Bulletin of Volcanology*, *67*(5), 441–456. <https://doi.org/10.1007/s00445-004-0386-2>
- Bonadonna, C., Macedonio, G., & Sparks, R. S. J. (2002). Numerical modelling of tephra fallout associated with dome collapses and vulcanian explosions: Application to hazard assessment on Montserrat. *Geological Society, London, Memoirs*, *21*(1), 517–537. <https://doi.org/10.1144/GSL.MEM.2002.021.01.23>

- Bonadonna, C., & Phillips, J. C. (2003). Sedimentation from strong volcanic plumes. *Journal of Geophysical Research*, *108*(B7), 2340. <https://doi.org/10.1029/2002JB002034>
- Bonadonna, C., Phillips, J. C., & Houghton, B. F. (2005). Modeling tephra sedimentation from a Ruapehu weak plume eruption. *Journal of Geophysical Research*, *110*(B8), B08209. <https://doi.org/10.1029/2004JB003515>
- Bonasia, R., Scaini, C., Capra, L., Nathenson, M., Siebe, C., Arana-Salinas, L., & Folch, A. (2014). Long-range hazard assessment of volcanic ash dispersal for a Plinian eruptive scenario at Popocatepetl volcano (Mexico): Implications for civil aviation safety. *Bulletin of Volcanology*, *76*, 1–16. <https://doi.org/10.1007/s00445-013-0789-z>
- Boselli, A., Scollo, S., Leto, G., Sanchez, R. Z., Sannino, A., Wang, X., et al. (2018). First volcanic plume measurements by an elastic/Raman Lidar close to the Etna summit craters. *Frontiers in Earth Science*, *6*, 125. <https://doi.org/10.3389/feart.2018.00125>
- Broggi, F., Amati, G., Boga, G., Castellano, M., Gracia, J., Esposti Ongaro, T., & Cerminara, M. (2021). Optimization strategies for efficient high-resolution volcanic plume simulations with OpenFOAM. In *EGU general assembly conference abstracts (EGU21-15310)*. <https://doi.org/10.5194/egusphere-egu21-15310>
- Brown, R. J., Bonadonna, C., & Durant, A. J. (2012). A review of volcanic ash aggregation. *Physics and Chemistry of the Earth, Parts A/B/C*, *45*, 65–78. <https://doi.org/10.1016/j.pce.2011.11.001>
- Bugliaro, L., Piontek, D., Kox, S., Schmidl, M., Mayer, B., Müller, R., et al. (2022). VADUGS: A neural network for the remote sensing of volcanic ash with MSG/SEVIRI trained with synthetic thermal satellite observations simulated with a radiative transfer model. *Natural Hazards and Earth System Sciences*, *22*(3), 1029–1054. <https://doi.org/10.5194/nhess-22-1029-2022>
- Burgers, G., Van Leeuwen, P. J., & Evensen, G. (1998). Analysis scheme in the ensemble Kalman filter. *Monthly Weather Review*, *126*(6), 1719–1724. [https://doi.org/10.1175/1520-0493\(1998\)126<1719:ASITEK>2.0.CO;2](https://doi.org/10.1175/1520-0493(1998)126<1719:ASITEK>2.0.CO;2)
- Burns, F. A., Bonadonna, C., Pioli, L., Cole, P. D., & Stinton, A. (2017). Ash aggregation during the 11 February 2010 partial dome collapse of the Soufriere Hills volcano, Montserrat. *Journal of Volcanology and Geothermal Research*, *335*, 92–112. <https://doi.org/10.1016/j.jvolgeores.2017.01.024>
- Bursik, M. (2001). Effect of wind on the rise height of volcanic plumes. *Geophysical Research Letters*, *28*(18), 3621–3624. <https://doi.org/10.1029/2001GL013393>
- Bursik, M., Jones, M., Carn, S., Dean, K., Patra, A., Pavolonis, M., et al. (2012). Estimation and propagation of volcanic source parameter uncertainty in an ash transport and dispersal model: Application to the Eyjafjallajökull plume of 14–16 April 2010. *Bulletin of Volcanology*, *74*(10), 2321–2338. <https://doi.org/10.1007/s00445-012-0665-2>
- Burton, M. (2016). Quantitative ground-based imaging of volcanic ash. In *Volcanic ash* (pp. 175–185). Elsevier. <https://doi.org/10.1016/B978-0-08-100405-0.00015-X>
- Butwin, M. K., Pfeffer, M. A., von Löwis, S., Støren, E. W., Bali, E., & Thorsteinsson, T. (2020). Properties of dust source material and volcanic ash in Iceland. *Sedimentology*, *67*(6), 3067–3087. <https://doi.org/10.1111/sed.12734>
- Cahalan, R. C., Mastin, L. G., Van Eaton, A. R., Hurwitz, S., Smith, A. B., Dufek, J., et al. (2023). Dynamics of the December 2020 ash-poor plume formed by lava-water interaction at the summit of Kilauea volcano, Hawai'i. *Geochemistry, Geophysics, Geosystems*, *24*(3), e2022GC010718. <https://doi.org/10.1029/2022GC010718>
- Campus, P. (2006). Monitoring volcanic eruptions with the IMS infrasound network. *Inframatrics*, *15*, 6–12.
- Cannata, A., Montalto, P., Aliotta, M., Cassisi, C., Pulvirenti, A., Privitera, E., & Patané, D. (2011). Clustering and classification of infrasonic events at Mount Etna using pattern recognition techniques. *Geophysical Journal International*, *185*(1), 253–264. <https://doi.org/10.1111/j.1365-246X.2011.04951.x>
- Cao, Z., Bursik, M., Yang, Q., & Patra, A. (2021). Simulating the transport and dispersal of volcanic ash clouds with initial conditions created by a 3D plume model. *Frontiers in Earth Science*, *9*, 704797. <https://doi.org/10.3389/feart.2021.704797>
- Caplan-Auerbach, J., Bellesiles, A., & Fernandes, J. K. (2010). Estimates of eruption velocity and plume height from infrasonic recordings of the 2006 eruption of Augustine Volcano, Alaska. *Journal of Volcanology and Geothermal Research*, *189*(1–2), 12–18. <https://doi.org/10.1016/j.jvolgeores.2009.10.002>
- Capponi, A., Harvey, N. J., Dacre, H. F., Beven, K., Saint, C., Wells, C., & James, M. R. (2022). Refining an ensemble of volcanic ash forecasts using satellite retrievals: Raikoke 2019. *Atmospheric Chemistry and Physics*, *22*(9), 6115–6134. <https://doi.org/10.5194/acp-22-6115-2022>
- Carazzo, G., & Jellinek, A. M. (2012). A new view of the dynamics, stability and longevity of volcanic clouds. *Earth and Planetary Science Letters*, *325*, 39–51. <https://doi.org/10.1016/j.epsl.2012.01.025>
- Carazzo, G., & Jellinek, A. M. (2013). Particle sedimentation and diffusive convection in volcanic ash-clouds. *Journal of Geophysical Research: Solid Earth*, *118*(4), 1420–1437. <https://doi.org/10.1002/jgrb.50155>
- Carey, S., & Sigurdsson, H. (1986). The 1982 eruptions of El Chichón volcano, Mexico (2): Observations and numerical modelling of tephra-fall distribution. *Bulletin of Volcanology*, *48*(2–3), 127–141. <https://doi.org/10.1007/BF01046547>
- Carey, S., & Sparks, R. S. J. (1986). Quantitative models of the fallout and dispersal of tephra from volcanic eruption columns. *Bulletin of Volcanology*, *48*(2–3), 109–125. <https://doi.org/10.1007/BF01046546>
- Carlsen, H. K., Ilyinskaya, E., Baxter, P. J., Schmidt, A., Thorsteinsson, T., Pfeffer, M. A., et al. (2021). Increased respiratory morbidity associated with exposure to a mature volcanic plume from a large Icelandic fissure eruption. *Nature Communications*, *12*(1), 2161. <https://doi.org/10.1038/s41467-02>
- Carn, S. A., & Krotkov, N. A. (2016). Ultraviolet satellite measurements of volcanic ash. In *Volcanic ash* (pp. 217–231). Elsevier. <https://doi.org/10.1016/B978-0-08-100405-0.00018-5>
- Carn, S. A., Krotkov, N. A., Fisher, B. L., Li, C., & Prata, A. J. (2018). First observations of volcanic eruption clouds from the L1 Earth-Sun Lagrange point by DSCOVR/EPIC. *Geophysical Research Letters*, *45*(20), 11–456. <https://doi.org/10.1029/2018GL079808>
- Carn, S. A., Krueger, A. J., Krotkov, N. A., Yang, K., & Evans, K. (2009). Tracking volcanic sulfur dioxide clouds for aviation hazard mitigation. *Natural Hazards*, *51*(2), 325–343. <https://doi.org/10.1007/s11069-008-9228-4>
- Carr, J. L., Horváth, Á., Wu, D. L., & Friberg, M. D. (2022). Stereo plume height and motion retrievals for the record-setting Hunga Tonga-Hunga Ha'apai eruption of 15 January 2022. *Geophysical Research Letters*, *49*(9), e2022GL098131. <https://doi.org/10.1029/2022GL098131>
- Carrasi, A., Bocquet, M., Bertino, L., & Evensen, G. (2018). Data assimilation in the geosciences: An overview of methods, issues, and perspectives. *Wiley Interdisciplinary Reviews: Climate Change*, *9*(5), e535. <https://doi.org/10.1002/wcc.535>
- Cashman, K. V., & Scheu, B. (2015). Magmatic fragmentation. In *The encyclopedia of volcanoes* (pp. 459–471). Academic Press. <https://doi.org/10.1016/B978-0-12-385938-9.00025-0>
- Cashman, K. V., & Taggart, J. E. (1983). Petrologic monitoring of 1981 and 1982 eruptive products from Mount St. Helens. *Science*, *221*(4618), 1385–1387. <https://doi.org/10.1126/science.221.4618.1385>

- Castaño, L. M., Ospina, C. A., Cadena, O. E., Galvis-Arenas, B., Londono, J. M., Laverde, C. A., et al. (2020). Continuous monitoring of the 2015–2018 Nevado del Ruiz activity, Colombia, using satellite infrared images and local infrasound records. *Earth Planets and Space*, 72, 1–18. <https://doi.org/10.1186/s40623-020-01197-z>
- Cerminara, M., Ongaro, T. E., Valade, S., & Harris, A. J. (2015). Volcanic plume vent conditions retrieved from infrared images: A forward and inverse modeling approach. *Journal of Volcanology and Geothermal Research*, 300, 129–147. <https://doi.org/10.1016/j.jvolgeores.2014.12.015>
- Chahine, M. T., Pagano, T. S., Aumann, H. H., Atlas, R., Barnet, C., Blaisdell, J., et al. (2006). AIRS: Improving weather forecasting and providing new data on greenhouse gases. *Bulletin of the American Meteorological Society*, 87(7), 911–926. <https://doi.org/10.1175/BAMS-87-7-911>
- Chai, T., Crawford, A., Stunder, B., Pavolonis, M. J., Draxler, R., & Stein, A. (2017). Improving volcanic ash predictions with the HYSPLIT dispersion model by assimilating MODIS satellite retrievals. *Atmospheric Chemistry and Physics*, 17(4), 2865–2879. <https://doi.org/10.5194/acp-17-2865-2017>
- Chazette, P., Bocquet, M., Royer, P., Winiarek, V., Raut, J. C., Labazuy, P., et al. (2012). Eyjafjallajökull ash concentrations derived from both lidar and modeling. *Journal of Geophysical Research*, 117(D20), D00U14. <https://doi.org/10.1029/2011JD015755>
- Cimarelli, C., Alatorre-Ibargüengoitia, M. A., Aizawa, K., Yokoo, A., Díaz-Marina, A., Iguchi, M., & Dingwell, D. B. (2016). Multiparametric observation of volcanic lightning: Sakurajima Volcano, Japan. *Geophysical Research Letters*, 43(9), 4221–4228. <https://doi.org/10.1002/2015GL067445>
- Cimarelli, C., & Genareau, K. (2022). A review of volcanic electrification of the atmosphere and volcanic lightning. *Journal of Volcanology and Geothermal Research*, 422, 107449. <https://doi.org/10.1016/j.jvolgeores.2021.107449>
- Clarisse, L., Coheur, P. F., Prata, F., Hadji-Lazaro, J., Hurtmans, D., & Clerbaux, C. (2013). A unified approach to infrared aerosol remote sensing and type specification. *Atmospheric Chemistry and Physics*, 13(4), 2195–2221. <https://doi.org/10.5194/acp-13-2195-2013>
- Clarisse, L., Hurtmans, D., Prata, A. J., Karagulian, F., Clerbaux, C., De Mazière, M., & Coheur, P. F. (2010). Retrieving radius, concentration, optical depth, and mass of different types of aerosols from high-resolution infrared nadir spectra. *Applied Optics*, 49(19), 3713–3722. <https://doi.org/10.1364/AO.49.003713>
- Clarisse, L., & Prata, F. (2016). Infrared sounding of volcanic ash. In *Volcanic ash* (pp. 189–215). Elsevier. <https://doi.org/10.1016/B978-0-08-100405-0.00017-3>
- Clerbaux, C., Boynard, A., Clarisse, L., George, M., Hadji-Lazaro, J., Herbin, H., et al. (2009). Monitoring of atmospheric composition using the thermal infrared IASI/MetOp sounder. *Atmospheric Chemistry and Physics*, 9(16), 6041–6054. <https://doi.org/10.5194/acp-9-6041-2009>
- Clift, R., & Gauvin, W. H. (1971). Motion of entrained particles in gas streams. *Canadian Journal of Chemical Engineering*, 49(4), 439–448. <https://doi.org/10.1002/cjce.5450490403>
- Collini, E., Osorio, M. S., Folch, A., Viramonte, J. G., Villarosa, G., & Salmuni, G. (2013). Volcanic ash forecast during the June 2011 Cordón Caulle eruption. *Natural Hazards*, 66(2), 389–412. <https://doi.org/10.1007/s11069-012-0492-y>
- Constantine, E. K., Bluth, G. J. S., & Rose, W. I. (2000). TOMS and AVHRR observations of drifting volcanic clouds from the August 1991 eruptions of Cerro Hudson. In P. J. Mouginiis-Mark, J. A. Crisp, & J. H. Fink (Eds.), *Geophysical monograph series* (Vol. 116, pp. 45–64). American Geophysical Union. <https://doi.org/10.1029/GM116p0045>
- Constantinescu, R., White, J. T., Connor, C., Cole, P., Fontijn, K., Barclay, J., & Robertson, R. (2024). Estimation of eruption source parameters for the 2021 La Soufrière eruption (St Vincent): Implications for quantification of eruption magnitude on volcanic islands. *Geological Society, London, Special Publications*, 539(1), 107–120. <https://doi.org/10.1144/SP539-2023-38>
- Coombs, M. L., Wech, A. G., Haney, M. M., Lyons, J. J., Schneider, D. J., Schwaiger, H. F., et al. (2018). Short-term forecasting and detection of explosions during the 2016–2017 eruption of Bogoslov volcano, Alaska. *Frontiers in Earth Science*, 6, 122. <https://doi.org/10.3389/feart.2018.00122>
- Cornell, W., Carey, S., & Sigurdsson, H. (1983). Computer simulation of transport and deposition of the Campanian Y-5 ash. *Journal of Volcanology and Geothermal Research*, 17(1–4), 89–109. [https://doi.org/10.1016/0377-0273\(83\)90063-X](https://doi.org/10.1016/0377-0273(83)90063-X)
- Corradini, S., Merucci, L., & Folch, A. (2010). Volcanic ash cloud properties: Comparison between MODIS satellite retrievals and FALL3D transport model. *IEEE Geoscience and Remote Sensing Letters*, 8(2), 248–252. <https://doi.org/10.1109/LGRS.2010.2064156>
- Corradini, S., Montopoli, M., Guerrieri, L., Ricci, M., Scollo, S., Merucci, L., et al. (2016). A multi-sensor approach for volcanic ash cloud retrieval and eruption characterization: The 23 November 2013 Etna lava fountain. *Remote Sensing*, 8(1), 58. <https://doi.org/10.3390/rs8010058>
- Corradini, S., Spinetti, C., Carboni, E., Tirelli, C., Buongiorno, M. F., Pugnaghi, S., & Gangale, G. (2008). Mt. Etna tropospheric ash retrieval and sensitivity analysis using Moderate Resolution Imaging Spectroradiometer measurements. *Journal of Applied Remote Sensing*, 2(1), 023550. <https://doi.org/10.1117/1.3046674>
- Corradino, C., Ganci, G., Cappello, A., Bilotta, G., Calvari, S., & Del Negro, C. (2020). Recognizing eruptions of Mount Etna through machine learning using multiperspective infrared images. *Remote Sensing*, 12(6), 970. <https://doi.org/10.3390/rs12060970>
- Costa, A., Folch, A., & Macedonio, G. (2010). A model for wet aggregation of ash particles in volcanic plumes and clouds: 1. Theoretical formulation. *Journal of Geophysical Research*, 115(B9), B09201. <https://doi.org/10.1029/2009JB007175>
- Costa, A., Folch, A., & Macedonio, G. (2013). Density-driven transport in the umbrella region of volcanic clouds: Implications for tephra dispersion models. *Geophysical Research Letters*, 40(18), 4823–4827. <https://doi.org/10.1002/grl.50942>
- Costa, A., Pioli, L., & Bonadonna, C. (2016). Assessing tephra total grain-size distribution: Insights from field data analysis. *Earth and Planetary Science Letters*, 443, 90–107. <https://doi.org/10.1016/j.epsl.2016.02.040>
- Costa, A., Suzuki, Y. J., Cerminara, M., Devenish, B. J., Ongaro, T. E., Herzog, M., et al. (2016). Results of the eruptive column model inter-comparison study. *Journal of Volcanology and Geothermal Research*, 326, 2–25. <https://doi.org/10.1016/j.jvolgeores.2016.01.017>
- Craig, H., Wilson, T., Stewart, C., Outes, V., Villarosa, G., & Baxter, P. (2016). Impacts to agriculture and critical infrastructure in Argentina after ashfall from the 2011 eruption of the Cordón Caulle volcanic complex: An assessment of published damage and function thresholds. *Journal of Applied Volcanology*, 5, 1–31. <https://doi.org/10.1186/s13617-016-0046-1>
- Crawford, A. (2020). The use of Gaussian mixture models with atmospheric Lagrangian particle dispersion models for density estimation and feature identification. *Atmosphere*, 11(12), 1369. <https://doi.org/10.3390/atmos11121369>
- Crawford, A. M., Stunder, B. J., Ngan, F., & Pavolonis, M. J. (2016). Initializing HYSPLIT with satellite observations of volcanic ash: A case study of the 2008 Kasatochi eruption. *Journal of Geophysical Research: Atmospheres*, 121(18), 10–786. <https://doi.org/10.1002/2016JD024779>
- Crevoisier, C., Clerbaux, C., Guidard, V., Phulpin, T., Armante, R., Barret, B., et al. (2014). Towards IASI-New Generation (IASI-NG): Impact of improved spectral resolution and radiometric noise on the retrieval of thermodynamic, chemistry and climate variables. *Atmospheric Measurement Techniques*, 7(12), 4367–4385. <https://doi.org/10.5194/amt-7-4367-2014>

- Cronin, S. J., Hedley, M. J., Neall, V. E., & Smith, R. G. (1998). Agronomic impact of tephra fallout from the 1995 and 1996 Ruapehu Volcano eruptions, New Zealand. *Environmental Geology*, *34*(1), 21–30. <https://doi.org/10.1007/s002540050253>
- Dacre, H. F., Grant, A. L., & Johnson, B. T. (2013). Aircraft observations and model simulations of concentration and particle size distribution in the Eyjafjallajökull volcanic ash cloud. *Atmospheric Chemistry and Physics*, *13*(3), 1277–1291. <https://doi.org/10.5194/acp-13-1277-2013>
- Dacre, H. F., Harvey, N. J., Webley, P. W., & Morton, D. (2016). How accurate are volcanic ash simulations of the 2010 Eyjafjallajökull eruption? *Journal of Geophysical Research: Atmospheres*, *121*(7), 3534–3547. <https://doi.org/10.1002/2015JD024265>
- Dalal, P., Kundu, B., Panda, J., & Jin, S. (2023). Atmospheric Lamb wave pulse and volcanic explosivity index following the 2022 Hunga Tonga (South Pacific) eruption. *Frontiers in Earth Science*, *10*, 931545. <https://doi.org/10.3389/feart.2022.931545>
- D'Amours, R., Malo, A., Flesch, T., Wilson, J., Gauthier, J. P., & Servranckx, R. (2015). The Canadian Meteorological Centre's atmospheric transport and dispersion modelling suite. *Atmosphere-Ocean*, *53*(2), 176–199. <https://doi.org/10.1080/07055900.2014.1000260>
- D'Amours, R., Malo, A., Servranckx, R., Bensimon, D., Trudel, S., & Gauthier-Bilodeau, J. P. (2010). Application of the atmospheric Lagrangian particle dispersion model MLDPO to the 2008 eruptions of Okmok and Kasatochi volcanoes. *Journal of Geophysical Research*, *115*(D2), D00L11. <https://doi.org/10.1029/2009JD013602>
- Dare, R. A., Potts, R. J., & Wain, A. G. (2016). Modelling wet deposition in simulations of volcanic ash dispersion from hypothetical eruptions of Merapi, Indonesia. *Atmospheric Environment*, *143*, 190–201. <https://doi.org/10.1016/j.atmosenv.2016.08.022>
- Dare, R. A., Smith, D. H., & Naughton, M. J. (2016). Ensemble prediction of the dispersion of volcanic ash from the 13 February 2014 eruption of Kelut, Indonesia. *Journal of Applied Meteorology and Climatology*, *55*(1), 61–78. <https://doi.org/10.1175/JAMC-D-15-0079.1>
- Dean, K., Bowling, S. A., Shaw, G., & Tanaka, H. (1994). Satellite analyses of movement and characteristics of the Redoubt Volcano plume, January 8, 1990. *Journal of Volcanology and Geothermal Research*, *62*(1–4), 339–352. [https://doi.org/10.1016/0377-0273\(94\)90040-X](https://doi.org/10.1016/0377-0273(94)90040-X)
- De Angelis, S., Diaz-Moreno, A., & Zuccarello, L. (2019). Recent developments and applications of acoustic infrasound to monitor volcanic emissions. *Remote Sensing*, *11*(11), 1302. <https://doi.org/10.3390/rs11111302>
- De Angelis, S., Fee, D., Haney, M., & Schneider, D. (2012). Detecting hidden volcanic explosions from Mt. Cleveland Volcano, Alaska with infrasound and ground-coupled airwaves. *Geophysical Research Letters*, *39*(21), L21312. <https://doi.org/10.1029/2012GL053635>
- Degruyter, W., & Bonadonna, C. (2012). Improving mass flow rate estimates of volcanic eruptions. *Geophysical Research Letters*, *39*(16), 16308. <https://doi.org/10.1029/2012GL052566>
- Degruyter, W., & Bonadonna, C. (2013). Impact of wind on the condition for column collapse of volcanic plumes. *Earth and Planetary Science Letters*, *377*, 218–226. <https://doi.org/10.1016/j.epsl.2013.06.041>
- de Laat, A., Vazquez-Navarro, M., Theys, N., & Stammes, P. (2020). Analysis of properties of the 19 February 2018 volcanic eruption of Mount Sinabung in S5P/TROPOMI and Himawari-8 satellite data. *Natural Hazards and Earth System Sciences*, *20*(5), 1203–1217. <https://doi.org/10.5194/nhess-20-1203-2020>
- Del Bello, E., Taddeucci, J., Merrison, J. P., Alois, S., Iversen, J. J., & Scarlato, P. (2018). Experimental simulations of volcanic ash resuspension by wind under the effects of atmospheric humidity. *Scientific Reports*, *8*(1), 14509. <https://doi.org/10.1038/s41598-018-32807-2>
- Delene, D. J., Rose, W. I., & Grody, N. C. (1996). Remote sensing of volcanic ash clouds using special sensor microwave imager data. *Journal of Geophysical Research*, *101*(B5), 11579–11588. <https://doi.org/10.1029/96JB00643>
- Deligne, N. I., Jenkins, S. F., Meredith, E. S., Williams, G. T., Leonard, G. S., Stewart, C., et al. (2022). From anecdotes to quantification: Advances in characterizing volcanic eruption impacts on the built environment. *Bulletin of Volcanology*, *84*(1), 7. <https://doi.org/10.1007/s00445-021-01506-8>
- Dellino, P., Mele, D., Bonasia, R., Braia, G., La Volpe, L., & Sulpizio, R. (2005). The analysis of the influence of pumice shape on its terminal velocity. *Geophysical Research Letters*, *32*(21), L21306. <https://doi.org/10.1029/2005GL023954>
- de' Michieli Vitturi, M., & Aravena, Á. (2021). Numerical modeling of magma ascent dynamics. In *Forecasting and planning for volcanic hazards, risks, and disasters* (pp. 239–284). Elsevier. <https://doi.org/10.1016/B978-0-12-818082-2.00006-8>
- de' Michieli Vitturi, M., Neri, A., & Barsotti, S. (2015). PLUME-MoM 1.0: A new integral model of volcanic plumes based on the method of moments. *Geoscientific Model Development*, *8*(8), 2447–2463. <https://doi.org/10.5194/gmd-8-2447-2015>
- de' Michieli Vitturi, M., & Pardini, F. (2021). PLUME-MoM-TSM 1.0.0: A volcanic column and umbrella cloud spreading model. *Geoscientific Model Development*, *14*(3), 1345–1377. <https://doi.org/10.5194/gmd-14-1345-2021>
- Devenish, B. J. (2013). Using simple plume models to refine the source mass flux of volcanic eruptions according to atmospheric conditions. *Journal of Volcanology and Geothermal Research*, *256*, 118–127. <https://doi.org/10.1016/j.jvolgeores.2013.02.015>
- Devenish, B. J. (2016). Estimating the total mass emitted by the eruption of Eyjafjallajökull in 2010 using plume-rise models. *Journal of Volcanology and Geothermal Research*, *326*, 114–119. <https://doi.org/10.1016/j.jvolgeores.2016.01.005>
- Devenish, B. J., Rooney, G. G., Webster, H. N., & Thomson, D. J. (2010). The entrainment rate for buoyant plumes in a crossflow. *Boundary-Layer Meteorology*, *134*(3), 411–439. <https://doi.org/10.1007/s10546-009-9464-5>
- Devenish, B. J., Thomson, D. J., Marengo, F., Leadbetter, S. J., Ricketts, H., & Dacre, H. F. (2012). A study of the arrival over the United Kingdom in April 2010 of the Eyjafjallajökull ash cloud using ground-based lidar and numerical simulations. *Atmospheric Environment*, *48*, 152–164. <https://doi.org/10.1016/j.atmosenv.2011.06.033>
- Diller, K., Clarke, A. B., Voight, B., & Neri, A. (2006). Mechanisms of conduit plug formation: Implications for vulcanian explosions. *Geophysical Research Letters*, *33*(20), L20302. <https://doi.org/10.1029/2006GL027391>
- Dioguardi, F., Beckett, F., Dürig, T., & Stevenson, J. A. (2020). The impact of eruption source parameter uncertainties on ash dispersion forecasts during explosive volcanic eruptions. *Journal of Geophysical Research: Atmospheres*, *125*(17), e2020JD032717. <https://doi.org/10.1029/2020JD032717>
- Dioguardi, F., Mele, D., & Dellino, P. (2018). A new one-equation model of fluid drag for irregularly shaped particles valid over a wide range of Reynolds number. *Journal of Geophysical Research: Solid Earth*, *123*(1), 144–156. <https://doi.org/10.1002/2017JB014926>
- Dominguez, L., Bonadonna, C., Forte, P., Jarvis, P. A., Cioni, R., Mingari, L., et al. (2020). Aeolian remobilisation of the 2011-Cordón Caulle tephra-fallout deposit: Example of an important process in the life cycle of volcanic ash. *Frontiers in Earth Science*, *7*, 343. <https://doi.org/10.3389/feart.2019.00343>
- Dominguez, L., Rossi, E., Mingari, L., Bonadonna, C., Forte, P., Panebianco, J. E., & Bran, D. (2020). Mass flux decay timescales of volcanic particles due to aeolian processes in the Argentinian Patagonia steppe. *Scientific Reports*, *10*(1), 14456. <https://doi.org/10.1038/s41598-020-71022-w>
- Donnadieu, F. (2012). *Volcanological applications of Doppler radars: A review and examples from a transportable pulse radar in L-band*. INTECH Open Access Publisher.
- Donnadieu, F., Frevill, P., Hervier, C., Coltelli, M., Scollo, S., Prestifilippo, M., et al. (2016). Near-source Doppler radar monitoring of tephra plumes at Etna. *Journal of Volcanology and Geothermal Research*, *312*, 26–39. <https://doi.org/10.1016/j.jvolgeores.2016.01.009>

- Donnadieu, F., Valade, S., & Moune, S. (2011). Three dimensional transport speed of wind-drifted ash plumes using ground-based radar. *Geophysical Research Letters*, *38*(18), L18310. <https://doi.org/10.1029/2011GL049001>
- Douillet, G. A., Rasmussen, K. R., Kueppers, U., Castro, D. L., Merrison, J. P., Iversen, J. J., & Dingwell, D. B. (2014). Saltation threshold for pyroclasts at various bed slopes: Wind tunnel measurements. *Journal of Volcanology and Geothermal Research*, *278*, 14–24. <https://doi.org/10.1016/j.jvolgeores.2014.03.011>
- Draxler, R. R., & Hess, G. D. (1997). Description of the HYSPLIT4 modeling system.
- Dubuisson, P., Herbin, H., Minvielle, F., Compiègne, M., Thieuleux, F., Parol, F., & Pelon, J. (2014). Remote sensing of volcanic ash plumes from thermal infrared: A case study analysis from SEVIRI, MODIS and IASI instruments. *Atmospheric Measurement Techniques*, *7*(2), 359–371. <https://doi.org/10.5194/amt-7-359-2014>
- Durant, A. J. (2015). Toward a realistic formulation of fine-ash lifetime in volcanic clouds. *Geology*, *43*(3), 271–272. <https://doi.org/10.1130/focus032015.1>
- Durant, A. J., Shaw, R. A., Rose, W. I., Mi, Y., & Ernst, G. G. J. (2008). Ice nucleation and overseeding of ice in volcanic clouds. *Journal of Geophysical Research*, *113*(D9), D09206. <https://doi.org/10.1029/2007JD009064>
- Dürig, T., Gudmundsson, M. T., Dioguardi, F., & Schmidt, L. S. (2023). Quantifying the effect of wind on volcanic plumes: Implications for plume modeling. *Journal of Geophysical Research: Atmospheres*, *128*(2), e2022JD037781. <https://doi.org/10.1029/2022JD037781>
- Dürig, T., Gudmundsson, M. T., Dioguardi, F., Woodhouse, M., Björnsson, H., Barsotti, S., et al. (2018). REFIR-A multi-parameter system for near real-time estimates of plume-height and mass eruption rate during explosive eruptions. *Journal of Volcanology and Geothermal Research*, *360*, 61–83. <https://doi.org/10.1016/j.jvolgeores.2018.07.003>
- Eckhardt, S., Prata, A. J., Seibert, P., Stebel, K., & Stohl, A. (2008). Estimation of the vertical profile of sulfur dioxide injection into the atmosphere by a volcanic eruption using satellite column measurements and inverse transport modeling. *Atmospheric Chemistry and Physics*, *8*(14), 3881–3897. <https://doi.org/10.5194/acp-8-3881-2008>
- Eliasson, J. (2020). New model for dispersion of volcanic ash and dust in the troposphere. *International Journal of Geosciences*, *11*(8), 544–561. <https://doi.org/10.4236/ijg.2020.118029>
- Eliasson, J., Watson, I. M., & Weber, K. (2016). In situ observations of airborne ash from manned aircraft. In *Volcanic ash* (pp. 89–98). Elsevier. <https://doi.org/10.1016/B978-0-08-100405-0.00009-4>
- Eliasson, J., Yasuda, N., Weber, K., Voge, A., & Pálsson, T. (2014). The role of in-situ measurements of volcanic ash concentrations in preventing economic disasters due to volcanic ash clouds. *IDRiM Journal*, *4*(1), 48–60. <https://doi.org/10.5595/idrim.2014.0092>
- Eliasson, J., Yoshitani, J., Weber, K., Yasuda, N., Iguchi, M., & Vogel, A. (2014). Airborne measurement in the ash plume from mount sakurajima: Analysis of gravitational effects on dispersion and fallout. *International Journal of Atmospheric Sciences*, *2014*, 1–16. <https://doi.org/10.1155/2014/372135>
- Ellrod, G. P., Connell, B. H., & Hillger, D. W. (2003). Improved detection of airborne volcanic ash using multispectral infrared satellite data. *Journal of Geophysical Research*, *108*(D12), 4356. <https://doi.org/10.1029/2002JD002802>
- Engwell, S., Mastin, L., Tupper, A., Kibler, J., Acethorp, P., Lord, G., & Filgueira, R. (2021). Near-real-time volcanic cloud monitoring: Insights into global explosive volcanic eruptive activity through analysis of volcanic ash advisories. *Bulletin of Volcanology*, *83*(2), 1–17. <https://doi.org/10.1007/s00445-020-01419-y>
- Engwell, S., Mastin, L. G., Bonadonna, C., Barsotti, S., Deligne, N. I., & Oladottir, B. A. (2024). Characterising, quantifying, and accessing eruption source parameters of explosive volcanic eruptions for operational simulation of tephra dispersion: A current view and future perspectives. *Bulletin of Volcanology*, *86*(7), 67. <https://doi.org/10.1007/s00445-024-01706-y>
- Eriksson, P., Rydberg, B., Mattioli, V., Thoss, A., Accadia, C., Klein, U., & Buehler, S. A. (2020). Towards an operational Ice Cloud Imager (ICI) retrieval product. *Atmospheric Measurement Techniques*, *13*(1), 53–71. <https://doi.org/10.5194/amt-13-53-2020>
- Esposti Ongaro, T., & Cerminara, M. (2016). Non-equilibrium processes in ash-laden volcanic plumes: New insights from 3D multiphase flow simulations. *Journal of Volcanology and Geothermal Research*, *326*, 127–142. <https://doi.org/10.1016/j.jvolgeores.2016.04.004>
- Esse, B., Burton, M., Varnam, M., Kazahaya, R., Wallace, P. A., Von-Aulock, F., et al. (2018). Quantification of ash sedimentation dynamics through depolarisation imaging with AshCam. *Scientific Reports*, *8*(1), 15680. <https://doi.org/10.1038/s41598-018-34110-6>
- Evensen, G. (1994). Sequential data assimilation with a nonlinear quasi-geostrophic model using Monte Carlo methods to forecast error statistics. *Journal of Geophysical Research*, *99*(C5), 10143–10162. <https://doi.org/10.1029/94JC00572>
- Falcone, A. M., & Cataldo, J. C. (2003). Entrainment velocity in an axisymmetric turbulent jet. *Transactions of the ASME*, *125*(4), 620–627. <https://doi.org/10.1115/1.1595674>
- Fee, D., Garcés, M., & Steffke, A. (2010). Infrasound from Tungurahua volcano 2006–2008: Strombolian to plinian eruptive activity. *Journal of Volcanology and Geothermal Research*, *193*(1–2), 67–81. <https://doi.org/10.1016/j.jvolgeores.2010.03.006>
- Fee, D., & Matoza, R. S. (2013). An overview of volcano infrasound: From Hawaiian to Plinian, local to global. *Journal of Volcanology and Geothermal Research*, *249*, 123–139. <https://doi.org/10.1016/j.jvolgeores.2012.09.002>
- Feng, J. (2008). A size-resolved model and a four-mode parameterization of dry deposition of atmospheric aerosols. *Journal of Geophysical Research*, *113*(D12), D12201. <https://doi.org/10.1029/2007JD009004>
- Fero, J., Carey, S. N., & Merrill, J. T. (2009). Simulating the dispersal of tephra from the 1991 Pinatubo eruption: Implications for the formation of widespread ash layers. *Journal of Volcanology and Geothermal Research*, *186*(1–2), 120–131. <https://doi.org/10.1016/j.jvolgeores.2009.03.011>
- Fiantis, D., Ginting, F. I., Nelson, M., & Minasny, B. (2019). Volcanic ash, Insecurity for the people but securing fertile soil for the future. *Sustainability*, *11*(11), 3072. <https://doi.org/10.3390/su11113072>
- Folch, A. (2012). A review of tephra transport and dispersal models: Evolution, current status, and future perspectives. *Journal of Volcanology and Geothermal Research*, *235*, 96–115. <https://doi.org/10.1016/j.jvolgeores.2012.05.020>
- Folch, A., Abril, C., Afanasiev, M., Amati, G., Bader, M., Badia, R. M., et al. (2023). The EU center of excellence for Exascale in solid Earth (ChEES): Implementation, results, and roadmap for the second phase. *Future Generation Computer Systems*, *146*, 47–61. <https://doi.org/10.1016/j.future.2023.04.006>
- Folch, A., Costa, A., & Basart, S. (2012). Validation of the FALL3D ash dispersion model using observations of the 2010 Eyjafjallajökull volcanic ash clouds. *Atmospheric Environment*, *48*, 165–183. <https://doi.org/10.1016/j.atmosenv.2011.06.072>
- Folch, A., Costa, A., Durant, A., & Macedonio, G. (2010). A model for wet aggregation of ash particles in volcanic plumes and clouds: 2. Model application. *Journal of Geophysical Research*, *115*(B9), B09202. <https://doi.org/10.1029/2009JB007176>
- Folch, A., Costa, A., & Macedonio, G. (2009). FALL3D: A computational model for transport and deposition of volcanic ash. *Computers & Geosciences*, *35*(6), 1334–1342. <https://doi.org/10.1016/j.cageo.2008.08.008>
- Folch, A., Costa, A., & Macedonio, G. (2016). FPLUME-1.0: An integral volcanic plume model accounting for ash aggregation. *Geoscientific Model Development*, *9*(1), 431–450. <https://doi.org/10.5194/gmd-9-431-2016>

- Folch, A., Costa, A., Macedonio, G., & Mingari, L. (2022). FALL3D (version 8.1.2) [Software]. *Zenodo*. <https://doi.org/10.5281/zenodo.6343786>
- Folch, A., Mingari, L., Gutierrez, N., Hanzlich, M., Macedonio, G., & Costa, A. (2020). FALL3D-8.0: A computational model for atmospheric transport and deposition of particles, aerosols and radionuclides—Part 1: Model physics and numerics. *Geoscientific Model Development*, 13(3), 1431–1458. <https://doi.org/10.5194/gmd-13-1431-2020>
- Folch, A., Mingari, L., Osorio, M. S., & Collini, E. (2014). Modeling volcanic ash resuspension—application to the 14–18 October 2011 outbreak episode in central Patagonia, Argentina. *Natural Hazards and Earth System Sciences*, 14(1), 119–133. <https://doi.org/10.5194/nhess-14-119-2014>
- Folch, A., Mingari, L., & Prata, A. T. (2022). Ensemble-based forecast of volcanic clouds using FALL3D-8.1. *Frontiers in Earth Science*, 9, 741841. <https://doi.org/10.3389/feart.2021.741841>
- Folch, A., & Sulpizio, R. (2010). Evaluating long-range volcanic ash hazard using supercomputing facilities: Application to Somma-Vesuvius (Italy), and consequences for civil aviation over the central Mediterranean area. *Bulletin of Volcanology*, 72(9), 1039–1059. <https://doi.org/10.1007/s00445-010-0386-3>
- Forbes, L., Jarvis, D., Potts, J., & Baxter, P. J. (2003). Volcanic ash and respiratory symptoms in children on the island of Montserrat, British West Indies. *Occupational and Environmental Medicine*, 60(3), 207–211. <https://doi.org/10.1136/oem.60.3.207>
- Fowler, A. C., & Scheu, B. (2016). A theoretical explanation of grain size distributions in explosive rock fragmentation. *Proceedings of the Royal Society A: Mathematical, Physical and Engineering Sciences*, 472(2190), 20150843. <https://doi.org/10.1098/rspa.2015.0843>
- Francis, P. N., Cooke, M. C., & Saunders, R. W. (2012). Retrieval of physical properties of volcanic ash using Meteosat: A case study from the 2010 Eyjafjallajökull eruption. *Journal of Geophysical Research*, 117(D20), D00U09. <https://doi.org/10.1029/2011JD016788>
- Freret-Lorgeril, V., Bonadonna, C., Corradini, S., Donnadieu, F., Guerrieri, L., Lacanna, G., et al. (2021). Examples of multi-sensor determination of eruptive source parameters of explosive events at Mount Etna. *Remote Sensing*, 13(11), 2097. <https://doi.org/10.3390/rs13112097>
- Freret-Lorgeril, V., Bonadonna, C., Corradini, S., Guerrieri, L., Lemus, J., Donnadieu, F., et al. (2022). Tephra characterization and multi-disciplinary determination of eruptive source parameters of a weak paroxysm at Mount Etna (Italy). *Journal of Volcanology and Geothermal Research*, 421, 107431. <https://doi.org/10.1016/j.jvolgeores.2021.107431>
- Freret-Lorgeril, V., Bonadonna, C., Rossi, E., Poulidis, A. P., & Iguchi, M. (2022). New insights into real-time detection of tephra grainsize, settling velocity and sedimentation rate. *Scientific Reports*, 12(1), 4650. <https://doi.org/10.1038/s41598-022-08711-1>
- Freret-Lorgeril, V., Donnadieu, F., Eycheenne, J., Soriaux, C., & Latchimy, T. (2019). In situ terminal settling velocity measurements at Stromboli volcano: Input from physical characterization of ash. *Journal of Volcanology and Geothermal Research*, 374, 62–79. <https://doi.org/10.1016/j.jvolgeores.2019.02.005>
- Freret-Lorgeril, V., Donnadieu, F., Scollo, S., Provost, A., Fréville, P., Guéhenneux, Y., et al. (2018). Mass eruption rates of tephra plumes during the 2011–2015 lava fountain paroxysms at Mt. Etna from Doppler radar retrievals. *Frontiers in Earth Science*, 6, 73. <https://doi.org/10.3389/feart.2018.00073>
- Friedman, P. D., Vadakoot, V. D., Meyer, W. J., Jr., & Carey, S. (2007). Instability threshold of a negatively buoyant fountain. *Experiments in Fluids*, 42(5), 751–759. <https://doi.org/10.1007/s00348-007-0283-5>
- Fries, A., Lemus, J., Jarvis, P. A., Clarke, A. B., Phillips, J. C., Manzella, I., & Bonadonna, C. (2021). The influence of particle concentration on the formation of settling-driven gravitational instabilities at the base of volcanic clouds. *Frontiers in Earth Science*, 9, 640090. <https://doi.org/10.3389/feart.2021.640090>
- Fu, G., Prata, F., Lin, H. X., Heemink, A., Segers, A., & Lu, S. (2017). Data assimilation for volcanic ash plumes using a satellite observational operator: A case study on the 2010 Eyjafjallajökull volcanic eruption. *Atmospheric Chemistry and Physics*, 17(2), 1187–1205. <https://doi.org/10.5194/acp-17-1187-2017>
- Gabellini, P., Rossi, E., Bonadonna, C., Pistolesi, M., Bagheri, G., & Cioni, R. (2020). Physical and aerodynamic characterization of particle clusters at Sakurajima Volcano (Japan). *Frontiers in Earth Science*, 8, 575874. <https://doi.org/10.3389/feart.2020.575874>
- Gangale, G., Prata, A. J., & Clarisse, L. (2010). The infrared spectral signature of volcanic ash determined from high-spectral resolution satellite measurements. *Remote Sensing of Environment*, 114(2), 414–425. <https://doi.org/10.1016/j.rse.2009.09.007>
- Ganser, G. H. (1993). A rational approach to drag prediction of spherical and nonspherical particles. *Powder Technology*, 77(2), 143–152. [https://doi.org/10.1016/0032-5910\(93\)80051-B](https://doi.org/10.1016/0032-5910(93)80051-B)
- Gardner, J. E., Wadsworth, F. B., Carley, T. L., Llewellyn, E. W., Kusumaatmaja, H., & Sahagian, D. (2023). Bubble formation in magma. *Annual Review of Earth and Planetary Sciences*, 51(1), 131–154. <https://doi.org/10.1146/annurev-earth-031621-080308>
- Gasteiger, J., Groß, S., Freudenthaler, V., & Wiegner, M. (2011). Volcanic ash from Iceland over Munich: Mass concentration retrieved from ground-based remote sensing measurements. *Atmospheric Chemistry and Physics*, 11(5), 2209–2223. <https://doi.org/10.5194/acp-11-2209-2011>
- Giehl, C., Brooker, R. A., Marxer, H., & Nowak, M. (2017). An experimental simulation of volcanic ash deposition in gas turbines and implications for jet engine safety. *Chemical Geology*, 461, 160–170. <https://doi.org/10.1016/j.chemgeo.2016.11.024>
- Gilbert, J. S., & Lane, S. J. (1994). The origin of accretionary lapilli. *Bulletin of Volcanology*, 56(5), 398–411. <https://doi.org/10.1007/BF00326465>
- Giles, T. M., Newnham, R. M., Lowe, D. J., & Munro, A. J. (1999). Impact of tephra fall and environmental change: A 1000 year record from Matakana Island, Bay of Plenty, North Island, New Zealand. *Geological Society, London, Special Publications*, 161(1), 11–26. <https://doi.org/10.1144/gsl.sp.1999.161.01.03>
- Gomez, C., & Kennedy, B. (2018). Capturing volcanic plumes in 3D with UAV-based photogrammetry at Yasur Volcano—Vanuatu. *Journal of Volcanology and Geothermal Research*, 350, 84–88. <https://doi.org/10.1016/j.jvolgeores.2017.12.007>
- Gonnermann, H. M. (2015). Magma fragmentation. *Annual Review of Earth and Planetary Sciences*, 43(1), 431–458. <https://doi.org/10.1146/annurev-earth-060614-105206>
- Gonnermann, H. M., & Manga, M. (2007). The fluid mechanics inside a volcano. *Annual Review of Fluid Mechanics*, 39(1), 321–356. <https://doi.org/10.1146/annurev.fluid.39.050905.110207>
- Gorkavyi, N., Carn, S., DeLand, M., Knyazikhin, Y., Krotkov, N., Marshak, A., et al. (2021). Earth imaging from the surface of the moon with a DSCOVR/EPIC-type camera. *Frontiers in Remote Sensing*, 2, 724074. <https://doi.org/10.3389/frsen.2021.724074>
- Gouhier, M., Deslandes, M., Guéhenneux, Y., Hereil, P., Cacault, P., & Josse, B. (2020). Operational response to volcanic ash risks using HOTVOLC satellite-based system and MOCAGE-accident model at the Toulouse VAAC. *Atmosphere*, 11(8), 864. <https://doi.org/10.3390/atmos11080864>
- Gouhier, M., Eycheenne, J., Azzaoui, N., Guillin, A., Deslandes, M., Poret, M., et al. (2019). Low efficiency of large volcanic eruptions in transporting very fine ash into the atmosphere. *Scientific Reports*, 9(1), 1449. <https://doi.org/10.1038/s41598-019-38595-7>
- Grainger, R. G., Peters, D. M., Thomas, G. E., Smith, A. J. A., Siddans, R., Carboni, E., & Dudhia, A. (2013). Measuring volcanic plume and ash properties from space. *Geological Society, London, Special Publications*, 380(1), 293–320. <https://doi.org/10.1144/SP380.7>

- Gray, T. M., & Bennartz, R. (2015). Automatic volcanic ash detection from MODIS observations using a back-propagation neural network. *Atmospheric Measurement Techniques*, 8(12), 5089–5097. <https://doi.org/10.5194/amt-8-5089-2015>
- Griessbach, S., Hoffmann, L., Spang, R., & Riese, M. (2014). Volcanic ash detection with infrared limb sounding: MIPAS observations and radiative transfer simulations. *Atmospheric Measurement Techniques*, 7(5), 1487–1507. <https://doi.org/10.5194/amt-7-1487-2014>
- Gu, Y., Rose, W. I., & Bluth, G. J. (2003). Retrieval of mass and sizes of particles in sandstorms using two MODIS IR bands: A case study of April 7, 2001 sandstorm in China. *Geophysical Research Letters*, 30(15), 1805. <https://doi.org/10.1029/2003GL017405>
- Gu, Y., Rose, W. I., Schneider, D. J., Bluth, G. J., & Watson, I. M. (2005). Advantageous GOES IR results for ash mapping at high latitudes: Cleveland eruptions 2001. *Geophysical Research Letters*, 32(2), 5. <https://doi.org/10.1029/2004GL021651>
- Gudmundsson, G. (2011). Respiratory health effects of volcanic ash with special reference to Iceland. A review. *The clinical respiratory journal*, 5(1), 2–9. <https://doi.org/10.1111/j.1752-699X.2010.00231.x>
- Gudmundsson, M. T., Pedersen, R., Vogfjörð, K., Thorbjarnardóttir, B., Jakobsdóttir, S., & Roberts, M. J. (2010). Eruptions of Eyjafjallajökull Volcano, Iceland. *Eos, Transactions of the American Geophysical Union*, 91(21), 190–191. <https://doi.org/10.1029/2010EO210002>
- Gudmundsson, M. T., Thordarson, T., Höskuldsson, Á., Larsen, G., Björnsson, H., Prata, F. J., et al. (2012). Ash generation and distribution from the April–May 2010 eruption of Eyjafjallajökull. *Iceland. Scientific Reports*, 2(1), 572. <https://doi.org/10.1038/srep00572>
- Guéhenneux, Y., Gouhier, M., & Labazuy, P. (2015). Improved space borne detection of volcanic ash for real-time monitoring using 3-Band method. *Journal of Volcanology and Geothermal Research*, 293, 25–45. <https://doi.org/10.1016/j.jvolgeores.2015.01.005>
- Guerrero Tello, J. F., Coltelli, M., Marsella, M., Celauro, A., & Palenzuela Baena, J. A. (2022). Convolutional neural network algorithms for Semantic segmentation of volcanic ash plumes using visible camera imagery. *Remote Sensing*, 14(18), 4477. <https://doi.org/10.3390/rs14184477>
- Han, Y., Revercomb, H., Cromp, M., Gu, D., Johnson, D., Mooney, D., et al. (2013). Suomi NPP CrIS measurements, sensor data record algorithm, calibration and validation activities, and record data quality. *Journal of Geophysical Research: Atmospheres*, 118(22), 12–734. <https://doi.org/10.1002/2013JD020344>
- Harris, A. J., Ripepe, M., & Hughes, E. A. (2012). Detailed analysis of particle launch velocities, size distributions and gas densities during normal explosions at Stromboli. *Journal of Volcanology and Geothermal Research*, 231, 109–131. <https://doi.org/10.1016/j.jvolgeores.2012.02.012>
- Harris, D. M., & Rose, W. I., Jr. (1983). Estimating particle sizes, concentrations, and total mass of ash in volcanic clouds using weather radar. *Journal of Geophysical Research*, 88(C15), 10969–10983. <https://doi.org/10.1029/JC088iC15p10969>
- Harvey, N. J., Dacre, H. F., Saint, C., Prata, A. T., Webster, H. N., & Grainger, R. G. (2022). Quantifying the impact of meteorological uncertainty on emission estimates and the risk to aviation using source inversion for the Raikoke 2019 eruption. *Atmospheric Chemistry and Physics*, 22(13), 8529–8545. <https://doi.org/10.5194/acp-22-8529-2022>
- Hasegawa, Y., Sugai, A., Hayashi, Y., Hayashi, Y., Saito, S., & Shimbori, T. (2015). Improvements of volcanic ash fall forecasts issued by the Japan Meteorological Agency. *Journal of Applied Volcanology*, 4, 1–12. <https://doi.org/10.1186/s13617-014-0018-2>
- Hayes, J. L., Calderón, R., Deligne, N. I., Jenkins, S. F., Leonard, G. S., McSparran, A. M., et al. (2019). Timber-framed building damage from tephra fall and lahar: 2015 Calbuco eruption, Chile. *Journal of Volcanology and Geothermal Research*, 374, 142–159. <https://doi.org/10.1016/j.jvolgeores.2019.02.017>
- Hayes, J. L., Wilson, T. M., Stewart, C., Villarosa, G., Salgado, P., Beigt, D., et al. (2019). Tephra clean-up after the 2015 eruption of Calbuco volcano, Chile: A quantitative geospatial assessment in four communities. *Journal of Applied Volcanology*, 8, 1–23. <https://doi.org/10.1186/s13617-019-0087-3>
- Herman, J. R., Bhartia, P. K., Torres, O., Hsu, C., Sefior, C., & Celarier, E. (1997). Global distribution of UV-absorbing aerosols from Nimbus 7/TOMS data. *Journal of Geophysical Research*, 102(D14), 16911–16922. <https://doi.org/10.1029/96JD03680>
- Hersbach, H., Bell, B., Berrisford, P., Hirahara, S., Horányi, A., Muñoz-Sabater, J., et al. (2020). The ERA5 global reanalysis. *Quarterly Journal of the Royal Meteorological Society*, 146(730), 1999–2049. <https://doi.org/10.1002/qj.3803>
- Hewett, T. A., Fay, J. A., & Hoult, D. P. (1971). Laboratory experiments of smokestack plumes in a stable atmosphere. *Atmospheric Environment*, 5(9), 767–789. [https://doi.org/10.1016/0004-6981\(71\)90028-X](https://doi.org/10.1016/0004-6981(71)90028-X)
- Hillger, D. W., & Clark, J. D. (2002a). Principal component image analysis of MODIS for volcanic ash. Part I: Most important bands and implications for future GOES imagers. *Journal of Applied Meteorology and Climatology*, 41(10), 985–1001. [https://doi.org/10.1175/1520-0450\(2002\)041<0985:PCIAOM>2.0.CO;2](https://doi.org/10.1175/1520-0450(2002)041<0985:PCIAOM>2.0.CO;2)
- Hillger, D. W., & Clark, J. D. (2002b). Principal component image analysis of MODIS for volcanic ash. Part II: Simulation of current GOES and GOES-M imagers. *Journal of Applied Meteorology*, 41(10), 1003–1010. [https://doi.org/10.1175/1520-0450\(2002\)041<1003:PCIAOM>2.0.CO;2](https://doi.org/10.1175/1520-0450(2002)041<1003:PCIAOM>2.0.CO;2)
- Hillman, S. E., Horwell, C. J., Densmore, A. L., Damby, D. E., Fubini, B., Ishimine, Y., & Tomatis, M. (2012). Sakurajima volcano: A physico-chemical study of the health consequences of long-term exposure to volcanic ash. *Bulletin of Volcanology*, 74(4), 913–930. <https://doi.org/10.1007/s00445-012-0575-3>
- Hirtl, M., Scherllin-Pirscher, B., Stuefer, M., Arnold, D., Baro, R., Maurer, C., & Mulder, M. D. (2020). Extension of the WRF-Chem volcanic emission preprocessor to integrate complex source terms and evaluation for different emission scenarios of the Grimsvötn 2011 eruption. *Natural Hazards and Earth System Sciences*, 20(11), 3099–3115. <https://doi.org/10.5194/nhess-20-3099-2020>
- Hirtl, M., Stuefer, M., Arnold, D., Grell, G., Maurer, C., Natali, S., et al. (2019). The effects of simulating volcanic aerosol radiative feedbacks with WRF-Chem during the Eyjafjallajökull eruption, April and May 2010. *Atmospheric Environment*, 198, 194–206. <https://doi.org/10.1016/j.atmosenv.2018.10.058>
- Hobbs, P. V., Radke, L. F., Lyons, J. H., Ferek, R. J., Coffman, D. J., & Casadevall, T. J. (1991). Airborne measurements of particle and gas emissions from the 1990 volcanic eruptions of Mount Redoubt. *Journal of Geophysical Research*, 96(D10), 18735–18752. <https://doi.org/10.1029/91JD01635>
- Hobbs, P. V., Tuell, J. P., Hegg, D. A., Radke, L. F., & Eltgroth, M. W. (1982). Particles and gases in the emissions from the 1980–1981 volcanic eruptions of Mt. St. Helens. *Journal of Geophysical Research*, 87(C13), 11062–11086. <https://doi.org/10.1029/JC087iC13p11062>
- Hoffmann, L., Griessbach, S., & Meyer, C. I. (2014). Volcanic emissions from AIRS observations: Detection methods, case study, and statistical analysis. In *Remote sensing of clouds and the atmosphere XIX; and optics in atmospheric propagation and adaptive systems XVII* (Vol. 9242, pp. 305–312). SPIE. <https://doi.org/10.1117/12.2066326>
- Holasek, R. E., & Rose, W. I. (1991). Anatomy of 1986 Augustine volcano eruptions as recorded by multispectral image processing of digital AVHRR weather satellite data. *Bulletin of Volcanology*, 53(6), 420–435. <https://doi.org/10.1007/BF00258183>
- Holasek, R. E., Self, S., & Woods, A. W. (1996). Satellite observations and interpretation of the 1991 Mount Pinatubo eruption plumes. *Journal of Geophysical Research*, 101(B12), 27635–27655. <https://doi.org/10.1029/96JB01179>

- Horváth, Á., Carr, J. L., Girina, O. A., Wu, D. L., Bril, A. A., Mazurov, A. A., et al. (2021). Geometric estimation of volcanic eruption column height from GOES-R near-limb imagery—Part 1: Methodology. *Atmospheric Chemistry and Physics*, 21(16), 12189–12206. <https://doi.org/10.5194/acp-21-12189-2021>
- Horváth, Á., Carr, J. L., Wu, D. L., Bruckert, J., Hoshyaripour, G. A., & Buehler, S. A. (2022). Measurement report: Plume heights of the April 2021 La Soufrière eruptions from GOES-17 side views and GOES-16-MODIS stereo views. *Atmospheric Chemistry and Physics*, 22(18), 12311–12330. <https://doi.org/10.5194/acp-22-12311-2022>
- Horváth, Á., Girina, O. A., Carr, J. L., Wu, D. L., Bril, A. A., Mazurov, A. A., et al. (2021). Geometric estimation of volcanic eruption column height from GOES-R near-limb imagery—Part 2: Case studies. *Atmospheric Chemistry and Physics*, 21(16), 12207–12226. <https://doi.org/10.5194/acp-21-12207-2021>
- Horwell, C. J., Sparks, R. S. J., Brewer, T. S., Llewellyn, E. W., & Williamson, B. J. (2003). Characterization of respirable volcanic ash from the Soufrière Hills volcano, Montserrat, with implications for human health hazards. *Bulletin of Volcanology*, 65(5), 346–362. <https://doi.org/10.1007/s00445-002-0266-6>
- Houghton, B. F., Wilson, C. J. N., Del Carlo, P., Coltelli, M., Sable, J. E., & Carey, R. (2004). The influence of conduit processes on changes in style of basaltic Plinian eruptions: Tarawera 1886 and Etna 122 BC. *Journal of Volcanology and Geothermal Research*, 137(1–3), 1–14. <https://doi.org/10.1016/j.jvolgeores.2004.05.009>
- Hoult, D. P., Fay, J. A., & Forney, L. J. (1969). A theory of plume rise compared with field observations. *Journal of the Air Pollution Control Association*, 19(8), 585–590. <https://doi.org/10.1080/00022470.1969.10466526>
- Hoult, D. P., & Weil, J. C. (1972). Turbulent plume in a laminar cross flow. *Atmospheric Environment*, 6(8), 513–531. [https://doi.org/10.1016/0004-6981\(72\)90069-8](https://doi.org/10.1016/0004-6981(72)90069-8)
- Hsu, N. C., Herman, J. R., Bhartia, P. K., Sefort, C. J., Torres, O., Thompson, A. M., et al. (1996). Detection of biomass burning smoke from TOMS measurements. *Geophysical Research Letters*, 23(7), 745–748. <https://doi.org/10.1029/96GL00455>
- Huq, P., & Stewart, E. J. (1996). A laboratory study of buoyant plumes in laminar and turbulent crossflows. *Atmospheric Environment*, 30(7), 1125–1135. [https://doi.org/10.1016/1352-2310\(95\)00335-5](https://doi.org/10.1016/1352-2310(95)00335-5)
- Hurst, T., & Davis, C. (2017). Forecasting volcanic ash deposition using HYSPLIT. *Journal of Applied Volcanology*, 6(1), 1–8. <https://doi.org/10.1186/s13617-017-0056-7>
- ICAO. (2010). Meteorological service for international air navigation. Retrieved from <https://www.icao.int/airnavigation/IMP/Documents/Annex%203%20-%2075.pdf>
- ICAO. (2020). Handbook on the International Airways Volcano Watch (IAVW). Doc 9766-AN/968. Retrieved from <https://www.icao.int/airnavigation/METP/MOGVA%20Reference%20Documents/Handbook%20on%20the%20IAVW,%20Doc%209766.pdf>
- ICAO. (2021). *Volcanic ash contingency plan—European and North Atlantic regions, technical report*. International Civil Aviation Organisation.
- ICAO. (2024). *Volcanic ash contingency plan—European and North Atlantic regions, technical report*. International Civil Aviation Organisation. Retrieved from <https://www.icao.int/EURNAT/EUR%20and%20NAT%20Documents/NAT%20Documents/NAT%20Documents/NAT%20Documents/NAT%20Doc%20006%20-%20NAT%20Contingency%20Plan/NAT%20Doc%20006%20Part%20II,%20Ed.%202.2.0.pdf>
- Iguchi, M., Nakamichi, H., Tanaka, H., Ohta, Y., Shimizu, A., & Miki, D. (2019). Integrated monitoring of volcanic ash and forecasting at Sakurajima volcano, Japan. *Journal of Disaster Research*, 14(5), 798–809. <https://doi.org/10.20965/jdr.2019.p0798>
- Illingworth, A. J., Barker, H. W., Beljaars, A., Ceccaldi, M., Chepfer, H., Clerbaux, N., et al. (2015). The EarthCARE satellite: The next step forward in global measurements of clouds, aerosols, precipitation, and radiation. *Bulletin of the American Meteorological Society*, 96(8), 1311–1332. <https://doi.org/10.1175/BAMS-D-12-00227.1>
- Inoue, T. (1985). On the temperature and effective emissivity determination of semi-transparent cirrus clouds by bi-spectral measurements in the 10 μm window region. *Journal of the Meteorological Society of Japanese Series II*, 63(1), 88–99. <https://doi.org/10.2151/jmsj.1965.63.1.88>
- Ishii, K. (2018). Estimation of emission mass from an eruption plume for the Aso volcano eruption, on October 8, 2016, using a four-dimensional variational method. *Earth Planets and Space*, 70, 1–9. <https://doi.org/10.1186/s40623-018-0964-8>
- Ishii, K., Hayashi, M., Ishimoto, H., & Shimbori, T. (2023). Prediction of volcanic ash concentrations in ash clouds from explosive eruptions based on an atmospheric transport model and the Japanese meteorological satellite Himawari-8: A case study for the Kirishima-Shinmoedake eruption on April 4th 2018. *Earth Planets and Space*, 75(1), 37. <https://doi.org/10.1186/s40623-023-01790-y>
- Ishimoto, H., Masuda, K., Fukui, K., Shimbori, T., Inazawa, T., Tuchiya, H., et al. (2016). Estimation of the refractive index of volcanic ash from satellite infrared sounder data. *Remote Sensing of Environment*, 174, 165–180. <https://doi.org/10.1016/j.rse.2015.12.009>
- Jacobson, M. Z. (1999). *Fundamentals of atmospheric modeling*. Cambridge University Press.
- James, M. R., Lane, S. J., & Gilbert, J. S. (2003). Density, construction, and drag coefficient of electrostatic volcanic ash aggregates. *Journal of Geophysical Research*, 108(B9), 24–35. <https://doi.org/10.1029/2002JB002011>
- Jarvis, P. A., Bonadonna, C., Dominguez, L., Forte, P., Frischknecht, C., Bran, D., et al. (2020). Aeolian remobilisation of volcanic ash: Outcomes of a workshop in the Argentinian Patagonia. *Frontiers in Earth Science*, 8, 569. <https://doi.org/10.3389/feart.2020.575184>
- Jenkins, S., Smith, C., Allen, M., & Grainger, R. (2023). Tonga eruption increases chance of temporary surface temperature anomaly above 1.5°C. *Nature Climate Change*, 13(2), 127–129. <https://doi.org/10.1038/s41558-022-01568-2>
- Jenkins, S. F., Barsotti, S., Hincks, T. K., Neri, A., Phillips, J. C., Sparks, R. S. J., et al. (2015). Rapid emergency assessment of ash and gas hazard for future eruptions at Santorini Volcano, Greece. *Journal of Applied Volcanology*, 4(1), 1–22. <https://doi.org/10.1186/s13617-015-0033-y>
- Jessop, D. E., & Jellinek, A. M. (2014). Effects of particle mixtures and nozzle geometry on entrainment into volcanic jets. *Geophysical Research Letters*, 41(11), 3858–3863. <https://doi.org/10.1002/2014GL060059>
- Jing, D., He, Y., Yin, Z., Liu, F., Yi, Y., & Yi, F. (2023). Evolution of aerosol plumes from 2019 Raikoke volcanic eruption observed with polarization lidar over central China. *Atmospheric Environment*, 119880, 119880. <https://doi.org/10.1016/j.atmosenv.2023.119880>
- Johnson, B., Turnbull, K., Brown, P., Burgess, R., Dorsey, J., Baran, A. J., et al. (2012). In situ observations of volcanic ash clouds from the FAAM aircraft during the eruption of Eyjafjallajökull in 2010. *Journal of Geophysical Research*, 117(D20), D00U24. <https://doi.org/10.1029/2011JD016760>
- Jones, A., Thomson, D., Hort, M., & Devenish, B. (2007). The UK Met Office's next-generation atmospheric dispersion model, NAME III. In *Air pollution modeling and its application XVII* (pp. 580–589). Springer US.
- Jones, T. J., Cashman, K. V., Liu, E. J., Rust, A. C., & Scheu, B. (2022). Magma fragmentation: A perspective on emerging topics and future directions. *Bulletin of Volcanology*, 84(5), 45. <https://doi.org/10.1007/s00445-022-01555-7>
- Jones, T. J., & Russell, J. K. (2017). Ash production by attrition in volcanic conduits and plumes. *Scientific Reports*, 7(1), 5538. <https://doi.org/10.1038/s41598-017-05450-6>
- Jordan, S. C., Dürig, T., Cas, R. A., & Zimanowski, B. (2014). Processes controlling the shape of ash particles: Results of statistical IPA. *Journal of Volcanology and Geothermal Research*, 288, 19–27. <https://doi.org/10.1016/j.jvolgeores.2014.09.012>
- Kalman, R. E. (1960). A new approach to linear filtering and prediction problems.

- Kalnay, E., Kanamitsu, M., Kistler, R., Collins, W., Deaven, D., Gandin, L., et al. (2018). The NCEP/NCAR 40-year reanalysis project. In *Renewable energy* (pp. 1146–1194). Routledge. [https://doi.org/10.1175/1520-0477\(1996\)077<0437:TNYRP>2.0.CO;2](https://doi.org/10.1175/1520-0477(1996)077<0437:TNYRP>2.0.CO;2)
- Kaminski, E., & Jaupart, C. (1998). The size distribution of pyroclasts and the fragmentation sequence in explosive volcanic eruptions. *Journal of Geophysical Research*, *103*(B12), 29759–29779. <https://doi.org/10.1029/98JB02795>
- Kaminski, E., Tait, S., & Carazzo, G. (2005). Turbulent entrainment in jets with arbitrary buoyancy. *Journal of Fluid Mechanics*, *526*, 361–376. <https://doi.org/10.1017/S0022112004003209>
- Karamchandani, P., Seigneur, C., Vijayaraghavan, K., & Wu, S. Y. (2002). Development and application of a state-of-the-science plume-in-grid model. *Journal of Geophysical Research*, *107*(D19), ACH12. <https://doi.org/10.1029/2002JD002123>
- Kerminen, V. M., Niemi, J. V., Timonen, H., Aurela, M., Frey, A., Carbone, S., et al. (2011). Characterization of a volcanic ash episode in southern Finland caused by the Grimsvötn eruption in Iceland in May 2011. *Atmospheric Chemistry and Physics*, *11*(23), 12227–12239. <https://doi.org/10.5194/acp-11-12227-2011>
- Khaykin, S., Podglajen, A., Ploeger, F., Grooß, J. U., Tencé, F., Bekki, S., et al. (2022). Global perturbation of stratospheric water and aerosol burden by Hunga eruption. *Communications Earth & Environment*, *3*(1), 316. <https://doi.org/10.1038/s43247-022-00652-x>
- Kieffer, S. W. (1989). Geologic nozzles. *Reviews of Geophysics*, *27*(1), 3–38. <https://doi.org/10.1029/RG0271001p00003>
- Kieffer, S. W., & Sturtevant, B. (1984). Laboratory studies of volcanic jets. *Journal of Geophysical Research*, *89*(B10), 8253–8268. <https://doi.org/10.1029/JB089iB10p08253>
- Kienle, J., & Shaw, G. E. (1979). Plume dynamics, thermal energy and long-distance transport of vulcanian eruption clouds from Augustine volcano, Alaska. *Journal of Volcanology and Geothermal Research*, *6*(1–2), 139–164. [https://doi.org/10.1016/0377-0273\(79\)90051-9](https://doi.org/10.1016/0377-0273(79)90051-9)
- Kim, J., Jeong, U., Ahn, M.-H., Kim, J. H., Park, R. J., Lee, H., et al. (2020). New Era of air quality monitoring from space: Geostationary environment monitoring spectrometer (GEMS). *Bulletin of the American Meteorological Society*, *101*(1), E1–E22. <https://doi.org/10.1175/BAMS-D-18-0013.1>
- Kim, K., Fee, D., Yokoo, A., & Lees, J. M. (2015). Acoustic source inversion to estimate volume flux from volcanic explosions. *Geophysical Research Letters*, *42*(13), 5243–5249. <https://doi.org/10.1002/2015GL064466>
- Kim, M. H., Omar, A. H., Tackett, J. L., Vaughan, M. A., Winker, D. M., Trepte, C. R., et al. (2018). The CALIPSO version 4 automated aerosol classification and lidar ratio selection algorithm. *Atmospheric Measurement Techniques*, *11*(11), 6107–6135. <https://doi.org/10.5194/amt-11-6107-2018>
- Kloss, C., Sellitto, P., Renard, J.-B., Baron, A., Bègue, N., Legras, B., et al. (2022). Aerosol characterization of the stratospheric plume from the volcanic eruption at Hunga Tonga 15 January 2022. *Geophysical Research Letters*, *49*(16), e2022GL099394. <https://doi.org/10.1029/2022GL099394>
- Klüser, L., Erbertseder, T., & Meyer-Arne, J. (2013). Observation of volcanic ash from Puyehue–Cordón Caulle with IASI. *Atmospheric Measurement Techniques*, *6*(1), 35–46. <https://doi.org/10.5194/amt-6-35-2013>
- Kok, J. F., Parteli, E. J., Michaels, T. I., & Karam, D. B. (2012). The physics of wind-blown sand and dust. *Reports on Progress in Physics*, *75*(10), 106901. <https://doi.org/10.1088/0034-4885/75/10/106901>
- Koyaguchi, T., Suzuki, Y. J., & Kozono, T. (2010). Effects of the crater on eruption column dynamics. *Journal of Geophysical Research*, *115*(B7), 69. <https://doi.org/10.1029/2009JB007146>
- Koyaguchi, T., & Tokuno, M. (1993). Origin of the giant eruption cloud of Pinatubo, June 15, 1991. *Journal of Volcanology and Geothermal Research*, *55*(1–2), 85–96. [https://doi.org/10.1016/0377-0273\(93\)90091-5](https://doi.org/10.1016/0377-0273(93)90091-5)
- Koyaguchi, T., & Woods, A. W. (1996). On the formation of eruption columns following explosive mixing of magma and surface-water. *Journal of Geophysical Research*, *101*(B3), 5561–5574. <https://doi.org/10.1029/95JB01687>
- Kozono, T., Iguchi, M., Miwa, T., Maki, M., Maesaka, T., & Miki, D. (2019). Characteristics of tephra fall from eruptions at Sakurajima volcano, revealed by optical disdrometer measurements. *Bulletin of Volcanology*, *81*(7), 1–18. <https://doi.org/10.1007/s00445-019-1300-2>
- Kristiansen, N. I., Prata, A. J., Stohl, A., & Carn, S. A. (2015). Stratospheric volcanic ash emissions from the 13 February 2014 Kelut eruption. *Geophysical Research Letters*, *42*(2), 588–596. <https://doi.org/10.1002/2014GL062307>
- Kristiansen, N. I., Stohl, A., Prata, A. J., Bukowiecki, N., Dacre, H., Eckhardt, S., et al. (2012). Performance assessment of a volcanic ash transport model mini-ensemble used for inverse modeling of the 2010 Eyjafjallajökull eruption. *Journal of Geophysical Research*, *117*(D20), D00U11. <https://doi.org/10.1029/2011JD016844>
- Krotkov, N., Habib, S., da Silva, A., Hughes, E., Yang, K., Brentzel, K., et al. (2014). Real time volcanic cloud products and predictions for aviation alerts. In *6th AIAA atmospheric and space environments conference* (p. 2618). <https://doi.org/10.2514/6.2014-2618>
- Krotkov, N. A., Torres, O., Seftor, C., Krueger, A. J., Kostinski, A., Rose, W. I., et al. (1999). Comparison of TOMS and AVHRR volcanic ash retrievals from the August 1992 eruption of Mt. Spurr. *Geophysical Research Letters*, *26*(4), 455–458. <https://doi.org/10.1029/1998GL900278>
- Krueger, A. F. (1982). Geostationary satellite observations of the April 1979 Soufriere eruptions. *Science*, *216*(4550), 1108–1109. <https://doi.org/10.1126/science.216.4550.1108>
- Kylling, A., Kahnert, M., Lindqvist, H., & Nousiainen, T. (2014). Volcanic ash infrared signature: Porous non-spherical ash particle shapes compared to homogeneous spherical ash particles. *Atmospheric Measurement Techniques*, *7*(4), 919–929. <https://doi.org/10.5194/amt-7-919-2014>
- Lamb, O. D., De Angelis, S., & Lavallée, Y. (2015). Using infrasound to constrain ash plume rise. *Journal of Applied Volcanology*, *4*, 1–9. <https://doi.org/10.1186/s13617-015-0038-6>
- Leadbetter, S. J., Hort, M. C., Jones, A. R., Webster, H. N., & Draxler, R. R. (2015). Sensitivity of the modelled deposition of Caesium-137 from the Fukushima Dai-ichi nuclear power plant to the wet deposition parameterisation in NAME. *Journal of Environmental Radioactivity*, *139*, 200–211. <https://doi.org/10.1016/j.jenvrad.2014.03.018>
- Leadbetter, S. J., Hort, M. C., Von Löwis, S., Weber, K., & Witham, C. S. (2012). Modeling the resuspension of ash deposited during the eruption of Eyjafjallajökull in spring 2010. *Journal of Geophysical Research*, *117*(D20), D00U10. <https://doi.org/10.1029/2011JD016802>
- Lechner, P., Tupper, A., Guffanti, M., Loughlin, S., & Casadevall, T. (2018). Volcanic ash and aviation—The challenges of real-time, global communication of a natural hazard. In *Observing the volcano world: Volcano crisis communication* (pp. 51–64).
- Lemus, J., Fries, A., Jarvis, P. A., Bonadonna, C., Chopard, B., & Lätt, J. (2021). Modelling settling-driven gravitational instabilities at the base of volcanic clouds using the lattice Boltzmann method. *Frontiers in Earth Science*, *9*, 713175. <https://doi.org/10.3389/feart.2021.713175>
- Li, M., Letu, H., Ishimoto, H., Li, S., Liu, L., Nakajima, T. Y., et al. (2023). Retrieval of terahertz ice cloud properties from airborne measurements based on the irregularly shaped Voronoi ice scattering models. *Atmospheric Measurement Techniques*, *16*(2), 331–353. <https://doi.org/10.5194/amt-16-331-2023>
- Liepmann, D. (1991). Streamwise vorticity and entrainment in the near field of a round jet. *Physics of Fluids A*, *3*(5), 1179–1185. <https://doi.org/10.1063/1.858046>

- List, E. J. (1982). Turbulent jets and plumes. *Annual Review of Fluid Mechanics*, 14(1), 189–212. <https://doi.org/10.1146/annurev.fl.14.010182.001201>
- Liu, E. J., Cashman, K. V., Beckett, F. M., Witham, C. S., Leadbetter, S. J., Hort, M. C., & Guðmundsson, S. (2014). Ash mists and Brown snow: Remobilization of volcanic ash from recent Icelandic eruptions. *Journal of Geophysical Research: Atmospheres*, 119(15), 9463–9480. <https://doi.org/10.1002/2014JD021598>
- Liu, E. J., Cashman, K. V., Miller, E., Moore, H., Edmonds, M., Kunz, B. E., et al. (2020). Petrologic monitoring at Volcán de Fuego, Guatemala. *Journal of Volcanology and Geothermal Research*, 405, 107044. <https://doi.org/10.1016/j.jvolgeores.2020.107044>
- Löffler-Mang, M., & Joss, J. (2000). An optical disdrometer for measuring size and velocity of hydrometeors. *Journal of Atmospheric and Oceanic Technology*, 17(2), 130–139. [https://doi.org/10.1175/1520-0426\(2000\)017<0130:AODFMS>2.0.CO;2](https://doi.org/10.1175/1520-0426(2000)017<0130:AODFMS>2.0.CO;2)
- Lopez, T., Fee, D., Prata, F., & Dehn, J. (2013). Characterization and interpretation of volcanic activity at Karymsky Volcano, Kamchatka, Russia, using observations of infrasound, volcanic emissions, and thermal imagery. *Geochemistry, Geophysics, Geosystems*, 14(12), 5106–5127. <https://doi.org/10.1002/2013gc004817>
- Lopez, T., Thomas, H. E., Prata, A. J., Amigo, A., Fee, D., & Moriano, D. (2015). Volcanic plume characteristics determined using an infrared imaging camera. *Journal of Volcanology and Geothermal Research*, 300, 148–166. <https://doi.org/10.1016/j.jvolgeores.2014.12.009>
- Loughlin, S. C., Sparks, R. S. J., Brown, S. K., Jenkins, S. F., & Vye-Brown, C. (2015). *Global volcanic hazards and risk*. Cambridge University Press.
- Lu, S., Lin, H. X., Heemink, A. W., Fu, G., & Segers, A. J. (2016). Estimation of volcanic ash emissions using trajectory-based 4D-Var data assimilation. *Monthly Weather Review*, 144(2), 575–589. <https://doi.org/10.1175/MWR-D-15-0194.1>
- Lynett, P., McCann, M., Zhou, Z., Renteria, W., Borrero, J., Greer, D., et al. (2022). Diverse tsunamigenesis triggered by the Hunga Tonga-Hunga Ha'apai eruption. *Nature*, 609(7928), 728–733. <https://doi.org/10.1038/s41586-022-05170-6>
- Macedonio, G., Costa, A., & Longo, A. (2005). A computer model for volcanic ash fallout and assessment of subsequent hazard. *Computers & Geosciences*, 31(7), 837–845. <https://doi.org/10.1016/j.cageo.2005.01.013>
- Mackie, S., Cashman, K., Ricketts, H., Rust, A., & Watson, M. (Eds.). (2016). *Volcanic ash: Hazard observation*. Elsevier.
- Maeno, F., Kaneko, T., Ichihara, M., Suzuki, Y. J., Yasuda, A., Nishida, K., & Ohminato, T. (2022). Seawater-magma interactions sustained the high column during the 2021 phreatomagmatic eruption of Fukutoku-Oka-no-Ba. *Communications Earth & Environment*, 3(1), 260. <https://doi.org/10.1038/s43247-022-00594-4>
- Maki, M., Takaoka, R., & Iguchi, M. (2021). Characteristics of particle size distributions of falling volcanic ash measured by optical disdrometers at the sakurajima volcano, Japan. *Atmosphere*, 12(5), 601. <https://doi.org/10.3390/atmos12050601>
- Manzella, I., Bonadonna, C., Phillips, J. C., & Monnard, H. (2015). The role of gravitational instabilities in deposition of volcanic ash. *Geology*, 43(3), 211–214. <https://doi.org/10.1130/g36252.1>
- Marchese, F., Falconieri, A., Filizzola, C., Pergola, N., & Tramutoli, V. (2019). Investigating volcanic plumes from Mt. Etna eruptions of December 2015 by means of AVHRR and SEVIRI data. *Sensors*, 19(5), 1174. <https://doi.org/10.3390/s19051174>
- Marchetti, E., Poggi, P., Delle Donne, D., Pistolesi, M., Bonadonna, C., Bagheri, G., et al. (2022). Real-time tephra-fallout accumulation rates and grain-size distributions using ASHER (ASH collector and sizER) disdrometers. *Journal of Volcanology and Geothermal Research*, 429, 107611. <https://doi.org/10.1016/j.jvolgeores.2022.107611>
- Marchetti, E., Ripepe, M., Campus, P., Le Pichon, A., Vergoz, J., Lacanna, G., et al. (2019). Long range infrasound monitoring of Etna volcano. *Scientific Reports*, 9(1), 18015. <https://doi.org/10.1038/s41598-019-54468-5>
- Maréchal, V., Voisin-Plessis, R., Roberts, T. J., Aiuppa, A., Narivelo, H., Hamer, P. D., et al. (2023). Halogen chemistry in volcanic plumes: A 1D framework based on MOCAGE 1D (version R1. 18.1) preparing 3D global chemistry modelling. *Geoscientific Model Development*, 16(10), 2873–2898. <https://doi.org/10.5194/gmd-16-2873-2023>
- Martet, M., Peuch, V. H., Laurent, B., Marticorena, B., & Bergametti, G. (2009). Evaluation of long-range transport and deposition of desert dust with the CTM MOCAGE. *Tellus B: Chemical and Physical Meteorology*, 61(2), 449–463. <https://doi.org/10.1111/j.1600-0889.2008.00413.x>
- Marticorena, B., Bergametti, G., Aumont, B., Callot, Y., N'Doumè, C., & Legrand, M. (1997). Modeling the atmospheric dust cycle: 2. Simulation of Saharan dust sources. *Journal of Geophysical Research*, 102(D4), 4387–4404. <https://doi.org/10.1029/96JD02964>
- Marzano, F. S., Barbieri, S., Vulpiani, G., & Rose, W. I. (2006). Volcanic ash cloud retrieval by ground-based microwave weather radar. *IEEE Transactions on Geoscience and Remote Sensing*, 44(11), 3235–3246. <https://doi.org/10.1109/TGRS.2006.879116>
- Marzano, F. S., Corradini, S., Mereu, L., Kylling, A., Montopoli, M., Cimini, D., et al. (2018). Multisatellite multisensor observations of a sub-Plinian volcanic eruption: The 2015 Calbuco explosive event in Chile. *IEEE Transactions on Geoscience and Remote Sensing*, 56(5), 2597–2612. <https://doi.org/10.1109/TGRS.2017.2769003>
- Marzano, F. S., Lamantea, M., Montopoli, M., Herzog, M., Graf, H., & Cimini, D. (2013). Microwave remote sensing of the 2011 Plinian eruption of the Grímsvötn Icelandic volcano. *Remote Sensing of Environment*, 129, 168–184. <https://doi.org/10.1016/j.rse.2012.11.005>
- Marzano, F. S., Picciotti, E., Montopoli, M., & Vulpiani, G. (2013). Inside volcanic clouds: Remote sensing of ash plumes using microwave weather radars. *Bulletin of the American Meteorological Society*, 94(10), 1567–1586. <https://doi.org/10.1175/BAMS-D-11-00160.1>
- Mastin, L. G. (2007). A user-friendly one-dimensional model for wet volcanic plumes. *Geochemistry, Geophysics, Geosystems*, 8(3), 166. <https://doi.org/10.1029/2006GC001455>
- Mastin, L. G. (2014). Testing the accuracy of a 1-D volcanic plume model in estimating mass eruption rate. *Journal of Geophysical Research: Atmospheres*, 119(5), 2474–2495. <https://doi.org/10.1002/2013JD020604>
- Mastin, L. G., Guffanti, M., Servranckx, R., Webley, P., Barsotti, S., Dean, K., et al. (2009). A multidisciplinary effort to assign realistic source parameters to models of volcanic ash-cloud transport and dispersion during eruptions. *Journal of Volcanology and Geothermal Research*, 186(1–2), 10–21. <https://doi.org/10.1016/j.jvolgeores.2009.01.008>
- Mastin, L. G., Schwaiger, H., Schneider, D. J., Wallace, K. L., Schaefer, J., & Denlinger, R. P. (2013). Injection, transport, and deposition of tephra during event 5 at Redoubt Volcano, 23 March, 2009. *Journal of Volcanology and Geothermal Research*, 259, 201–213. <https://doi.org/10.1016/j.jvolgeores.2012.04.025>
- Mastin, L. G., & Van Eaton, A. R. (2020). Comparing simulations of umbrella-cloud growth and ash transport with observations from Pinatubo, Kelud, and Calbuco Volcanoes. *Atmosphere*, 11(10), 1038. <https://doi.org/10.3390/atmos11101038>
- Mastin, L. G., Van Eaton, A. R., & Cronin, S. J. (2024). Did steam boost the height and growth rate of the giant Hunga eruption plume? *Bulletin of Volcanology*, 86(7), 64. <https://doi.org/10.1007/s00445-024-01749-1>
- Mastin, L. G., Van Eaton, A. R., & Durant, A. J. (2016). Adjusting particle-size distributions to account for aggregation in tephra-deposit model forecasts. *Atmospheric Chemistry and Physics*, 16(14), 9399–9420. <https://doi.org/10.5194/acp-16-9399-2016>
- Matoza, R. S., Fee, D., Green, D. N., Le Pichon, A., Vergoz, J., Haney, M. M., et al. (2018). Local, regional, and remote seismo-acoustic observations of the April 2015 VEI 4 eruption of Calbuco volcano, Chile. *Journal of Geophysical Research: Solid Earth*, 123(5), 3814–3827. <https://doi.org/10.1002/2017JB015182>

- Matoza, R. S., Hedlin, M. A., & Garcés, M. A. (2007). An infrasound array study of Mount St. Helens. *Journal of Volcanology and Geothermal Research*, 160(3–4), 249–262. <https://doi.org/10.1016/j.jvolgeores.2006.10.006>
- Matson, M. (1984). The 1982 El Chichon volcano eruptions—A satellite perspective. *Journal of Volcanology and Geothermal Research*, 23(1–2), 1–10. [https://doi.org/10.1016/0377-0273\(84\)90054-4](https://doi.org/10.1016/0377-0273(84)90054-4)
- McGetchin, T. R., & Ullrich, G. W. (1973). Xenoliths in maars and diatremes with inferences for the Moon, Mars, and Venus. *Journal of Geophysical Research*, 78(11), 1833–1853. <https://doi.org/10.1029/JB078i011p01833>
- McGonigle, A. J. S., Aiuppa, A., Giudice, G., Tamburello, G., Hodson, A. J., & Gurrieri, S. (2008). Unmanned aerial vehicle measurements of volcanic carbon dioxide fluxes. *Geophysical Research Letters*, 35(6), L06303. <https://doi.org/10.1029/2007GL032508>
- McKee, K., Smith, C. M., Reath, K., Snee, E., Maher, S., Matoza, R. S., et al. (2021). Evaluating the state-of-the-art in remote volcanic eruption characterization Part I: Raikoke volcano, Kuril Islands. *Journal of Volcanology and Geothermal Research*, 419, 107354. <https://doi.org/10.1016/j.jvolgeores.2021.107354>
- McNutt, S. R., & Williams, E. R. (2010). Volcanic lightning: Global observations and constraints on source mechanisms. *Bulletin of Volcanology*, 72(10), 1153–1167. <https://doi.org/10.1007/s00445-010-0393-4>
- Mendil, M., Leirens, S., Armand, P., & Duchenne, C. (2022). Hazardous atmospheric dispersion in urban areas: A deep learning approach for emergency pollution forecast. *Environmental Modelling & Software*, 152, 105387. <https://doi.org/10.1016/j.envsoft.2022.105387>
- Mereu, L., Marzano, F. S., Montopoli, M., & Bonadonna, C. (2015). Retrieval of tephra size spectra and mass flow rate from C-band radar during the 2010 Eyjafjallajökull eruption. *Iceland. IEEE Transactions on Geoscience and Remote Sensing*, 53(10), 5644–5660. <https://doi.org/10.1109/TGRS.2015.2427032>
- Mereu, L., Scollo, S., Bonadonna, C., Donnadieu, F., Freret-Lorgeril, V., & Marzano, F. S. (2021). Ground-based remote sensing and uncertainty analysis of the mass eruption rate associated with the 3–5 December 2015 paroxysms of Mt. Etna. *IEEE Journal of Selected Topics in Applied Earth Observations and Remote Sensing*, 15, 504–518. <https://doi.org/10.1109/JSTARS.2021.3133946>
- Mereu, L., Scollo, S., Mori, S., Boselli, A., Leto, G., & Marzano, F. S. (2018). Maximum-likelihood retrieval of volcanic ash concentration and particle size from ground-based scanning lidar. *IEEE Transactions on Geoscience and Remote Sensing*, 56(10), 5824–5842. <https://doi.org/10.1109/TGRS.2018.2826839>
- Mingari, L., Costa, A., Macedonio, G., & Folch, A. (2023). Reconstructing tephra fall deposits via ensemble-based data assimilation techniques. *Geoscientific Model Development*, 16(12), 3459–3478. <https://doi.org/10.5194/gmd-16-3459-2023>
- Mingari, L., Folch, A., Dominguez, L., & Bonadonna, C. (2020). Volcanic ash resuspension in Patagonia: Numerical simulations and observations. *Atmosphere*, 11(9), 977. <https://doi.org/10.3390/atmos11090977>
- Mingari, L., Folch, A., Prata, A. T., Pardini, F., Macedonio, G., & Costa, A. (2022). Data assimilation of volcanic aerosol observations using FALL3D+ PDAF. *Atmospheric Chemistry and Physics*, 22(3), 1773–1792. <https://doi.org/10.5194/acp-22-1773-2022>
- Mingari, L. A., Collini, E. A., Folch, A., Báez, W., Bustos, E., Osoro, M. S., et al. (2017). Numerical simulations of windblown dust over complex terrain: The Fiambalá basin episode in June 2015. *Atmospheric Chemistry and Physics*, 17(11), 6759–6778. <https://doi.org/10.5194/acp-17-6759-2017>
- Miwa, T., Nagai, M., & Kawaguchi, R. (2018). Resuspension of ash after the 2014 phreatic eruption at Ontake volcano, Japan. *Journal of Volcanology and Geothermal Research*, 351, 105–114. <https://doi.org/10.1016/j.jvolgeores.2018.01.003>
- Moiseenko, K. B., & Malik, N. A. (2019). Linear inverse problem for inferring eruption source parameters from sparse ash deposit data as viewed from an atmospheric dispersion modeling perspective. *Bulletin of Volcanology*, 81(3), 1–19. <https://doi.org/10.1007/s00445-019-1281-1>
- Moitra, P., Gonnermann, H. M., Houghton, B. F., & Tiwary, C. S. (2018). Fragmentation and Plinian eruption of crystallizing basaltic magma. *Earth and Planetary Science Letters*, 500, 97–104. <https://doi.org/10.1016/j.epsl.2018.08.003>
- Montesinos, B. M., Luzón, M. T., Sandri, L., Rudy, O., Cheptsov, A., Macedonio, G., et al. (2022). On the feasibility and usefulness of high-performance computing in probabilistic volcanic hazard assessment: An application to tephra hazard from Campi Flegrei. *Frontiers in Earth Science*, 10, 941789. <https://doi.org/10.3389/feart.2022.941789>
- Montopoli, M., Cimini, D., Lamantea, M., Herzog, M., Graf, H. F., & Marzano, F. S. (2013). Microwave radiometric remote sensing of volcanic ash clouds from space: Model and data analysis. *IEEE Transactions on Geoscience and Remote Sensing*, 51(9), 4678–4691. <https://doi.org/10.1109/TGRS.2013.2260343>
- Mori, T., Hashimoto, T., Terada, A., Yoshimoto, M., Kazahaya, R., Shinohara, H., & Tanaka, R. (2016). Volcanic plume measurements using a UAV for the 2014 Mt. Ontake eruption. *Earth Planets and Space*, 68, 1–18. <https://doi.org/10.1186/s40623-016-0418-0>
- Mortier, A., Goloub, P., Podvin, T., Deroo, C., Chaikovskiy, A., Ajtai, N., et al. (2013). Detection and characterization of volcanic ash plumes over Lille during the Eyjafjallajökull eruption. *Atmospheric Chemistry and Physics*, 13(7), 3705–3720. <https://doi.org/10.5194/acp-13-3705-2013>
- Morton, B. R., Taylor, G. I., & Turner, J. S. (1956). Turbulent gravitational convection from maintained and instantaneous sources. *Proceedings of the Royal Society of London. Series A. Mathematical and Physical Sciences*, 234(1196), 1–23. <https://doi.org/10.1098/rspa.1956.0011>
- Mourtada-Bonnefoi, C. C., & Mader, H. M. (2004). Experimental observations of the effect of crystals and pre-existing bubbles on the dynamics and fragmentation of vesiculating flows. *Journal of Volcanology and Geothermal Research*, 129(1–3), 83–97. [https://doi.org/10.1016/S0377-0273\(03\)00233-6](https://doi.org/10.1016/S0377-0273(03)00233-6)
- Mueller, S. B., Kueppers, U., Ametsbichler, J., Cimarelli, C., Merrison, J. P., Poret, M., et al. (2017). Stability of volcanic ash aggregates and break-up processes. *Scientific Reports*, 7(1), 7440. <https://doi.org/10.1038/s41598-017-07927-w>
- Mueller, S. B., Kueppers, U., Ayris, P. M., Jacob, M., & Dingwell, D. B. (2016). Experimental volcanic ash aggregation: Internal structuring of accretionary lapilli and the role of liquid bonding. *Earth and Planetary Science Letters*, 433, 232–240. <https://doi.org/10.1016/j.epsl.2015.11.007>
- Muser, L. O., Hoshyaripour, G. A., Bruckert, J., Horváth, Á., Malinina, E., Wallis, S., et al. (2020). Particle aging and aerosol–radiation interaction affect volcanic plume dispersion: Evidence from the Raikoke 2019 eruption. *Atmospheric Chemistry and Physics*, 20(23), 15015–15036. <https://doi.org/10.5194/acp-20-15015-2020>
- Naeger, A. R., Newchurch, M. J., Moore, T., Chance, K., Liu, X., Alexander, S., et al. (2021). Revolutionary air-pollution applications from future tropospheric emissions: Monitoring of pollution (TEMPO) observations. *Bulletin of the American Meteorological Society*, 102(9), E1735–E1741. <https://doi.org/10.1175/BAMS-D-21-0050.1>
- Nag, A., Murphy, M. J., Schulz, W., & Cummins, K. L. (2015). Lightning locating systems: Insights on characteristics and validation techniques. *Earth and Space Science*, 2(4), 65–93. <https://doi.org/10.1002/2014EA000051>
- National Centers for Environmental Prediction/National Weather Service/NOAA/U.S. Department of Commerce. (2015). NCEP GFS 0.25 degree global forecast grids historical archive [Dataset]. *Research Data Archive at the National Center for Atmospheric Research, Computational and Information Systems Laboratory*. <https://doi.org/10.5065/D65D8PWK>
- Neri, A., Di Muro, A., & Rosi, M. (2002). Mass partition during collapsing and transitional columns by using numerical simulations. *Journal of Volcanology and Geothermal Research*, 115(1–2), 1–18. [https://doi.org/10.1016/S0377-0273\(01\)00304-3](https://doi.org/10.1016/S0377-0273(01)00304-3)

- Newhall, C. G., & Self, S. (1982). The volcanic explosivity index (VEI) an estimate of explosive magnitude for historical volcanism. *Journal of Geophysical Research*, 87(C2), 1231–1238. <https://doi.org/10.1029/JC087iC02p01231>
- Ngan, F., Stein, A., & Draxler, R. (2015). Inline coupling of WRF–HYSPPLIT: Model development and evaluation using tracer experiments. *Journal of Applied Meteorology and Climatology*, 54(6), 1162–1176. <https://doi.org/10.1175/JAMC-D-14-0247.1>
- Ogden, D. E., Glatzmaier, G. A., & Wohletz, K. H. (2008). Effects of vent overpressure on buoyant eruption columns: Implications for plume stability. *Earth and Planetary Science Letters*, 268(3–4), 283–292. <https://doi.org/10.1016/j.epsl.2008.01.014>
- Osman, S., Beckett, F., Rust, A., & Snee, E. (2020). Sensitivity of volcanic ash dispersion modelling to input grain size distribution based on hydromagmatic and magmatic deposits. *Atmosphere*, 11(6), 567. <https://doi.org/10.3390/atmos11060567>
- Osman, S., Thomas, M., Crummy, J., Sharp, A., & Carver, S. (2023). Laboratory tests to understand tephra sliding behaviour on roofs. *Journal of Applied Volcanology*, 12(1), 11. <https://doi.org/10.1186/s13617-023-00137-2>
- Osores, M. S., Folch, A., Collini, E., Villarosa, G., Durant, A. J., Pujol, G., & Viramonte, J. G. (2013). Validation of the FALL3D model for the 2008 Chaitén eruption using field and satellite data. *Andean Geology*, 40(2), 262. <https://doi.org/10.5027/andgeoV40n2-a05>
- Osores, S., Ruiz, J., Folch, A., & Collini, E. (2020). Volcanic ash forecast using ensemble-based data assimilation: An ensemble transform Kalman filter coupled with the FALL3D-7.2 model (ETKF–FALL3D version 1.0). *Geoscientific Model Development*, 13(1), 1–22. <https://doi.org/10.5194/gmd-13-1-2020>
- Oswalt, J. S., Nichols, W., & O'Hara, J. F. (1996). Meteorological observations of the 1991 mount Pinatubo eruption. *Fire and Mud: eruptions and lahars of Mount Pinatubo, Philippines*, 625, 636.
- Palchetti, L., Brindley, H., Bantges, R., Buehler, S. A., Camy-Peyret, C., Carli, B., et al. (2020). FORUM: Unique far-infrared satellite observations to better understand how Earth radiates energy to space. *Bulletin of the American Meteorological Society*, 101(12), E2030–E2046. <https://doi.org/10.1175/BAMS-D-19-0322.1>
- Pankhurst, M. J., Scarrow, J. H., Barbee, O. A., Hickey, J., Coldwell, B. C., Rollinson, G. K., et al. (2022). Rapid response petrology for the opening eruptive phase of the 2021 Cumbre Vieja eruption, La Palma, Canary Islands. *Volcanica*, 5(1), 1–10. <https://doi.org/10.30909/vol.05.01.0110>
- Pardini, F., Barsotti, S., Bonadonna, C., de' Michieli Vitturi, M., Folch, A., Mastin, L., et al. (2024). [Simulation] dynamics, monitoring and forecasting of tephra in the atmosphere [Dataset]. *Zenodo*. <https://doi.org/10.5281/zenodo.13316791>
- Pardini, F., Corradini, S., Costa, A., Esposti Ongaro, T., Merucci, L., Neri, A., et al. (2020). Ensemble-based data assimilation of volcanic ash clouds from satellite observations: Application to the 24 December 2018 Mt. Etna explosive eruption. *Atmosphere*, 11(4), 359. <https://doi.org/10.3390/atmos11040359>
- Pardini, F., de' Michieli Vitturi, M., Andronico, D., Esposti Ongaro, T., Cristaldi, A., & Neri, A. (2022). Real-time probabilistic assessment of volcanic hazard for tephra dispersal and fallout at Mt. Etna: The 2021 lava fountain episodes. *Bulletin of Volcanology*, 85(1), 6. <https://doi.org/10.1007/s00445-022-01614-z>
- Pardini, F., Spanu, A., de' Michieli Vitturi, M., Salvetti, M. V., & Neri, A. (2016). Grain size distribution uncertainty quantification in volcanic ash dispersal and deposition from weak plumes. *Journal of Geophysical Research: Solid Earth*, 121(2), 538–557. <https://doi.org/10.1002/2015JB012536>
- Patrick, M. R. (2007). Dynamics of Strombolian ash plumes from thermal video: Motion, morphology, and air entrainment. *Journal of Geophysical Research*, 112(B6), B06202. <https://doi.org/10.1029/2006JB004387>
- Patrick, M. R., Harris, A. J., Ripepe, M., Dehn, J., Rothery, D. A., & Calvari, S. (2007). Strombolian explosive styles and source conditions: Insights from thermal (FLIR) video. *Bulletin of Volcanology*, 69(7), 769–784. <https://doi.org/10.1007/s00445-006-0107-0>
- Pavolonis, M. J. (2010). Advances in extracting cloud composition information from spaceborne infrared radiances—A robust alternative to brightness temperatures. Part I: Theory. *Journal of Applied Meteorology and Climatology*, 49(9), 1992–2012. <https://doi.org/10.1175/2010JAMC2433.1>
- Pavolonis, M. J., Feltz, W. F., Heidinger, A. K., & Gallina, G. M. (2006). A daytime complement to the reverse absorption technique for improved automated detection of volcanic ash. *Journal of Atmospheric and Oceanic Technology*, 23(11), 1422–1444. <https://doi.org/10.1175/JTECH1926.1>
- Pavolonis, M. J., Heidinger, A. K., & Sieglaff, J. (2013). Automated retrievals of volcanic ash and dust cloud properties from upwelling infrared measurements. *Journal of Geophysical Research: Atmospheres*, 118(3), 1436–1458. <https://doi.org/10.1002/jgrd.50173>
- Pavolonis, M. J., Sieglaff, J., & Cintineo, J. (2015a). Spectrally enhanced cloud objects—A generalized framework for automated detection of volcanic ash and dust clouds using passive satellite measurements: 1. Multispectral analysis. *Journal of Geophysical Research: Atmospheres*, 120(15), 7813–7841. <https://doi.org/10.1002/2014JD022968>
- Pavolonis, M. J., Sieglaff, J., & Cintineo, J. (2015b). Spectrally enhanced cloud objects—A generalized framework for automated detection of volcanic ash and dust clouds using passive satellite measurements: 2. Cloud object analysis and global application. *Journal of Geophysical Research: Atmospheres*, 120(15), 7842–7870. <https://doi.org/10.1002/2014JD022969>
- Pavolonis, M. J., Sieglaff, J., & Cintineo, J. (2018). Automated detection of explosive volcanic eruptions using satellite-derived cloud vertical growth rates. *Earth and Space Science*, 5(12), 903–928. <https://doi.org/10.1029/2018EA000410>
- Pelley, R. E., Cooke, M. C., Manning, A. J., Thomson, D. J., Witham, C. S., & Hort, M. C. (2015). Initial implementation of an inversion technique for estimating volcanic ash source parameters in near real time using satellite retrievals; forecasting research technical report 604; Met Office: Exeter, UK.
- Pelley, R. E., Thomson, D. J., Webster, H. N., Cooke, M. C., Manning, A. J., Witham, C. S., & Hort, M. C. (2021). A near-real-time method for estimating volcanic ash emissions using satellite retrievals. *Atmosphere*, 12(12), 1573. <https://doi.org/10.3390/atmos12121573>
- Pergola, N., Tramutoli, V., Marchese, F., Scaffidi, I., & Lacava, T. (2004). Improving volcanic ash cloud detection by a robust satellite technique. *Remote Sensing of Environment*, 90(1), 1–22. <https://doi.org/10.1016/j.rse.2003.11.014>
- Petäjä, T., Laakso, L., Grönholm, T., Launiainen, S., Evele-Peltoniemi, I., Virkkula, A., et al. (2012). In-situ observations of Eyjafjallajökull ash particles by hot-air balloon. *Atmospheric Environment*, 48, 104–112. <https://doi.org/10.1016/j.atmosenv.2011.08.046>
- Petersen, G. N., Björnsson, H., & Arason, P. (2012). The impact of the atmosphere on the Eyjafjallajökull 2010 eruption plume. *Journal of Geophysical Research*, 117(D20), D00U07. <https://doi.org/10.1029/2011JD016762>
- Petracca, I., De Santis, D., Picchiani, M., Corradini, S., Guerrieri, L., Prata, F., et al. (2022). Volcanic cloud detection using Sentinel-3 satellite data by means of neural networks: The Raikoke 2019 eruption test case. *Atmospheric Measurement Techniques*, 15(24), 7195–7210. <https://doi.org/10.5194/amt-15-7195-2022>
- Pfeffer, M. A., Bergsson, B., Barsotti, S., Stefánsdóttir, G., Galle, B., Arellano, S., et al. (2018). Ground-based measurements of the 2014–2015 Holuhraun volcanic cloud (Iceland). *Geosciences*, 8(1), 29. <https://doi.org/10.3390/geosciences8010029>
- Pfeiffer, T., Costa, A., & Macedonio, G. (2005). A model for the numerical simulation of tephra fall deposits. *Journal of Volcanology and Geothermal Research*, 140(4), 273–294. <https://doi.org/10.1016/j.jvolgeores.2004.09.001>

- Picchiani, M., Chini, M., Corradini, S., Merucci, L., Sellitto, P., Del Frate, F., & Stramondo, S. (2011). Volcanic ash detection and retrievals using MODIS data by means of neural networks. *Atmospheric Measurement Techniques*, 4(12), 2619–2631. <https://doi.org/10.5194/amt-4-2619-2011>
- Pieri, D., Diaz, J. A., Bland, G., Fladeland, M., Madrigal, Y., Corrales, E., et al. (2013). In situ observations and sampling of volcanic emissions with NASA and UCR unmanned aircraft, including a case study at Turrialba Volcano, Costa Rica. *Geological Society, London, Special Publications*, 380(1), 321–352. <https://doi.org/10.1144/SP380.13>
- Piontek, D., Bugliaro, L., Kar, J., Schumann, U., Marengo, F., Plu, M., & Voigt, C. (2021). The new volcanic ash satellite retrieval VACOS using MSG/SEVIRI and artificial neural networks: 2. Validation. *Remote Sensing*, 13(16), 3128. <https://doi.org/10.3390/rs13163128>
- Piontek, D., Bugliaro, L., Schmidl, M., Zhou, D. K., & Voigt, C. (2021). The new volcanic ash satellite retrieval vacos using msg/seviri and artificial neural networks: 1. Development. *Remote Sensing*, 13(16), 3112. <https://doi.org/10.3390/rs13163112>
- Piscini, A., Corradini, S., Marchese, F., Merucci, L., Pergola, N., & Tramutoli, V. (2011). Volcanic ash cloud detection from space: A comparison between the RSTASH technique and the water vapour corrected BTM procedure. *Geomatics, Natural Hazards and Risk*, 2(3), 263–277. <https://doi.org/10.1080/19475705.2011.568069>
- Piscini, A., Picchiani, M., Chini, M., Corradini, S., Merucci, L., Del Frate, F., & Stramondo, S. (2014). A neural network approach for the simultaneous retrieval of volcanic ash parameters and SO<sub>2</sub> using MODIS data. *Atmospheric Measurement Techniques*, 7(12), 4023–4047. <https://doi.org/10.5194/amt-7-4023-2014>
- Pisso, I., Sollum, E., Grythe, H., Kristiansen, N. I., Cassiani, M., Eckhardt, S., et al. (2019). The Lagrangian particle dispersion model FLEXPART version 10.4. *Geoscientific Model Development*, 12(12), 4955–4997. <https://doi.org/10.5194/gmd-12-4955-2019>
- Platt, C. M. R., & Prata, A. J. (1993). Nocturnal effects in the retrieval of land surface temperatures from satellite measurements. *Remote Sensing of Environment*, 45(2), 127–136. [https://doi.org/10.1016/0034-4257\(93\)90037-X](https://doi.org/10.1016/0034-4257(93)90037-X)
- Plu, M., Scherllin-Pirscher, B., Arias, D. A., Baro, R., Bigeard, G., Bugliaro, L., et al. (2021). An ensemble of state-of-the-art ash dispersion models: Towards probabilistic forecasts to increase the resilience of air traffic against volcanic eruptions. *Natural Hazards and Earth System Sciences*, 21(10), 2973–2992. <https://doi.org/10.5194/nhess-21-2973-2021>
- Podglajen, A., Le Pichon, A., Garcia, R. F., G erier, S., Millet, C., Bedka, K., et al. (2022). Stratospheric balloon observations of infrasound waves from the 15 January 2022 Hunga eruption, Tonga. *Geophysical Research Letters*, 49(19), e2022GL100833. <https://doi.org/10.1029/2022gl100833>
- Poli, P., & Shapiro, N. M. (2022). Rapid characterization of large volcanic eruptions: Measuring the impulse of the Hunga Tonga Ha'apai explosion from teleseismic waves. *Geophysical Research Letters*, 49(8), e2022GL098123. <https://doi.org/10.1029/2022GL098123>
- Pollack, J. B., Toon, O. B., & Khare, B. N. (1973). Optical properties of some terrestrial rocks and glasses. *Icarus*, 19(3), 372–389. [https://doi.org/10.1016/0019-1035\(73\)90115-2](https://doi.org/10.1016/0019-1035(73)90115-2)
- Pollastri, S., Rossi, E., & Bonadonna, C. (2022). First field evidence of the electrical multipolar nature of volcanic aggregates. *Science Advances*, 8(46), eabo7380. <https://doi.org/10.1126/sciadv.abo7380>
- Pope, S. B. (2000). *Turbulent flows*. Cambridge University Press.
- Poret, M., Corradini, S., Merucci, L., Costa, A., Andronico, D., Montopoli, M., et al. (2018). Reconstructing volcanic plume evolution integrating satellite and ground-based data: Application to the 23 November 2013 Etna eruption. *Atmospheric Chemistry and Physics*, 18(7), 4695–4714. <https://doi.org/10.5194/acp-18-4695-2018>
- Potts, R. J., & Ebert, E. E. (1996). On the detection of volcanic ash in NOAA AVHRR infrared satellite imagery. In *8th Australasian remote sensing conference* (pp. 25–29).
- Pouget, S., Bursik, M., Johnson, C. G., Hogg, A. J., Phillips, J. C., & Sparks, R. S. J. (2016). Interpretation of umbrella cloud growth and morphology: Implications for flow regimes of short-lived and long-lived eruptions. *Bulletin of Volcanology*, 78, 1–19. <https://doi.org/10.1007/s00445-015-0993-0>
- Pouget, S., Bursik, M., Webley, P., Dehn, J., & Pavolonis, M. (2013). Estimation of eruption source parameters from umbrella cloud or downwind plume growth rate. *Journal of Volcanology and Geothermal Research*, 258, 100–112. <https://doi.org/10.1016/j.jvolgeores.2013.04.002>
- Poullidis, A. P., Phillips, J. C., Renfrew, I. A., Barclay, J., Hogg, A., Jenkins, S. F., et al. (2018). Meteorological controls on local and regional volcanic ash dispersal. *Scientific Reports*, 8(1), 6873. <https://doi.org/10.1038/s41598-018-24651-1>
- Prabhakara, C., Fraser, R. S., Dalu, G., Wu, M. L. C., Curran, R. J., & Styles, T. (1988). Thin cirrus clouds: Seasonal distribution over oceans deduced from Nimbus-4 IRIS. *Journal of Applied Meteorology and Climatology*, 27(4), 379–399. [https://doi.org/10.1175/1520-0450\(1988\)027<0379:TCCSDO>2.0.CO;2](https://doi.org/10.1175/1520-0450(1988)027<0379:TCCSDO>2.0.CO;2)
- Prata, A. J. (1989a). Infrared radiative transfer calculations for volcanic ash clouds. *Geophysical Research Letters*, 16(11), 1293–1296. <https://doi.org/10.1029/GL016i011p01293>
- Prata, A. J. (1989b). Observations of volcanic ash clouds in the 10–12 μm window using AVHRR/2 data. *International Journal of Remote Sensing*, 10(4–5), 751–761. <https://doi.org/10.1080/01431168908903916>
- Prata, A. J. (2009). Satellite detection of hazardous volcanic clouds and the risk to global air traffic. *Natural Hazards*, 51(2), 303–324. <https://doi.org/10.1007/s11069-008-9273-z>
- Prata, A. J., & Barton, I. J. (1994). Detection and discrimination of volcanic clouds by infrared radiometry—I: Theory. In T. J. Casadevall (Ed.), *Volcanic ash and aviation safety: Proceedings of the first international symposium on volcanic ash and aviation safety, No. 2047* (pp. 305–311). US Government Printing Office.
- Prata, A. J., Barton, I. J., Johnson, R. W., Kamo, K., & Kingwell, J. (1991). Hazard from volcanic ash. *Nature*, 354(6348), 25. <https://doi.org/10.1038/354025a0>
- Prata, A. J., & Bernardo, C. (2009). Retrieval of volcanic ash particle size, mass and optical depth from a ground-based thermal infrared camera. *Journal of Volcanology and Geothermal Research*, 186(1–2), 91–107. <https://doi.org/10.1016/j.jvolgeores.2009.02.007>
- Prata, A. J., & Grant, I. F. (2001). Retrieval of microphysical and morphological properties of volcanic ash plumes from satellite data: Application to Mt Ruapehu, New Zealand. *Quarterly Journal of the Royal Meteorological Society*, 127(576), 2153–2179. <https://doi.org/10.1002/qj.49712757615>
- Prata, A. J., & Prata, A. T. (2012). Eyjafjallaj kull volcanic ash concentrations determined using Spin Enhanced Visible and Infrared Imager measurements. *Journal of Geophysical Research*, 117(D20), D00U23. <https://doi.org/10.1029/2011JD016800>
- Prata, A. T. (2016). Remote sensing of volcanic eruptions. In *Plate boundaries and natural hazards, American Geophysical Union (AGU)* (pp. 289–322). <https://doi.org/10.1002/9781119054146.ch14>
- Prata, A. T., Folch, A., Prata, A. J., Biondi, R., Brenot, H., Cimarelli, C., et al. (2020). Anak Krakatau triggers volcanic freezer in the upper troposphere. *Scientific Reports*, 10(1), 3584. <https://doi.org/10.1038/s41598-020-60465-w>

- Prata, A. T., Grainger, R. G., Taylor, I. A., Povey, A. C., Proud, S. R., & Poulsen, C. A. (2022). Uncertainty-bounded estimates of ash cloud properties using the ORAC algorithm: Application to the 2019 Raikoke eruption. *Atmospheric Measurement Techniques*, *15*(20), 5985–6010. <https://doi.org/10.5194/amt-15-5985-2022>
- Prata, A. T., Mingari, L., Folch, A., Macedonio, G., & Costa, A. (2021). FALL3D-8.0: A computational model for atmospheric transport and deposition of particles, aerosols and radionuclides—Part 2: Model validation. *Geoscientific Model Development*, *14*(1), 409–436. <https://doi.org/10.5194/gmd-14-409-2021>
- Prata, A. T., Siems, S. T., & Manton, M. J. (2015). Quantification of volcanic cloud top heights and thicknesses using A-train observations for the 2008 Chaitén eruption. *Journal of Geophysical Research: Atmospheres*, *120*(7), 2928–2950. <https://doi.org/10.1002/2014JD022399>
- Prata, A. T., Young, S. A., Siems, S. T., & Manton, M. J. (2017). Lidar ratios of stratospheric volcanic ash and sulfate aerosols retrieved from CALIOP measurements. *Atmospheric Chemistry and Physics*, *17*(13), 8599–8618. <https://doi.org/10.5194/acp-17-8599-2017>
- Prata, F. (2020). Detection and avoidance of atmospheric aviation hazards using infrared spectroscopic imaging. *Remote Sensing*, *12*(14), 2309. <https://doi.org/10.3390/rs12142309>
- Prata, F., & Lynch, M. (2019). Passive Earth observations of volcanic clouds in the atmosphere. *Atmosphere*, *10*(4), 199. <https://doi.org/10.3390/atmos10040199>
- Prata, F., & Rose, B. (2015). Volcanic ash hazards to aviation. In *The encyclopedia of volcanoes* (pp. 911–934). Academic Press. <https://doi.org/10.1016/B978-0-12-385938-9.00052-3>
- Prata, F., Woodhouse, M., Huppert, H. E., Prata, A., Thordarson, T., & Carn, S. (2017). Atmospheric processes affecting the separation of volcanic ash and SO<sub>2</sub> in volcanic eruptions: Inferences from the may 2011 Grímsvötn eruption. *Atmospheric Chemistry and Physics*, *17*, 10709–10732. <https://doi.org/10.5194/acp-17-10709-2017>
- Prata, G. S., Ventress, L. J., Carboni, E., Mather, T. A., Grainger, R. G., & Pyle, D. M. (2019). A new parameterization of volcanic ash complex refractive index based on NBO/T and SiO<sub>2</sub> content. *Journal of Geophysical Research: Atmospheres*, *124*(3), 1779–1797. <https://doi.org/10.1029/2018JD028679>
- Pritchard, M. E., Poland, M., Reath, K., Andrews, B., Bagnardi, M., Biggs, J., et al. (2022). *Optimizing satellite resources for the global assessment and mitigation of volcanic hazards—Suggestions from the USGS Powell center volcano remote sensing working group (no. 2022-5116)*. US Geological Survey. Retrieved from <http://pubs.er.usgs.gov/publication/sir20225116>
- Proud, S. R., Prata, A. T., & Schmauß, S. (2022). The January 2022 eruption of Hunga Tonga-Hunga Ha'apai volcano reached the mesosphere. *Science*, *378*(6619), 554–557. <https://doi.org/10.1126/science.abo4076>
- Pyle, D. M., Mather, T. A., & Biggs, J. (2013). Remote sensing of volcanoes and volcanic processes: Integrating observation and modelling—introduction. *Geological Society, London, Special Publications*, *380*(1), 1–13. <https://doi.org/10.1144/SP380.14>
- Ramkrishna, D., & Singh, M. R. (2014). Population balance modeling: Current status and future prospects. *Annual Review of Chemical and Biomolecular Engineering*, *5*(1), 123–146. <https://doi.org/10.1146/annurev-chembioeng-060713-040241>
- Rampino, M. R., & Self, S. (1992). Volcanic winter and accelerated glaciation following the Toba super-eruption. *Nature*, *359*(6390), 50–52. <https://doi.org/10.1038/359050a0>
- Re, G., Corsaro, R. A., D'Orlando, C., & Pompilio, M. (2021). Petrological monitoring of active volcanoes: A review of existing procedures to achieve best practices and operative protocols during eruptions. *Journal of Volcanology and Geothermal Research*, *419*, 107365. <https://doi.org/10.1016/j.jvolgeores.2021.107365>
- Reckziegel, F., Bustos, E., Mingari, L., Báez, W., Villarosa, G., Folch, A., et al. (2016). Forecasting volcanic ash dispersal and coeval resuspension during the April–May 2015 Calbuco eruption. *Journal of Volcanology and Geothermal Research*, *321*, 44–57. <https://doi.org/10.1016/j.jvolgeores.2016.04.033>
- Reckziegel, F., Folch, A., & Viramonte, J. (2019). ATLAS-1.0: Atmospheric Lagrangian dispersion model for tephra transport and deposition. *Computers & Geosciences*, *131*, 41–51. <https://doi.org/10.1016/j.cageo.2019.05.008>
- Reed, B. E., Peters, D. M., McPheat, R., & Grainger, R. G. (2018). The complex refractive index of volcanic ash aerosol retrieved from spectral mass extinction. *Journal of Geophysical Research: Atmospheres*, *123*(2), 1339–1350. <https://doi.org/10.1002/2017JD027362>
- Ricou, F. P., & Spalding, D. B. (1961). Measurements of entrainment by axisymmetrical turbulent jets. *Journal of Fluid Mechanics*, *11*(1), 21–32. <https://doi.org/10.1017/S0022112061000834>
- Rieger, D., Bangert, M., Bischoff-Gauss, I., Förstner, J., Lundgren, K., Reinert, D., et al. (2015). ICON-ART 1.0—A new online-coupled model system from the global to regional scale. *Geoscientific Model Development Discussions*, *8*(1), 567–614. <https://doi.org/10.5194/gmd-8-1659-2015>
- Ripepe, M., Bonadonna, C., Folch, A., Delle Donne, D., Lacanna, G., Marchetti, E., & Höskuldsson, A. (2013). Ash-plume dynamics and eruption source parameters by infrasound and thermal imagery: The 2010 Eyjafjallajökull eruption. *Earth and Planetary Science Letters*, *366*, 112–121. <https://doi.org/10.1016/j.epsl.2013.02.005>
- Robock, A., & Matson, M. (1983). Circumglobal transport of the El Chichón volcanic dust cloud. *Science*, *221*(4606), 195–197. <https://doi.org/10.1126/science.221.4606.195>
- Rocha-Lima, A., Martins, J. V., Remer, L. A., Krotkov, N. A., Tabacniks, M. H., Ben-Ami, Y., & Artaxo, P. (2014). Optical, microphysical and compositional properties of the Eyjafjallajökull volcanic ash. *Atmospheric Chemistry and Physics*, *14*(19), 10649–10661. <https://doi.org/10.5194/acp-14-10649-2014>
- Rodgers, C. D. (1976). Retrieval of atmospheric temperature and composition from remote measurements of thermal radiation. *Reviews of Geophysics*, *14*(4), 609–624. <https://doi.org/10.1029/RG014i004p00609>
- Rodgers, C. D. (2000). *Inverse methods for atmospheric sounding: Theory and practice* (Vol. 2). World scientific. <https://doi.org/10.1142/3171>
- Romeo, F., Mereu, L., Scollo, S., Papa, M., Corradini, S., Merucci, L., & Marzano, F. S. (2023). Volcanic cloud detection and retrieval using satellite multisensor observations. *Remote Sensing*, *15*(4), 888. <https://doi.org/10.3390/rs15040888>
- Romero, J. E., Morgavi, D., Arzilli, F., Daga, R., Caselli, A., Reckziegel, F., et al. (2016). Eruption dynamics of the 22–23 April 2015 Calbuco volcano (southern Chile): Analyses of tephra fall deposits. *Journal of Volcanology and Geothermal Research*, *317*, 15–29. <https://doi.org/10.1016/j.jvolgeores.2016.02.027>
- Rose, W. I., Bluth, G. J., Schneider, D. J., Ernst, G. G., Riley, C. M., Henderson, L. J., & McGimsey, R. G. (2001). Observations of volcanic clouds in their first few days of atmospheric residence: The 1992 eruptions of Crater Peak, Mount Spurr volcano, Alaska. *The Journal of Geology*, *109*(6), 677–694. <https://doi.org/10.1086/323189>
- Rose, W. I., Delene, D. J., Schneider, D. J., Bluth, G. J. S., Krueger, A. J., Sprod, I., et al. (1995). Ice in the 1994 Rabaul eruption cloud: Implications for volcano hazard and atmospheric effects. *Nature*, *375*(6531), 477–479. <https://doi.org/10.1038/375477a0>
- Rose, W. I., & Durant, A. J. (2009). Fine ash content of explosive eruptions. *Journal of Volcanology and Geothermal Research*, *186*(1–2), 32–39. <https://doi.org/10.1016/j.jvolgeores.2009.01.010>

- Rose, W. I., & Durant, A. J. (2011). Fate of volcanic ash: Aggregation and fallout. *Geology*, 39(9), 895–896. <https://doi.org/10.1130/focus092011.1>
- Rose, W. I., Kostinski, A. B., & Kelley, L. (1995). Real-time C-band radar observations of 1992 eruption C. In *The 1992 eruptions of Crater Peak Vent, Mount Spurr volcano, Alaska*, (2139) (p. 19).
- Rosi, M., Pistolesi, M., Bertagnini, A., Landi, P., Pompilio, M., & Di Roberto, A. (2013). Chapter 14 Stromboli volcano, Aeolian islands (Italy): Present eruptive activity and hazards. *Geological Society, London, Memoirs*, 37(1), 473–490. <https://doi.org/10.1144/M37.14>
- Rossi, E., Bagheri, G., Beckett, F., & Bonadonna, C. (2021). The fate of volcanic ash: Premature or delayed sedimentation? *Nature Communications*, 12(1), 1303. <https://doi.org/10.1038/s41467-021-21568-8>
- Rowell, C. R., Jellinek, A. M., Hajimirza, S., & Aubry, T. J. (2022). External surface water influence on explosive eruption dynamics, with implications for stratospheric sulfur delivery and volcano-climate feedback. *Frontiers in Earth Science*, 10, 788294. <https://doi.org/10.3389/feart.2022.788294>
- Sahetapy-Engel, S. T., & Harris, A. J. (2009). Thermal-image-derived dynamics of vertical ash plumes at Santiaguito volcano, Guatemala. *Bulletin of Volcanology*, 71(7), 827–830. <https://doi.org/10.1007/s00445-009-0284-8>
- Sawada, Y. (1983). Analysis of eruption clouds by the 1981 eruptions of Alaid and Pagan volcanos with GMS images. *Papers in Meteorology and Geophysics*, 34(4), 307–324. <https://doi.org/10.2467/mripapers.34.307>
- Sawada, Y. (1987). Study on analyses of volcanic eruptions based on eruption cloud image data obtained by the geostationary meteorological satellite (GMS). *Technical Report of the Meteorological Research Institute*, 22, 1–335.
- Sawada, Y. (1996). Detection of explosive eruptions and regional tracking of volcanic ash clouds with geostationary meteorological satellite (GMS). In *Monitoring and mitigation of volcano hazards*. Springer. [https://doi.org/10.1007/978-3-642-80087-0\\_9](https://doi.org/10.1007/978-3-642-80087-0_9)
- Schellenberg, B., Richardson, T., Watson, M., Greatwood, C., Clarke, R., Thomas, R., et al. (2019). Remote sensing and identification of volcanic plumes using fixed-wing UAVs over Volcán de Fuego, Guatemala. *Journal of Field Robotics*, 36(7), 1192–1211. <https://doi.org/10.1002/rob.21896>
- Schneider, D. J., & Hoblitt, R. P. (2013). Doppler weather radar observations of the 2009 eruption of Redoubt Volcano, Alaska. *Journal of Volcanology and Geothermal Research*, 259, 133–144. <https://doi.org/10.1016/j.jvolgeores.2012.11.004>
- Schneider, D. J., Rose, W. I., Coke, L. R., Bluth, G. J., Sprod, I. E., & Krueger, A. J. (1999). Early evolution of a stratospheric volcanic eruption cloud as observed with TOMS and AVHRR. *Journal of Geophysical Research*, 104(D4), 4037–4050. <https://doi.org/10.1029/1998JD200073>
- Schneider, D. J., Rose, W. I., & Kelley, L. (1995). Tracking of 1992 eruption clouds from Crater Peak vent of Mount Spurr volcano, Alaska, using AVHRR. *US Geological Survey Bulletin*, 2139, 27–36.
- Schultz, C. J., Andrews, V. P., Genareau, K. D., & Naeger, A. R. (2020). Observations of lightning in relation to transitions in volcanic activity during the 3 June 2018 Fuego Eruption. *Scientific Reports*, 10(1), 18015. <https://doi.org/10.1038/s41598-020-74576-x>
- Schumann, U., Weinzierl, B., Reitebuch, O., Schlager, H., Minikin, A., Forster, C., et al. (2011). Airborne observations of the Eyjafjalla volcano ash cloud over Europe during air space closure in April and May 2010. *Atmospheric Chemistry and Physics*, 11(5), 2245–2279. <https://doi.org/10.5194/acp-11-2245-2011>
- Schwaiger, H. F., Denlinger, R. P., & Mastin, L. G. (2012). Ash3d: A finite-volume, conservative numerical model for ash transport and tephra deposition. *Journal of Geophysical Research*, 117(B4), B04204. <https://doi.org/10.1029/2011JB008968>
- Scollo, S., Bonadonna, C., & Manzella, I. (2017). Settling-driven gravitational instabilities associated with volcanic clouds: New insights from experimental investigations. *Bulletin of Volcanology*, 79(6), 1–14. <https://doi.org/10.1007/s00445-017-1124-x>
- Scollo, S., Boselli, A., Corradini, S., Leto, G., Guerrieri, L., Merucci, L., et al. (2020). Multi-sensor analysis of a weak and long-lasting volcanic plume emission. *Remote Sensing*, 12(23), 3866. <https://doi.org/10.3390/rs12233866>
- Scollo, S., Coltelli, M., Prodi, F., Folegani, M., & Natali, S. (2005). Terminal settling velocity measurements of volcanic ash during the 2002–2003 Etna eruption by an X-band microwave rain gauge disdrometer. *Geophysical Research Letters*, 32(10), L10302. <https://doi.org/10.1029/2004GL022100>
- Scollo, S., Del Carlo, P., & Coltelli, M. (2007). Tephra fallout of 2001 Etna flank eruption: Analysis of the deposit and plume dispersion. *Journal of Volcanology and Geothermal Research*, 160(1–2), 147–164. <https://doi.org/10.1016/j.jvolgeores.2006.09.007>
- Scollo, S., Prestifilippo, M., Bonadonna, C., Cioni, R., Corradini, S., Degruyter, W., et al. (2019). Near-real-time tephra fallout assessment at Mt. Etna, Italy. *Remote Sensing*, 11(24), 2987. <https://doi.org/10.3390/rs11242987>
- Scollo, S., Prestifilippo, M., Pecora, E., Corradini, S., Merucci, L., Spata, G., & Coltelli, M. (2014). Eruption column height estimation of the 2011–2013 Etna lava fountains. *Annals of Geophysics*, 57(2), S0214. <https://doi.org/10.4401/ag-6396>
- Scollo, S., Prestifilippo, M., Spata, G., D'Agostino, M., & Coltelli, M. (2009). Monitoring and forecasting Etna volcanic plumes. *Natural Hazards and Earth System Sciences*, 9(5), 1573–1585. <https://doi.org/10.5194/nhess-9-1573-2009>
- Scollo, S., Tarantola, S., Bonadonna, C., Coltelli, M., & Saltelli, A. (2008). Sensitivity analysis and uncertainty estimation for tephra dispersal models. *Journal of Geophysical Research*, 113(B6), 1–17. <https://doi.org/10.1029/2006JB004864>
- Sears, T. M., Thomas, G. E., Carboni, E., Smith, A. J., & Grainger, R. G. (2013). SO<sub>2</sub> as a possible proxy for volcanic ash in aviation hazard avoidance. *Journal of Geophysical Research: Atmospheres*, 118(11), 5698–5709. <https://doi.org/10.1002/jgrd.50505>
- Seftor, C. J., Hsu, N. C., Herman, J. R., Bhartia, P. K., Torres, O., Rose, W. I., et al. (1997). Detection of volcanic ash clouds from Nimbus 7/total ozone mapping spectrometer. *Journal of Geophysical Research*, 102(D14), 16749–16759. <https://doi.org/10.1029/97JD00925>
- Seibert, P. (2000). Inverse modelling of sulfur emissions in Europe based on trajectories. *Inverse Methods in Global Biogeochemical Cycles*, 114, 147–154. <https://doi.org/10.1029/GM114p0147>
- Settle, M. (1978). Volcanic eruption clouds and the thermal power output of explosive eruptions. *Journal of Volcanology and Geothermal Research*, 3(3–4), 309–324. [https://doi.org/10.1016/0377-0273\(78\)90041-0](https://doi.org/10.1016/0377-0273(78)90041-0)
- Shao, Y., Raupach, M. R., & Findlater, P. A. (1993). Effect of saltation bombardment on the entrainment of dust by wind. *Journal of Geophysical Research*, 98(D7), 12719–12726. <https://doi.org/10.1029/93JD00396>
- Shimbori, T., & Ishii, K. (2021). Design of the Japan Meteorological Agency atmospheric transport model. *Technical Report MRI*, 84, 146.
- Siebert, L., Cottrell, E., Venzke, E., & Andrews, B. (2015). Earth's volcanoes and their eruptions: An overview. In *The encyclopedia of volcanoes* (pp. 239–255). <https://doi.org/10.1016/B978-0-12-385938-9.00012-2>
- Sigurdsson, H., Houghton, B., McNutt, S., Rymer, H., & Stix, J. (2015). *The encyclopedia of volcanoes*. Elsevier.
- Simionato, R., Jarvis, P. A., Rossi, E., & Bonadonna, C. (2022). PlumeTraP: A new MATLAB-based algorithm to detect and parametrize volcanic plumes from visible-wavelength images. *Remote Sensing*, 14(7), 1766. <https://doi.org/10.3390/rs14071766>
- Smith, C. M., Gaudin, D., Van Eaton, A. R., Behnke, S. A., Reader, S., Thomas, R. J., et al. (2021). Impulsive volcanic plumes generate volcanic lightning and vent discharges: A statistical analysis of Sakurajima volcano in 2015. *Geophysical Research Letters*, 48(11), e2020GL092323. <https://doi.org/10.1029/2020GL092323>

- Smith, C. M., Van Eaton, A. R., Said, R., & Holzworth, R. H. (2018). Volcanic lightning as a monitoring tool during the 2016–2017 eruption of Bogoslof volcano, AK. In *25th international lightning detect conference & 7th international lightning meteorology conference* (pp. 1–5).
- Smoluchowski, M. (1917). Versuch einer mathematischen Theorie der Koagulationskinetik kolloider Lösungen. *Zeitschrift für Physikalische Chemie*, *92*, 128–168.
- Soda, R. (1961). Infrared absorption spectra of quartz and some other silica modification. *Bulletin of the Chemical Society of Japan*, *34*(10), 1491–1495. <https://doi.org/10.1246/bcsj.34.1491>
- Solovitz, S. A., & Mastin, L. G. (2009). Experimental study of near-field air entrainment by subsonic volcanic jets. *Journal of Geophysical Research*, *114*(B10), B10203. <https://doi.org/10.1029/2009JB006298>
- Solovitz, S. A., Mastin, L. G., & Saffaraval, F. (2011). Experimental study of near-field entrainment of moderately overpressured jets. *Journal of Fluids Engineering*, *133*(5), 051304. <https://doi.org/10.1115/1.4004083>
- Song, W., Lavallée, Y., Hess, K. U., Kueppers, U., Cimarelli, C., & Dingwell, D. B. (2016). Volcanic ash melting under conditions relevant to ash turbine interactions. *Nature Communications*, *7*(1), 10795. <https://doi.org/10.1038/ncomms10795>
- Spampinato, L., Calvari, S., Oppenheimer, C., & Boschi, E. (2011). Volcano surveillance using infrared cameras. *Earth-Science Reviews*, *106*(1–2), 63–91. <https://doi.org/10.1016/j.earscirev.2011.01.003>
- Sparks, R. S. J. (1986). The dimensions and dynamics of volcanic eruption columns. *Bulletin of Volcanology*, *48*(1), 3–15. <https://doi.org/10.1007/BF01073509>
- Sparks, R. S. J., Biggs, J., & Neuberg, J. W. (2012). Monitoring volcanoes. *Science*, *335*(6074), 1310–1311. <https://doi.org/10.1126/science.1219485>
- Sparks, R. S. J., Bursik, M. I., Carey, S. N., Gilbert, J. S., Glaze, L., Sigurdsson, H., & Woods, A. W. (1997). *Volcanic plumes*. John Wiley & Sons, Inc.
- Sparks, R. S. J., Moore, J. G., & Rice, C. J. (1986). The initial giant umbrella cloud of the May 18th, 1980, explosive eruption of Mount St. Helens. *Journal of Volcanology and Geothermal Research*, *28*(3–4), 257–274. [https://doi.org/10.1016/0377-0273\(86\)90026-0](https://doi.org/10.1016/0377-0273(86)90026-0)
- Sparks, R. S. J., & Wilson, L. (1976). A model for the formation of ignimbrite by gravitational column collapse. *Journal of the Geological Society*, *132*(4), 441–451. <https://doi.org/10.1144/gsjgs.132.4.0441>
- Stein, A. F., Draxler, R. R., Rolph, G. D., Stunder, B. J., Cohen, M. D., & Ngan, F. (2015). NOAA's HYSPLIT atmospheric transport and dispersion modeling system. *Bulletin of the American Meteorological Society*, *96*(12), 2059–2077. <https://doi.org/10.1175/BAMS-D-14-00110.1>
- Stephens, G. L., Vane, D. G., Boain, R. J., Mace, G. G., Sassen, K., Wang, Z., et al. (2002). The CloudSat mission and the A-train: A new dimension of space-based observations of clouds and precipitation. *Bulletin of the American Meteorological Society*, *83*(12), 1771–1790. <https://doi.org/10.1175/BAMS-83-12-1771>
- Stewart, C., Damby, D. E., Horwell, C. J., Elias, T., Ilyinskaya, E., Tomašek, I., et al. (2022). Volcanic air pollution and human health: Recent advances and future directions. *Bulletin of Volcanology*, *84*(1), 11. <https://doi.org/10.1007/s00445-021-01513-9>
- Stohl, A., Prata, A. J., Eckhardt, S., Clarisse, L., Durant, A., Henne, S., et al. (2011). Determination of time- and height-resolved volcanic ash emissions and their use for quantitative ash dispersion modeling: The 2010 Eyjafjallajökull eruption. *Atmospheric Chemistry and Physics*, *11*(9), 4333–4351. <https://doi.org/10.5194/acp-11-4333-2011>
- Stokes, G. G. (1851). On the effect of the internal friction of fluids on the motion of pendulums. *Transactions of the Cambridge Philosophical Society*, *9*(Part II), 8e106.
- Stuefer, M., Freitas, S. R., Grell, G., Webley, P., Peckham, S., McKeen, S. A., & Egan, S. D. (2013). Inclusion of ash and SO<sub>2</sub> emissions from volcanic eruptions in WRF-Chem: Development and some applications. *Geoscientific Model Development*, *6*(2), 457–468. <https://doi.org/10.5194/gmd-6-457-2013>
- Suh, S. H., Maki, M., Iguchi, M., Lee, D. I., Yamaji, A., & Momotani, T. (2019). Free-fall experiments of volcanic ash particles using a 2-D video disdrometer. *Atmospheric Measurement Techniques*, *12*(10), 5363–5379. <https://doi.org/10.5194/amt-12-5363-2019>
- Sulpizio, R., Folch, A., Costa, A., Scaini, C., & Dellino, P. (2012). Hazard assessment of far-range volcanic ash dispersal from a violent strombolian eruption at Somma-Vesuvius volcano, Naples, Italy: Implications on civil aviation. *Bulletin of Volcanology*, *74*(9), 2205–2218. <https://doi.org/10.1007/s00445-012-0656-3>
- Sun, H., Eastham, S., & Keith, D. (2022). Developing a plume-in-grid model for plume evolution in the stratosphere. *Journal of Advances in Modeling Earth Systems*, *14*(4), e2021MS002816. <https://doi.org/10.1029/2021MS002816>
- Suzuki, T. (1983). A theoretical model for dispersion of tephra. In *Arc volcanism: physics and tectonics* (Vol. 95, p. 113).
- Suzuki, Y. J., Costa, A., Cerminara, M., Ongaro, T. E., Herzog, M., Van Eaton, A. R., & Denby, L. C. (2016). Inter-comparison of three-dimensional models of volcanic plumes. *Journal of Volcanology and Geothermal Research*, *326*, 26–42. <https://doi.org/10.1016/j.jvolgeores.2016.06.011>
- Suzuki, Y. J., Costa, A., & Koyaguchi, T. (2020). Control of vent geometry on the fluid dynamics of volcanic plumes: Insights from numerical simulations. *Geophysical Research Letters*, *47*(10), e2020GL087038. <https://doi.org/10.1029/2020gl087038>
- Suzuki, Y. J., & Koyaguchi, T. (2009). A three-dimensional numerical simulation of spreading umbrella clouds. *Journal of Geophysical Research*, *114*(B3), B03209. <https://doi.org/10.1029/2007JB005369>
- Suzuki, Y. J., & Koyaguchi, T. (2010). Numerical determination of the efficiency of entrainment in volcanic eruption columns. *Geophysical Research Letters*, *37*(5), L05302. <https://doi.org/10.1029/2009GL042159>
- Suzuki, Y. J., & Koyaguchi, T. (2015). Effects of wind on entrainment efficiency in volcanic plumes. *Journal of Geophysical Research: Solid Earth*, *120*(9), 6122–6140. <https://doi.org/10.1002/2015JB012208>
- Tackett, J. L., Kar, J., Vaughan, M. A., Getzewich, B. J., Kim, M. H., Vernier, J. P., et al. (2023). The CALIPSO version 4.5 stratospheric aerosol subtyping algorithm. *Atmospheric Measurement Techniques*, *16*(3), 745–768. <https://doi.org/10.5194/amt-16-745-2023>
- Taddeucci, J., Scarlato, P., Montanaro, C., Cimarelli, C., Del Bello, E., Freda, C., et al. (2011). Aggregation-dominated ash settling from the Eyjafjallajökull volcanic cloud illuminated by field and laboratory high-speed imaging. *Geology*, *39*(9), 891–894. <https://doi.org/10.1130/g32016.1>
- Takishita, K., Poulidis, A. P., & Iguchi, M. (2022). In-situ measurement of tephra deposit load based on a disdrometer network at Sakurajima volcano, Japan. *Journal of Volcanology and Geothermal Research*, *421*, 107442. <https://doi.org/10.1016/j.jvolgeores.2021.107442>
- Taylor, I. A., Grainger, R. G., Prata, A. T., Proud, S. R., Mather, T. A., & Pyle, D. M. (2023). A satellite chronology of plumes from the April 2021 eruption of La Soufrière, St Vincent. *Atmospheric Chemistry and Physics*, *23*(24), 15209–15234. <https://doi.org/10.5194/acp-23-15209-2023>
- Thomas, G. E., & Siddans, R. (2015). Development of OCA type processors to volcanic ash detection and retrieval. *Final Report EUMETSAT RFG*, *13*(715), 490.

- Titos, M., Martínez Montesinos, B., Barsotti, S., Sandri, L., Folch, A., Mingari, L., et al. (2022). Long-term hazard assessment of explosive eruptions at Jan Mayen (Norway) and implications for air traffic in the North Atlantic. *Natural Hazards and Earth System Sciences*, 22(1), 139–163. <https://doi.org/10.5194/nhess-22-139-2022>
- Torres, O., Tanskanen, A., Veihelmann, B., Ahn, C., Braak, R., Bhartia, P. K., et al. (2007). Aerosols and surface UV products from Ozone Monitoring Instrument observations: An overview. *Journal of Geophysical Research*, 112(D24), D24S47. <https://doi.org/10.1029/2007JD008809>
- Trancoso, R., Behr, Y., Hurst, T., & Deligne, N. I. (2022). Towards real-time probabilistic ash deposition forecasting for New Zealand. *Journal of Applied Volcanology*, 11(1), 13. <https://doi.org/10.1186/s13617-022-00123-0>
- Tupper, A., Textor, C., Herzog, M., Graf, H. F., & Richards, M. S. (2009). Tall clouds from small eruptions: The sensitivity of eruption height and fine ash content to tropospheric instability. *Natural Hazards*, 51(2), 375–401. <https://doi.org/10.1007/s11069-009-9433-9>
- Turcotte, D. L. (1997). *Fractals and chaos in geology and geophysics*. Cambridge University Press.
- Turnbull, K., Johnson, B., Marengo, F., Haywood, J., Minikin, A., Weinzierl, B., et al. (2012). A case study of observations of volcanic ash from the eyjafjallajökull eruption: 1. In situ airborne observations. *Journal of Geophysical Research*, 117(D20), D00U13. <https://doi.org/10.1029/2011JD016688>
- Turner, J. S. (1986). Turbulent entrainment: The development of the entrainment assumption, and its application to geophysical flows. *Journal of Fluid Mechanics*, 173, 431–471. <https://doi.org/10.1017/S0022112086001222>
- Uppala, S. M., Källberg, P. W., Simmons, A. J., Andrae, U., Bechtold, V. D. C., Fiorino, M., et al. (2005). The ERA-40 re-analysis. *Quarterly Journal of the Royal Meteorological Society: A Journal of the Atmospheric Sciences, Applied Meteorology and Physical Oceanography*, 131(612), 2961–3012. <https://doi.org/10.1256/qj.04.176>
- Valade, S. A., Harris, A. J. L., & Cerminara, M. (2014). Plume Ascent Tracker: Interactive Matlab software for analysis of ascending plumes in image data. *Computers & Geosciences*, 66, 132–144. <https://doi.org/10.1016/j.cageo.2013.12.015>
- Valentine, G. A., & Wohletz, K. H. (1989). Numerical models of Plinian eruption columns and pyroclastic flows. *Journal of Geophysical Research*, 94(B2), 1867–1887. <https://doi.org/10.1029/JB094iB02p01867>
- Van Eaton, A. R., Amigo, Á., Bertin, D., Mastin, L. G., Giacosa, R. E., González, J., et al. (2016). Volcanic lightning and plume behavior reveal evolving hazards during the April 2015 eruption of Calbuco volcano, Chile. *Geophysical Research Letters*, 43(7), 3563–3571. <https://doi.org/10.1002/2016GL068076>
- Van Eaton, A. R., Herzog, M., Wilson, C. J. N., & McGregor, J. (2012). Ascent dynamics of large phreatomagmatic eruption clouds: The role of microphysics. *Journal of Geophysical Research*, 117(B3). <https://doi.org/10.1029/2011JB008892>
- Van Eaton, A. R., Lapierre, J., Behnke, S. A., Vagasky, C., Schultz, C. J., Pavolonis, M., et al. (2023). Lightning rings and gravity waves: Insights into the giant eruption plume from Tonga's Hunga Volcano on 15 January 2022. *Geophysical Research Letters*, 50(12), e2022GL102341. <https://doi.org/10.1029/2022GL102341>
- Van Eaton, A. R., Mastin, L. G., Herzog, M., Schwaiger, H. F., Schneider, D. J., Wallace, K. L., & Clarke, A. B. (2015). Hail formation triggers rapid ash aggregation in volcanic plumes. *Nature Communications*, 6(1), 7860. <https://doi.org/10.1038/ncomms8860>
- Van Eaton, A. R., Muirhead, J. D., Wilson, C. J., & Cimarelli, C. (2012). Growth of volcanic ash aggregates in the presence of liquid water and ice: An experimental approach. *Bulletin of Volcanology*, 74(9), 1963–1984. <https://doi.org/10.1007/s00445-012-0634-9>
- Van Eaton, A. R., & Wilson, C. J. (2013). The nature, origins and distribution of ash aggregates in a large-scale wet eruption deposit: Oruanui, New Zealand. *Journal of Volcanology and Geothermal Research*, 250, 129–154. <https://doi.org/10.1016/j.jvolgeores.2012.10.016>
- Van Zadelhoff, G. J., Donovan, D. P., & Wang, P. (2023). Detection of aerosol and cloud features for the EarthCARE atmospheric lidar (ATLID): The ATLID FeatureMask (A-FM) product. *Atmospheric Measurement Techniques*, 16(15), 3631–3651. <https://doi.org/10.5194/amt-16-3631-2023>
- Vecino, M. D., Rossi, E., Freret-Lorgeril, V., Fries, A., Gabellini, P., Lemus, J., et al. (2022). Aerodynamic characteristics and Genesis of aggregates at Sakurajima volcano, Japan. *Scientific Reports*, 12(1), 2044. <https://doi.org/10.1038/s41598-022-05854-z>
- Ventress, L. J., McGarragh, G., Carboni, E., Smith, A. J., & Grainger, R. G. (2016). Retrieval of ash properties from IASI measurements. *Atmospheric Measurement Techniques*, 9(11), 5407–5422. <https://doi.org/10.5194/amt-9-5407-2016>
- Vergoz, J., Hupe, P., Listowski, C., Le Pichon, A., Garcés, M. A., Marchetti, E., et al. (2022). IMS observations of infrasound and acoustic-gravity waves produced by the January 2022 volcanic eruption of Hunga, Tonga: A global analysis. *Earth and Planetary Science Letters*, 591, 117639. <https://doi.org/10.1016/j.epsl.2022.117639>
- Vernier, J. P., Fairlie, T. D., Murray, J. J., Tupper, A., Trepte, C., Winker, D., et al. (2013). An advanced system to monitor the 3D structure of diffuse volcanic ash clouds. *Journal of Applied Meteorology and Climatology*, 52(9), 2125–2138. <https://doi.org/10.1175/JAMC-D-12-0279.1>
- Vernier, J. P., Kalnajs, L., Diaz, J. A., Reese, T., Corrales, E., Alan, A., et al. (2020). VolKilau: Volcano rapid response balloon campaign during the 2018 Kilauea eruption. *Bulletin of the American Meteorological Society*, 101(10), E1602–E1618. <https://doi.org/10.1175/BAMS-D-19-0011.1>
- Vidal, L., Nesbitt, S. W., Salio, P., Farias, C., Nicora, M. G., Osore, M. S., et al. (2017). C-band dual-polarization radar observations of a massive volcanic eruption in South America. *Ieee Journal of Selected Topics in Applied Earth Observations and Remote Sensing*, 10(3), 960–974. <https://doi.org/10.1109/JSTARS.2016.2640227>
- Vittorio, F., Guidard, V., & Fourrié, N. (2021). An infrared atmospheric sounding Interferometer-new generation (IASI-NG) channel selection for numerical weather prediction. *Quarterly Journal of the Royal Meteorological Society*, 147(739), 3297–3317. <https://doi.org/10.1002/qj.4129>
- Volentik, A. C., & Houghton, B. F. (2015). Tephra fallout hazards at quito international airport (Ecuador). *Bulletin of Volcanology*, 77(6), 1–14. <https://doi.org/10.1007/s00445-015-0923-1>
- Volz, F. E. (1973). Infrared optical constants of ammonium sulfate, Sahara dust, volcanic pumice, and flyash. *Applied Optics*, 12(3), 564–568. <https://doi.org/10.1364/AO.12.000564>
- Walker, G. P. (1981). Generation and dispersal of fine ash and dust by volcanic eruptions. *Journal of Volcanology and Geothermal Research*, 11(1), 81–92. [https://doi.org/10.1016/0377-0273\(81\)90077-9](https://doi.org/10.1016/0377-0273(81)90077-9)
- Wallace, K. L., Schaefer, J. R., & Coombs, M. L. (2013). Character, mass, distribution, and origin of tephra-fall deposits from the 2009 eruption of Redoubt Volcano, Alaska—Highlighting the significance of particle aggregation. *Journal of Volcanology and Geothermal Research*, 259, 145–169. <https://doi.org/10.1016/j.jvolgeores.2012.09.015>
- Wardman, J. B., Wilson, T. M., Bodger, P. S., Cole, J. W., & Stewart, C. (2012). Potential impacts from tephra fall to electric power systems: A review and mitigation strategies. *Bulletin of Volcanology*, 74(10), 2221–2241. <https://doi.org/10.1007/s00445-012-0664-3>
- Watkin, S. C. (2003). The application of AVHRR data for the detection of volcanic ash in a Volcanic Ash Advisory Centre. *Meteorological Applications*, 10(4), 301–311. <https://doi.org/10.1017/S1350482703001063>

- Watson, I. M., Realmuto, V. J., Rose, W. I., Prata, A. J., Bluth, G. J., Gu, Y., et al. (2004). Thermal infrared remote sensing of volcanic emissions using the moderate resolution imaging spectroradiometer. *Journal of Volcanology and Geothermal Research*, *135*(1–2), 75–89. <https://doi.org/10.1016/j.jvolgeores.2003.12.017>
- Watson, L. M. (2020). Using unsupervised machine learning to identify changes in eruptive behavior at Mount Etna, Italy. *Journal of Volcanology and Geothermal Research*, *405*, 107042. <https://doi.org/10.1016/j.jvolgeores.2020.107042>
- Weber, K., Eliasson, J., Vogel, A., Fischer, C., Pohl, T., Van Haren, G., et al. (2012). Airborne in-situ investigations of the Eyjafjallajökull volcanic ash plume on Iceland and over north-western Germany with light aircrafts and optical particle counters. *Atmospheric Environment*, *48*, 9–21. <https://doi.org/10.1016/j.atmosenv.2011.10.030>
- Webley, P. W., Stunder, B. J. B., & Dean, K. G. (2009). Preliminary sensitivity study of eruption source parameters for operational volcanic ash cloud transport and dispersion models—A case study of the August 1992 eruption of the Crater Peak vent, Mount Spurr, Alaska. *Journal of Volcanology and Geothermal Research*, *186*(1–2), 108–119. <https://doi.org/10.1016/j.jvolgeores.2009.02.012>
- Webster, H., & Thomson, D. (2017). A particle size dependent wet deposition scheme for NAME. In *Forecasting research technical report; Met Office: Exeter, UK*, 2017 (Vol. 624).
- Wehr, T., Kubota, T., Tzeremes, G., Wallace, K., Nakatsuka, H., Ohno, Y., et al. (2023). The EarthCARE mission—science and system overview. *Atmospheric Measurement Techniques*, *16*(15), 3581–3608. <https://doi.org/10.5194/amt-16-3581-2023>
- Wen, S., & Rose, W. I. (1994). Retrieval of sizes and total masses of particles in volcanic clouds using AVHRR bands 4 and 5. *Journal of Geophysical Research*, *99*(D3), 5421–5431. <https://doi.org/10.1029/93JD03340>
- Westphal, D. L., Toon, O. B., & Carlson, T. N. (1987). A two-dimensional numerical investigation of the dynamics and microphysics of Saharan dust storms. *Journal of Geophysical Research*, *92*(D3), 3027–3049. <https://doi.org/10.1029/JD092iD03p03027>
- Wilkes, T. C., Pering, T. D., & McGonigle, A. J. S. (2022). Semantic segmentation of explosive volcanic plumes through deep learning. *Computers & Geosciences*, *168*, 105216. <https://doi.org/10.1016/j.cageo.2022.105216>
- Wilkins, K. L., Mackie, S., Watson, M., Webster, H. N., Thomson, D. J., & Dacre, H. F. (2015). Data insertion in volcanic ash cloud forecasting. *Annals of Geophysics*, *57*. <https://doi.org/10.4401/ag-6624>
- Wilkins, K. L., Watson, I. M., Kristiansen, N. I., Webster, H. N., Thomson, D. J., Dacre, H. F., & Prata, A. J. (2016). Using data insertion with the NAME model to simulate the 8 May 2010 Eyjafjallajökull volcanic ash cloud. *Journal of Geophysical Research: Atmospheres*, *121*(1), 306–323. <https://doi.org/10.1002/2015JD023895>
- Wilkins, K. L., Western, L. M., & Watson, I. M. (2016). Simulating atmospheric transport of the 2011 Grímsvötn ash cloud using a data insertion update scheme. *Atmospheric Environment*, *141*, 48–59. <https://doi.org/10.1016/j.atmosenv.2016.06.045>
- Wilson, G., Wilson, T. M., Deligne, N. I., & Cole, J. W. (2014). Volcanic hazard impacts to critical infrastructure: A review. *Journal of Volcanology and Geothermal Research*, *286*, 148–182. <https://doi.org/10.1016/j.jvolgeores.2014.08.030>
- Wilson, L. (1976). Explosive volcanic eruptions III, Plinian eruption columns. *Geophysical Journal of the Royal Astronomical Society*, *45*(3), 543–556. <https://doi.org/10.1111/j.1365-246X.1958.tb05342.x>
- Wilson, L., & Huang, T. C. (1979). The influence of shape on the atmospheric settling velocity of volcanic ash particles. *Earth and Planetary Science Letters*, *44*(2), 311–324. [https://doi.org/10.1016/0012-821X\(79\)90179-1](https://doi.org/10.1016/0012-821X(79)90179-1)
- Wilson, L., Sparks, R. S. J., Huang, T. C., & Watkins, N. D. (1978). The control of volcanic column heights by eruption energetics and dynamics. *Journal of Geophysical Research*, *83*(B4), 1829–1836. <https://doi.org/10.1029/JB083iB04p01829>
- Wilson, T. M., Cole, J. W., Stewart, C., Cronin, S. J., & Johnston, D. M. (2011). Ash storms: Impacts of wind-remobilised volcanic ash on rural communities and agriculture following the 1991 Hudson eruption, southern Patagonia, Chile. *Bulletin of Volcanology*, *73*(3), 223–239. <https://doi.org/10.1007/s00445-010-0396-1>
- Wilson, T. M., Jenkins, S., & Stewart, C. (2015). Impacts from volcanic ash fall. In *Volcanic hazards, risks and disasters* (pp. 47–86). Elsevier. <https://doi.org/10.1016/B978-0-12-396453-3.00003-4>
- Wilson, T. M., Stewart, C., Sword-Daniels, V., Leonard, G. S., Johnston, D. M., Cole, J. W., et al. (2012). Volcanic ash impacts on critical infrastructure. *Physics and Chemistry of the Earth, Parts A/B/C*, *45*, 5–23. <https://doi.org/10.1016/j.pce.2011.06.006>
- Winker, D. M., Liu, Z., Omar, A., Tackett, J., & Fairlie, D. (2012). CALIOP observations of the transport of ash from the Eyjafjallajökull volcano in April 2010. *Journal of Geophysical Research*, *117*(D20), D00U15. <https://doi.org/10.1029/2011JD016499>
- Witsil, A. J., & Johnson, J. B. (2020). Analyzing continuous infrasound from Stromboli volcano, Italy using unsupervised machine learning. *Computers & Geosciences*, *140*, 104494. <https://doi.org/10.1016/j.cageo.2020.104494>
- Wolfe, E. W., & Hoblitt, R. P. (1996). Overview of the eruptions. In *Fire and Mud: Eruptions and Lahars of Mount Pinatubo, Philippines* (pp. 3–20). University of Washington Press.
- Wood, K., Thomas, H., Watson, M., Calway, A., Richardson, T., Stebel, K., et al. (2019). Measurement of three dimensional volcanic plume properties using multiple ground based infrared cameras. *ISPRS Journal of Photogrammetry and Remote Sensing*, *154*, 163–175. <https://doi.org/10.1016/j.isprsjprs.2019.06.002>
- Woodhouse, M. J., Hogg, A. J., Phillips, J. C., & Sparks, R. S. J. (2013). Interaction between volcanic plumes and wind during the 2010 Eyjafjallajökull eruption, Iceland. *Journal of Geophysical Research: Solid Earth*, *118*(1), 92–109. <https://doi.org/10.1029/2012JB009592>
- Woods, A. W. (1988). The fluid dynamics and thermodynamics of eruption columns. *Bulletin of Volcanology*, *50*(3), 169–193. <https://doi.org/10.1007/BF01079681>
- Woods, A. W. (1993). Moist convection and the injection of volcanic ash into the atmosphere. *Journal of Geophysical Research*, *98*(B10), 17627–17636. <https://doi.org/10.1029/93JB00718>
- Woods, A. W., & Bower, S. M. (1995). The decompression of volcanic jets in a crater during explosive volcanic eruptions. *Earth and Planetary Science Letters*, *131*(3–4), 189–205. [https://doi.org/10.1016/0012-821X\(95\)00012-2](https://doi.org/10.1016/0012-821X(95)00012-2)
- Woods, A. W., & Self, S. (1992). Thermal disequilibrium at the top of volcanic clouds and its effect on estimates of the column height. *Nature*, *355*(6361), 628–630. <https://doi.org/10.1038/355628a0>
- Wright, C. J., Hindley, N. P., Alexander, M. J., Barlow, M., Hoffmann, L., Mitchell, C. N., et al. (2022). Surface-to-space atmospheric waves from Hunga Tonga–Hunga Ha’apai eruption. *Nature*, *609*(7928), 741–746. <https://doi.org/10.1038/s41586-022-050>
- Wynanski, I., & Fiedler, H. (1969). Some measurements in the self-preserving jet. *Journal of Fluid Mechanics*, *38*(3), 577–612. <https://doi.org/10.1017/S0022112069000358>
- Yamamoto, H., Watson, I. M., Phillips, J. C., & Bluth, G. J. (2008). Rise dynamics and relative ash distribution in vulcanian eruption plumes at Santiaguito Volcano, Guatemala, revealed using an ultraviolet imaging camera. *Geophysical Research Letters*, *35*(8), L08314. <https://doi.org/10.1029/2007GL032008>
- Yu, T., Rose, W. I., & Prata, A. J. (2002). Atmospheric correction for satellite-based volcanic ash mapping and retrievals using “split window” IR data from GOES and AVHRR. *Journal of Geophysical Research*, *107*(D16), AAC10. <https://doi.org/10.1029/2001JD000706>

- Zidikheri, M. J., & Lucas, C. (2021a). A computationally efficient ensemble filtering scheme for quantitative volcanic ash forecasts. *Journal of Geophysical Research: Atmospheres*, *126*(2), e2020JD033094. <https://doi.org/10.1029/2020JD033094>
- Zidikheri, M. J., & Lucas, C. (2021b). Improving ensemble volcanic ash forecasts by direct insertion of satellite data and ensemble filtering. *Atmosphere*, *12*(9), 1215. <https://doi.org/10.3390/atmos12091215>
- Zidikheri, M. J., Lucas, C., & Potts, R. J. (2017). Toward quantitative forecasts of volcanic ash dispersal: Using satellite retrievals for optimal estimation of source terms. *Journal of Geophysical Research: Atmospheres*, *122*(15), 8187–8206. <https://doi.org/10.1002/2017JD026679>
- Zidikheri, M. J., Lucas, C., & Potts, R. J. (2018). Quantitative verification and calibration of volcanic ash ensemble forecasts using satellite data. *Journal of Geophysical Research: Atmospheres*, *123*(8), 4135–4156. <https://doi.org/10.1002/2017JD027740>
- Zidikheri, M. J., Potts, R., & Lucas, C. (2014). A probabilistic inverse method for volcanic ash dispersion modelling. *ANZIAM Journal*, *56*, C194–C209. <https://doi.org/10.21914/anziamj.v56i0.9384>
- Zimanowski, B. (1998). Phreatomagmatic explosions. In A. Freundt, & M. Rosi (Eds.) *From Magma to Tephra: Modeling physical processes of explosive volcanic eruptions* (pp. 25–53). Elsevier.